

INFORMATION TO USERS

This manuscript has been reproduced from the microfilm master. UMI films the text directly from the original or copy submitted. Thus, some thesis and dissertation copies are in typewriter face, while others may be from any type of computer printer.

The quality of this reproduction is dependent upon the quality of the copy submitted. Broken or indistinct print, colored or poor quality illustrations and photographs, print bleedthrough, substandard margins, and improper alignment can adversely affect reproduction.

In the unlikely event that the author did not send UMI a complete manuscript and there are missing pages, these will be noted. Also, if unauthorized copyright material had to be removed, a note will indicate the deletion.

Oversize materials (e.g., maps, drawings, charts) are reproduced by sectioning the original, beginning at the upper left-hand corner and continuing from left to right in equal sections with small overlaps.

ProQuest Information and Learning
300 North Zeeb Road, Ann Arbor, MI 48106-1346 USA
800-521-0600

UMI[®]

The Pennsylvania State University
The Graduate School
Department of Materials Science and Engineering

**TEXTURING OF $\text{Na}_{1/2}\text{Bi}_{1/2}\text{TiO}_3\text{-BaTiO}_3$
CERAMICS BY TEMPLATED GRAIN GROWTH**

A Thesis in
Materials Science and Engineering
by

Huseyin Yilmaz

© 2002 Huseyin Yilmaz

Submitted in Partial Fulfillment
of the Requirements
for the Degree of

Doctor of Philosophy

December 2002

UMI Number: 3077026

UMI[®]

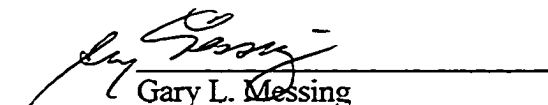
UMI Microform 3077026

Copyright 2003 by ProQuest Information and Learning Company.
All rights reserved. This microform edition is protected against
unauthorized copying under Title 17, United States Code.

ProQuest Information and Learning Company
300 North Zeeb Road
P.O. Box 1346
Ann Arbor, MI 48106-1346

We approve the thesis of Huseyin Yilmaz.

Date of Signature



Gary L. Messing
Professor of Ceramic Science and Engineering
Thesis Co-Advisor
Co-Chair of Committee

Aug 27, 2002



Susan Trolier-McKinstry
Professor of Ceramic Science and Engineering
Thesis Co-Advisor
Co-Chair of Committee

Sept. 18, 2002



Thomas R. Shroud
Professor of Materials
Senior Scientist

Sept 19, 2002



Clive A. Randall
Professor of Materials Science and Engineering

Sept 19, 2002



James P. Runt
Professor of Polymer Science
Associate Head for Graduate Studies

9/19/02

ABSTRACT

Sodium bismuth titanate modified with barium titanate, $(\text{Na}_{1/2}\text{Bi}_{1/2})\text{TiO}_3\text{-BaTiO}_3$ (NBT-BT), is a candidate lead-free piezoelectric material which has been shown to have comparatively high piezoelectric response. In this work, textured $(\text{Na}_{1/2}\text{Bi}_{1/2})\text{TiO}_3\text{-BaTiO}_3$ (5.5mol% BaTiO_3) ceramics with $\langle 100 \rangle_{\text{pc}}$ (where pc denotes the pseudocubic perovskite cell) orientation were fabricated by Templated Grain Growth (TGG) or Reactive Templated Grain Growth (RTGG) using anisotropically shaped template particles. In the case of TGG, molten salt synthesized SrTiO_3 platelets were tape cast with a $(\text{Na}_{1/2}\text{Bi}_{1/2})\text{TiO}_3\text{-5.5mol\%BaTiO}_3$ powder and sintered at 1200°C for up to 12 hours. For the RTGG approach, $\text{Bi}_4\text{Ti}_3\text{O}_{12}$ (BiT) platelets were tape cast with a Na_2CO_3 , Bi_2O_3 , TiO_2 , and BaCO_3 powder mixture and reactively sintered. The TGG approach using SrTiO_3 templates gave stronger texture along [001] compared to the RTGG approach using BiT templates. The textured ceramics were characterized by X-ray and electron backscatter diffraction for the quality of texture. The texture function was quantified by the Lotgering factor, rocking curve, pole figures, inverse pole figures, and orientation imaging microscopy. The grain orientation distribution in the [001], as measured by x-ray rocking curve (and also OIM), has a full width at half maximum of $\sim 8^\circ$ and a texture fraction of 80% for the samples sintered at 1200°C for 12 hours in O_2 .

Electrical and electromechanical property characterization of randomly oriented and $\langle 001 \rangle_{\text{pc}}$ textured $(\text{Na}_{1/2}\text{Bi}_{1/2})\text{TiO}_3\text{-5.5 mol\% BaTiO}_3$ rhombohedral ceramics showed 0.26% strain at 70 kV/cm, and large field d_{33} coefficients over 500 pC/N have been obtained for highly textured samples ($f \sim 90\%$). The d_{33} coefficient from Berlincourt

measurements was $d_{33} \sim 200$ pC/N. The materials show considerable hysteresis. The presence of hysteresis in the unipolar-electric field curve may be linked to the ferroelastic phase transition seen in the $(\text{Na}_{1/2}\text{Bi}_{1/2})\text{TiO}_3$ system on cooling from high temperature at $\sim 520^\circ\text{C}$.

The macroscopic physical properties (remanent polarization, dielectric constant, and piezoelectric coefficient) of random and textured ($[001]_{pc}$) rhombohedral perovskites were estimated by linear averaging of single crystal data. However, the complete polarization, dielectric, and piezoelectric tensors are not available for NBT-BT single crystals. Therefore, the properties of lead based (PZT, 52/48) rhombohedral ferroelectric single domain-single crystals, whose properties (polarization, dielectric and piezoelectric) were computed using Landau-Ginsburg-Devonshire phenomenological theory (by Haun et al.), were used in the calculations for random and textured cases. Based on the averaging calculations for a ceramic with rhombohedral symmetry, the remanent polarization was expected to decrease but the other properties like dielectric constant and piezoelectric coefficient were expected to increase as the texture fraction in the ceramic increases. The experimental findings were in agreement with the trends in the calculations.

TABLE OF CONTENTS

LIST OF FIGURES	viii
LIST OF TABLES	xiv
LIST OF SYMBOLS	xv
ACKNOWLEDGEMENTS	xvii
CHAPTER 1. STATEMENT OF THE PROBLEM	1
1.1 STATEMENT OF THE PROBLEM	1
1.2 SCIENTIFIC APPROACH	3
1.3 ORGANIZATION OF THE THESIS	4
1.4 REFERENCES	6
CHAPTER 2. LITERATURE REVIEW	8
2.1 INTRODUCTION	8
2.2 SODIUM BISMUTH TITANATE AND ITS SOLID SOLUTIONS	10
2.3 ELECTRICAL AND ELECTROMECHANICAL PROPERTIES OF TEXTURED PIEZOELECTRIC CERAMICS	23
2.4 MODELING OF STRUCTURE PROPERTY RELATIONS OF RANDOM AND ORIENTED CERAMICS	26
2.5 TEMPLATED GRAIN GROWTH AND TEMPLATE CHARACTERISTICS	34
2.6 REFERENCES	38
CHAPTER 3. (REACTIVE) TEMPLATED GRAIN GROWTH OF TEXTURED SODIUM BISMUTH TITANATE ($\text{Na}_{1/2}\text{Bi}_{1/2}\text{TiO}_3$- BaTiO_3) CERAMICS	45
3.1 INTRODUCTION	45
3.2 EXPERIMENTAL PROCEDURE	47
3.2.1 TEMPLATE SYNTHESIS	47
3.2.2 SAMPLE PREPARATION	49
3.3 RESULTS AND DISCUSSION	53
3.3.1 TGG OF NBT USING SrTiO_3 TEMPLATE PARTICLES	53
3.3.2 SINTERING AND MICROSTRUCTURE	55
3.3.3 REACTIVE TEMPLATED GRAIN GROWTH USING $\text{Bi}_4\text{Ti}_3\text{O}_{12}$ TEMPLATE PARTICLES	63
3.4 CONCLUSIONS	70

3.5 REFERENCES	72
CHAPTER 4. (REACTIVE) TEMPLATED GRAIN GROWTH OF TEXTURED SODIUM BISMUTH TITANATE ($\text{Na}_{1/2}\text{Bi}_{1/2}\text{TiO}_3$- BaTiO_3) CERAMICS	75
4.1 INTRODUCTION	75
4.2 EXPERIMENTAL PROCEDURE	77
4.3 RESULTS AND DISCUSSION	78
4.3.1 X-RAY DIFFRACTION ANALYSIS	78
4.3.2 HIGH FIELD ELECTRICAL PROPERTIES OF TEXTURED NBT-BT CERAMICS	83
4.3.2.1 POLARIZATION	83
4.3.2.2 ELECTROMECHANICAL PROPERTIES	89
4.3.2.3 HYSTERESIS IN NBT CERAMICS	97
4.3.2.4 DIELECTRIC PROPERTIES	109
4.4 ELECTRICAL PROPERTIES OF $\text{Bi}_4\text{Ti}_3\text{O}_{12}$ TEMPLATED $\text{Na}_{1/2}\text{Bi}_{1/2}\text{TiO}_3$ - BaTiO_3 CERAMICS	113
4.4 CONCLUSIONS	117
4.5 REFERENCES	118
CHAPTER 5. ELECTRON BACKSCATTER DIFFRACTION (EBSD) CHARACTERIZATION OF NBT-BT CERAMICS	120
5.1 INTRODUCTION	120
5.2 ORIENTATION IMAGING MICROSCOPY	121
5.3 EXPERIMENTAL PROCEDURE	127
5.4 RESULTS AND DISCUSSION	128
5.4.1 RANDOM CERAMICS	128
5.4.2 TEXTURED CERAMICS	132
5.5 CONCLUSIONS	146
5.6 REFERENCES	149
CHAPTER 6. CALCULATION OF ELECTRICAL AND ELECTROMECHANICAL PROPERTIES OF TEXTURED $3m$ SYMMETRY (RHOMBOHEDRAL) CERAMICS	152
6.1 INTRODUCTION	152
6.2 AVERAGING OF POLARIZATION	154
6.3 AVERAGING OF DIELECTRIC CONSTANT	164
6.4 AVERAGING OF PIEZOELECTRIC COEFFICIENT	170
6.5 CONCLUSIONS	175
6.6 REFERENCES	178

CHAPTER 7. SUMMARY AND FUTURE WORK	180
7.1 SUMMARY	180
7.2 FUTURE WORK	183
7.3 REFERENCES	186

LIST OF FIGURES

Figure		Page
2.1	Schematic of engineered domain configuration for <001> poled rhombohedral crystals.	9
2.2	Schematic of prototype perovskite structure ($m\bar{3}m$ symmetry).	11
2.3	(a) Temperature dependence of dielectric constant and $\tan\delta$ for $\text{Na}_{1/2}\text{Bi}_{1/2}\text{TiO}_3$ ceramics at dc biases of 0 and 2 kV/mm. (b) Temperature dependence of remanent polarization for $\text{Na}_{1/2}\text{Bi}_{1/2}\text{TiO}_3$ ceramics determined from pyroelectric measurement.	13
2.4	Regions of co-existing $\text{Na}_{1/2}\text{Bi}_{1/2}\text{TiO}_3$ phases as a function of temperature.	15
2.5	Modified phase diagram of $\text{Na}_{1/2}\text{Bi}_{1/2}\text{TiO}_3$ - BaTiO_3 system (F=Ferroelectric).	18
2.6	Unipolar strain curve for 5.5 mol% BaTiO_3 doped $\text{Na}_{1/2}\text{Bi}_{1/2}\text{TiO}_3$ single crystal actuated along <001> _{pc} .	19
2.7	Strain behavior of 2% PbTiO_3 doped $\text{Na}_{1/2}\text{Bi}_{1/2}\text{TiO}_3$ single crystal.	21
2.8	Curie groups showing subgroup-supergroup relations.	24
2.9	The drawing of the model system used in EMT. Spherical ferroelectric crystal in a homogeneous piezoelectric matrix. The Euler angles ϕ , ψ , and θ relate the crystal coordinate system (x_1, x_2, x_3) to the sample coordinate system (x_1', x_2', x_3'). c =elastic stiffness, e =piezoelectric constant, ϵ = permittivity, E =constant electric field, S = constant strain, $*$ =macroscopic property.	31
2.10	Relative dielectric constant of BaTiO_3 bulk ceramics vs. normalized polarization, calculated theoretically. $\epsilon_{33}^{\text{film}}$ represents the effect of clamping by the substrate on the dielectric constant of the thin film. The dielectric constant of unpoled c- and a-textured BaTiO_3 thin films are shown as dots.	32
2.11	Piezoelectric charge coefficient vs. remanent polarization in bulk BaTiO_3 ceramics. d_{33}^{film} represents the macroscopic piezoelectric response of a BaTiO_3 film.	33

2.12	Schematic of template alignment in tape casting and sample preparation.	35
2.13	Schematic of templated grain growth at high temperatures from initial (green) stage to final stage.	36
3.1	Modified phase diagram of $\text{Na}_{1/2}\text{Bi}_{1/2}\text{TiO}_3$ - BaTiO_3 system (F=Ferroelectric).	46
3.2	SEM image of molten salt synthesized SrTiO_3 particles.	48
3.3	SEM image of molten salt synthesized $\text{Bi}_4\text{Ti}_3\text{O}_{12}$ platelets.	50
3.4	Growth of $(\text{Na}_{1/2}\text{Bi}_{1/2})_{0.945}\text{Ba}_{0.055}\text{TiO}_3$ crystal on single crystal SrTiO_3 at 1200°C .	54
3.5	SEM microstructure of NBT-5.5 %BT ceramic sintered at 1200°C for 12 hrs. Dark regions are SrTiO_3 templates whereas the light regions are the matrix material.	56
3.6	Texture evolution as function of sintering time at 1200°C , 5 vol% SrTiO_3 templated NBT-5.5 mol% BT samples.	58
3.7	SEM image of intermediate stage of sintering of SrTiO_3 templated NBT-5.5 mol% BT ceramics. Arrows mark impingement.	60
3.8	XRD pattern of textured $(\text{Na}_{1/2}\text{Bi}_{1/2})_{0.945}\text{Ba}_{0.055}\text{TiO}_3$ ceramic using 5 vol% SrTiO_3 templates sintered at 1200°C for 12 hours (top), and powder of same chemical composition (bottom).	61
3.9	Rocking curve of textured $(\text{Na}_{1/2}\text{Bi}_{1/2})_{0.945}\text{Ba}_{0.055}\text{TiO}_3$ ceramic using 5 vol% SrTiO_3 template sintered at 1200°C for 12 hours (MD Eqn.=March-Dollase equation).	62
3.10	(a) XRD-pole figure of (002) planes of textured $(\text{Na}_{1/2}\text{Bi}_{1/2})_{0.945}\text{Ba}_{0.055}\text{TiO}_3$ ceramic using 5 vol% SrTiO_3 templates sintered at 1200°C for 12 hours. (Tilt angle= 70° , Azimuthal angle= 360°). (b) XRD-pole figure of (111) planes of textured $(\text{Na}_{1/2}\text{Bi}_{1/2})_{0.945}\text{Ba}_{0.055}\text{TiO}_3$ ceramic using 5 vol% SrTiO_3 templates sintered at 1200°C for 12 hours. (Tilt angle= 70° , Azimuthal angle= 360°)	64
3.11	XRD patterns of NBT-5.5%BT ceramics textured using $\text{Bi}_4\text{Ti}_3\text{O}_{12}$ templates at different heat treatment conditions.	67

3.12	SEM image of NBT-5.5%BT ceramics textured using $\text{Bi}_4\text{Ti}_3\text{O}_{12}$ templates after 12 hours at 1200°C, side view.	68
4.1	(a) (111) x-ray pattern of SrTiO_3 templates, (b) randomly oriented NBT-5.5 mol% BT, (c) textured NBT-5.5 mol% BT, and (d) textured NBT-6.5 mol% BT ceramics (textured ceramics contain 5 vol% SrTiO_3 templates), sintered at 1200°C for 12 hrs.	80
4.2	(a) (200) x-ray pattern of SrTiO_3 templates, (b) randomly oriented NBT-5.5 mol% BT, (c) textured NBT-5.5 mol% BT, and (d) textured NBT-6.5 mol% BT ceramics (textured ceramics contain 5 vol% SrTiO_3 templates), sintered at 1200°C for 12 hrs.	81
4.3	(200) x-ray pattern of textured NBT- 5.5 mol% BaTiO_3 ceramics sintered at 1200°C for 12 hrs (a) @ RT, (b) @ 150°C, (c) @ 550°C, (textured ceramics contain 5 vol% SrTiO_3 templates).	82
4.4	Polarization vs. electric field curves of randomly oriented and textured (5 vol % SrTiO_3) NBT-BT ceramics. All samples were sintered at 1200°C for 12 hrs.	84
4.5	Polarizations and coercive fields of randomly oriented and textured (5 vol % SrTiO_3) NBT ceramics plotted as a function of % BT doping. All samples were sintered at 1200°C for 12 hrs.	85
4.6	Polarization of textured (5 vol % SrTiO_3) NBT-5.5 mol% BT ceramics plotted as function of Lotgering factor. The random ceramics had no SrTiO_3 .	88
4.7	Unipolar maximum strain of randomly oriented ceramics plotted as function of % BT doping, sintered at 1200°C for 12 hrs.	90
4.8	Unipolar maximum strain of textured NBT-5.5% BT ceramics textured with 5 vol% SrTiO_3 .	91
4.9	Unipolar maximum strain and maximum hysteresis of textured NBT-BT ceramics textured with 5 vol% SrTiO_3 plotted as function of % BT doping.	92
4.10	d_{33} coefficient of random ceramics plotted as function of % BT doping.	94
4.11	d_{33} coefficients of textured ceramics plotted as function of % BT doping, sintered at 1200°C for 12 h with 5 vol% SrTiO_3 templates. Numbers specify amount of texture (Lotgering factor).	95

4.12	Unipolar maximum strain and maximum hysteresis of textured NBT-5.5 mol% BT ceramics textured with 5 vol% SrTiO ₃ plotted as function of Lotgering factor.	96
4.13	d ₃₃ coefficient of textured NBT-5.5 mol% BT ceramics textured with 5 vol% SrTiO ₃ plotted as function of Lotgering factor, sintered at 1200°C for 12 h.	98
4.14	Schematic showing the areas used in the calculation of large signal dielectric loss factor.	100
4.15	Comparison of large signal dielectric loss factor and normalized hysteresis measurements for randomly oriented and textured NBT ceramics at different BT doping levels. @70 kV/cm	101
4.16	Normalized hysteresis measured for randomly oriented and textured NBT-0 % BT and NBT-5.5 % BT ceramics. 1) 0 mol% BT doped NBT textured ceramics, 2) 0 mol % BT doped NBT randomly oriented ceramics, 3) 5.5 mol% BT doped NBT textured ceramics, 4) 5.5 mol % BT doped NBT randomly oriented ceramics.	102
4.17	Large signal dielectric loss factor measured for randomly oriented and textured NBT-0 % BT and NBT-5.5 % BT ceramics. 1) 0 mol% BT doped NBT textured ceramics, 2) 0 mol % BT doped NBT randomly oriented ceramics, 3) 5.5 mol% BT doped NBT textured ceramics, 4) 5.5 mol % BT doped NBT randomly oriented ceramics.	103
4.18	Dielectric constant (@ 1, 10, 100, and 1000 kHz) vs. temperature behavior of randomly oriented (a) and textured (b) NBT-5.5 mol% BT ceramics, sintered at 1200°C for 12 hrs. and measured on heating. Dielectric loss is reported @ 1, 10 and 100 kHz.	111
4.19	The variation of room temperature dielectric constant of NBT-5.5 mol% BT ceramics (5 vol% SrTiO ₃ templates) as function of texture fraction, sintered at 1200°C for 12 h.	112
4.20	Dielectric constant of NBT-5.5 mo% BT ceramics: a) randomly oriented ceramics, b) textured using 6 vol% BiT template particles.	114
4.21	Unipolar strain curves of three of NBT-5.5 mo% BT ceramics at different pre-reaction conditions.	116
5.1	Kikuchi pattern of Na _{1/2} Bi _{1/2} TiO ₃ -5.5 mol % BaTiO ₃ grain captured by the CCD camera (Top). Indexed pattern (Bottom). (pc=pattern center).	122

5.2	The components of the orientation imaging system; Electron Source (typically a SEM), Phosphor Screen, Mechanical Interface, Camera System, Lens/Fiber Optic Bundle, Digital Signal Processor, Computer/Video Card, Microscope System Control Electronics.	123
5.3	The position of the sample in the SEM chamber and image formation on the phosphorus screen.	124
5.4	OIM map of $\text{Na}_{1/2}\text{Bi}_{1/2}\text{TiO}_3\text{-BaTiO}_3$ random ceramics based on crystallographic orientation. Sintered at 1200°C for 12 hrs.	129
5.5	[001] pole figure of $\text{Na}_{1/2}\text{Bi}_{1/2}\text{TiO}_3\text{-BaTiO}_3$ random ceramic.	130
5.6	Inverse pole figure of $\text{Na}_{1/2}\text{Bi}_{1/2}\text{TiO}_3\text{-BaTiO}_3$ random ceramic.	131
5.7	Edge view SEM image of textured $\text{Na}_{1/2}\text{Bi}_{1/2}\text{TiO}_3\text{-BaTiO}_3$. Rectangular grains are oriented in the [001] direction. Dark gray areas are SrTiO_3 template particles. Light gray areas are hetero-epitaxially grown $\text{Na}_{1/2}\text{Bi}_{1/2}\text{TiO}_3\text{-BaTiO}_3$ matrix phase. Those regions are marked by arrows.	133
5.8	Color-coded crystal orientation map of textured $\text{Na}_{1/2}\text{Bi}_{1/2}\text{TiO}_3\text{-BaTiO}_3$. Texture direction ([001]) is perpendicular to the plane.	134
5.9	Image quality map obtained using OIM shows the morphology of the grains. Light gray areas at the center of large grains are the template particles.	136
5.10	Schematic representing one SrTiO_3 templated $\text{Na}_{1/2}\text{Bi}_{1/2}\text{TiO}_3\text{-BaTiO}_3$ grain and its orientation in the SEM image.	137
5.11	Image quality map of SrTiO_3 single crystal templated $\text{Na}_{1/2}\text{Bi}_{1/2}\text{TiO}_3\text{-5.5 mol % BaTiO}_3$ samples.	138
5.12	Color coded orientation map of SrTiO_3 single crystal templated $\text{Na}_{1/2}\text{Bi}_{1/2}\text{TiO}_3\text{-5.5 mol % BaTiO}_3$ samples.	139
5.13	OIM derived [001], [011] and [111] pole figures. The clustering of poles at the center of [001] pole figure confirms texture in that direction.	140
5.14	Orientation distribution function of textured $\text{Na}_{1/2}\text{Bi}_{1/2}\text{TiO}_3\text{-5.5 mol % BaTiO}_3$ samples.	142
5.15	Schematic representation of Euler angles.	143

5.16	Measured pole density data from OIM and March-Dollase function for textured $\text{Na}_{1/2}\text{Bi}_{1/2}\text{TiO}_3$ -5.5 mol % BaTiO_3 samples.	147
6.1	The relationship between the trigonal unit cell and the rhombohedral (pseudocubic) unit cell illustrated.	155
6.2	The relationship between the two coordinate system in terms of the (pseudo) cubic unit cell.	156
6.3	Definition of the angles to express directions in orthogonal coordinate system with axes labeled as x_1 , x_2 , and x_3 .	159
6.4	Directional dependence of polarization function (P_3) in spherical coordinate system.	161
6.5	Calculated remanent polarization (also expressed in % of P_s) as a function of texture fraction in rhombohedral PZT (52/48).	165
6.6	Directional dependence of dielectric function (ϵ_{33}) in spherical coordinate system.	167
6.7	Calculated room temperature dielectric constant (also expressed in % of ϵ_{33}) as a function of texture fraction in rhombohedral PZT (52/48).	171
6.8	Directional dependence of piezoelectric coefficient function (d_{33}) in spherical coordinate system.	173
6.9	Calculated piezoelectric coefficient (d_{33}) (also expressed in %) as a function of texture fraction in rhombohedral PZT (52/48).	176

LIST OF TABLES

Table		Page
5.1	Comparison of different texture quantification methods of textured $\text{Na}_{1/2}\text{Bi}_{1/2}\text{TiO}_3$ -5.5 mol % BaTiO_3 samples.	145
6.1	Axes relations in the old and new coordinate system. All directions given in cubic axes.	158

LIST OF SYMBOLS

a_{ij}	Directional cosines matrix
BT	BaTiO ₃
BiT	Bi ₄ Ti ₃ O ₁₂
c	Centi
C	Coulomb
°C	Degrees Celcius
d_{ij}	Piezoelectric coefficient
e_{max}	Maximum strain energy density
E	Electric field
E	Elastic modulus
f	Texture fraction
F	Ferroelectric
F(r,f,θ)	March-Dollase function
FWHM	Full width at half maximum
Hz	Hertz
IQ	Image quality
m	Mirror
MPB	Morphotropic phase boundary
N	Newton
NBT	Na _{1/2} Bi _{1/2} TiO ₃
p	pico
Pa	Pascal
pc	pseudocubic
P_i	Polarization
P_r	Remanent polarization
P_s	Spontaneous polarization
PMN	PbMg _{1/3} Nb _{2/3} O ₃
PT	PbTiO ₃
PZT	PbZr _x Ti _{1-x} O ₃
r	Texture parameter
ST	SrTiO ₃
s_{max}	Maximum field induced strain
T	Temperature
tanδ	Loss tangent
V	Volt
°	Degree
ϵ_{ij}	Dielectric constant
μ	Micron
α_{ij}	alfa matrix
%	Percent

$\langle \rangle$ Average
 ρ Density

ACKNOWLEDGEMENTS

I am thankful to Dr. G. L. Messing and Dr. S. Trolier-McKinstry for their guidance, encouragement, and patience throughout my education at PennState. They taught me how to solve the critical problems and do an excellent job. They have strongly encouraged me to develop my research skills.

I would like to thank my committee members, Dr. T. R. ShROUT, and Dr. C. A. Randall, for their time, interest, and thoughtful questions and suggestions.

I would like to thank The Ministry of Education of The Republic of Turkey for supporting me throughout my Ph.D. study.

I would like to thank DARPA for supporting my project (Grant F49620-00-1-0098) and to Dr. Vaudin for help with the x-ray rocking curve analysis of texture.

I would like to thank to Messing Group: Dr. Lee, Kristen, and Aravind for being good friends. Similarly, to previous members, in particular to Dr. Seongtae, Dr. Duran and Dr. Sabolsky for their critical comments. Without them life at State College would be boring. I am also grateful to the MRL staff (Leah, Tim, Paul, Beth, Tim, Scott, Maria, Jeff, and many others) for their generous help when I was in need.

My dad, Mehmet, and mom, Miyase, were my biggest supporters throughout my life. I pray that Allah (cc) blesses them and gives them a long healthy life. I would also like to thank my sisters, Ayse Yilmaz and Minnaz Bostanci, and my brother, Fatih Yilmaz, for supporting their little brother (that's me, by the way) in any means.

Chapter 1

STATEMENT OF THE PROBLEM

1.1 STATEMENT OF THE PROBLEM

Piezoelectric ceramics and single crystals are used in a variety of industrial applications as: 1) generators that convert mechanical energy into electrical energy, 2) ultrasonic transducers that convert electrical energy into mechanical energy, 3) sensors that convert mechanical force into an electrical signal, and 4) actuators that convert an electrical signal into mechanical displacement (strain) [1]. The suitability of a piezoelectric material for a specific application is affected by property coefficients like d_{ij} (piezoelectric coefficient), k_{ij} (electromechanical coupling factor), and Q_m (quality factor) [2].

The most commonly used piezoelectric ceramics are usually lead-based, such as $\text{PbZr}_x\text{Ti}_{1-x}\text{O}_3$ (PZT), $\text{PbMg}_{1/3}\text{Nb}_{2/3}\text{O}_3\text{-PbTiO}_3$ (PMN-PT), and $\text{PbZn}_{1/3}\text{Nb}_{2/3}\text{O}_3\text{-PbTiO}_3$ (PZN-PT). These lead-based ceramics display high property coefficients, especially near the MPB (morphotropic phase boundary). A piezoelectric coefficient of $d_{33}\sim 600$ pC/N and electromechanical coupling coefficient of $k_{33}\sim 70\%$ have been reported for PZT-5H ceramics [3-4]. For rhombohedrally distorted lead-based relaxor ferroelectric- PbTiO_3 single crystals oriented in the $\langle 001 \rangle_{pc}$ direction, a d_{33} coefficient of 1500-2500 pC/N and electromechanical coupling coefficient of $k_{33}>90\%$ have been reported [5].

Even though single crystals display high electrical and electromechanical performance, growth of single crystals is difficult and expensive. There are also limitations on the quantity and size of the single crystals. The physical properties of

single crystals are anisotropic in nature, i.e. direction dependent. Because of the averaging of the physical properties in orientation space, the macroscopic properties of the ceramic are less than optimized orientations of single crystals.

However, it is possible to improve the macroscopic physical properties of ceramics if the grain orientations and their distributions are controlled [6-10]. Grain oriented ceramics can exhibit anisotropic physical and electrical properties like those of single crystals.

In order to obtain the maximum possible piezoelectric strain out of the crystal, optimum crystallographic cuts have to be utilized. For PZN-4.5% PT single crystals, it was shown that $\langle 001 \rangle_{pc}$ (where pc stands for pseudo cubic) oriented rhombohedral crystals have a more stable domain state and have the highest strain [5]. Therefore, $\langle 001 \rangle_{pc}$ is the optimum orientation for rhombohedral crystals. For simplicity, cubic phase Miller indices are used to indicate crystal directions throughout the thesis.

Sodium bismuth titanate (NBT) is a non-lead based ferroelectric material with a rhombohedral crystal structure. Solid solutions of NBT with BaTiO_3 remain rhombohedral up to 6.5% BT [11]. NBT is a candidate piezoelectric material suitable for applications where there is a demand for high actuation power. It has been claimed to have 1.4 times the actuation energy density of polycrystalline PMN [12]. In the [001] direction, a d_{33} coefficient as high as 450 pC/N [11] has been reported for flux grown single crystals at the morphotropic phase boundary with BaTiO_3 [12], although the crystals were also quite hysteretic (20%), where the hysteresis was defined as the maximum opening in the unipolar strain curve divided by the maximum strain reached.

In addition, NBT is a non-lead based ceramic. If high electromechanical properties in an environmentally friendly textured ferroelectric ceramic are demonstrated, it could become a first choice in some commercial applications. The primary objective of this research was to develop a process to fiber texture rhombohedral sodium bismuth titanate-barium titanate (NBT-BT) ceramics in the $\langle 001 \rangle_{pc}$ direction to improve the electromechanical properties closer to the single crystal values. Compositions close to the MPB, where properties are reported to be high, were specifically chosen for this study. A standard ceramic processing technique in which templates can be aligned with a shear force during forming would have the advantages of low cost, high yield and shape flexibility. It is also interesting to consider the origin of the large hysteresis often observed under unipolar drive in NBT family materials, and whether it is intrinsic to the system.

1.2 SCIENTIFIC APPROACH

There are many processing techniques that can be employed to prepare a grain oriented ceramic. A shear force is the common requirement in these forming techniques. In the Templated Grain Growth (TGG) process, anisotropically shaped template particles are aligned in a matrix powder system and sintered to almost full density [6-9]. Tape casting is used in this case because the shear force in the doctor blade gap aligns templates easily in the tape casting slurry and has the flexibility of producing large parts. The green body is taken to elevated temperature where grain growth is possible. Since template particles are large in size compared to the size of the matrix powder, the fine grain matrix dissolves and precipitates on the template particles epitaxially. The volume

fraction of textured material, initially equal to the volume of template particles, increases within the ceramic at the sintering temperature with grain growth.

In TGG, the choice of template particles is a key issue [8-9]. Crystallography, chemical stability (compatibility), and the orientation of the template particle has to be taken into account. The right processing conditions for full texture development have to be determined. In this study NBT-BT ceramics were textured in the $\langle 001 \rangle_{pc}$ direction using either SrTiO_3 or $\text{Bi}_4\text{Ti}_3\text{O}_{12}$ template particles using either a templated grain growth or reactive templated grain growth approach, respectively.

The electrical and electromechanical properties of the resulting fiber textured material will be addressed by averaging the single crystal properties of a system with similar crystallography, since the full dielectric and piezoelectric tensor coefficients for the rhombohedral NBT-BT are not available.

1.3 ORGANIZATION OF THE THESIS

Chapter 2 introduces a concise review of piezoelectricity and ferroelectricity in NBT ceramics and its solid solutions with BaTiO_3 . The electrical and electromechanical properties of ceramics, textured ceramics and single crystals, either measured experimentally or calculated (estimated) from single crystal values, are reported. Also, typical characteristics of template particles for TGG and RTGG are also reviewed briefly.

Chapter 3 focuses on the processing issues mainly for the NBT-BT and SrTiO_3 systems, since SrTiO_3 template particles were used to texture NBT-BT ceramics. Various characterization methods were employed to quantify texture, including the Lotgering

factor, rocking curves and pole figures. NBT-BT ceramics were also textured using $\text{Bi}_4\text{Ti}_3\text{O}_{12}$ template particles. The key issues in this approach are addressed.

The experimental polarization (P_i), dielectric (ϵ_{ij}) and piezoelectric (d_{ijk}) properties of the random and textured ceramics are reported in Chapter 4. Properties are explained qualitatively in relation to the crystal symmetry of the ceramic.

The texture characterization methods mentioned in Chapter 3 are bulk characterization methods. Another texture characterization method called OIM (Orientation Imaging Microscopy) or EBSD (Electron Backscatter Diffraction) can supply orientation information of specific points on the sample surface. The results obtained using this characterization method are reported in Chapter 5.

In Chapter 6 the macroscopic physical properties of randomly oriented and highly textured rhombohedral 3m ceramic were estimated by averaging single crystal values of a similar material system. The orientation dependence of macroscopic physical properties were explained on the basis of crystallography. The trends in the experimentally measured values and calculated values were discussed in detail.

1.4 REFERENCES

1. K. Uchino, Ferroelectric Devices. Marcel Decker, Inc., New York (2000).
2. J. W. Wanders, Piezoelectric Ceramics: Properties and Applications. Philips Components, Eindhoven, The Netherlands (1991).
3. B. Jaffe, W. R. Cook, and H. Jaffe, Piezoelectric Ceramics. Academic Press, New York (1971).
4. U.S. Department of Defense, Military Standards: Piezoelectric Ceramic Material and Measurements Guidelines for Sonar Transducers. MIL-STD-1376B(SH). Naval Sea Systems Command, Arlington, VA (1995).
5. S. E. Park and T. R. ShROUT, "Ultrahigh Strain and Piezoelectric Behavior in Relaxor Based Ferroelectric Single Crystals," *J. Appl. Phys.*, **82** [4] pp. 1804-11 (1997).
6. S. H. Hong, S. Trolier-McKinstry, and G. L. Messing, "Dielectric and Electromechanical Properties of Textured Niobium-Doped Bismuth Titanate Ceramics," *J. Am. Ceram. Soc.*, **83** [1] pp. 113-118 (2000).
7. T. Tani, "Crystalline-Oriented Piezoelectric Bulk Ceramics with a Perovskite-type Structure," *J. Kor. Phys. Soc.*, **32** S1217-20 (1998).
8. B. Brahmaroutu, Templated Grain Growth of Textured Strontium Niobate Ceramics. Ph.D. thesis, Penn State University (1999).
9. C. Duran, Fabrication and Electrical Properties of Textured $\text{Sr}_{0.53}\text{Ba}_{0.47}\text{Nb}_2\text{O}_6$ Ceramics Prepared by Templated Grain Growth. Ph.D. thesis, Penn State University (2001).

10. X. H. Du, U. Belegundu, and K. Uchino, "Crystal Orientation Dependence of Piezoelectric Properties in Lead Zirconate Titanate: Theoretical Expectation for Thin Films," *Jpn. J. Appl. Phys.*, **36** [9A] pp. 5580-5587 (1997).
11. T. Takenaka, K. Maruyama, and K. Sakata, " $\text{Na}_{1/2}\text{Bi}_{1/2}\text{TiO}_3\text{-BaTiO}_3$ System for Lead-Free Piezoelectric Ceramics," *Jap. J. Appl. Phys.*, **30** [9b], 2236-9 (1991).
12. Y. M. Chiang, G. W. Farrey, A. N. Soukhojak, "Lead-Free High-Strain Single-Crystal Piezoelectrics in the Alkaline-Bismuth-Titanate Perovskite Family," *Applied Physics Letters*, **73**, 3683 (1998).

Chapter 2

LITERATURE REVIEW

2.1 INTRODUCTION

Piezoelectric materials are used in medical ultrasonic devices, ultrasonic motors, vibration dampers, sonar, and electromechanical positioners [1]. The materials of choice are usually lead-based perovskites due to their superior electrical and electromechanical properties. However, the toxicity of lead is a concern. As a result, there is an ongoing search for lead free piezoelectric ceramics. $(\text{Na}_{1/2}\text{Bi}_{1/2})\text{TiO}_3$ and its solid solutions are one of the candidates that draws attention [2]. Domain engineered BaTiO_3 , KNbO_3 and $\text{Ba}(\text{Zr}_{1-x}\text{Ti}_x)\text{O}_3$ single crystals are also being considered [3-5]. The ideas behind domain engineering of perovskite single crystals were proposed by Park and Shrout [6].

It has been shown that $\text{Pb}(\text{Zn}_{1/3}\text{Nb}_{2/3})\text{O}_3\text{-PbTiO}_3$ and $\text{Pb}(\text{Mg}_{1/3}\text{Nb}_{2/3})\text{O}_3\text{-PbTiO}_3$ single crystals with rhombohedral symmetry have remarkable piezoelectric properties in the $\langle 001 \rangle_{\text{pc}}$ (pc=pseudo-cubic) [6]. Unipolar strains as high as 1.7%, piezoelectric coefficients (d_{33}) of 2500 pC/N, and an electromechanical coupling coefficient (k_{33}) of >0.9 have been reported [7]. The origin of the high piezoelectric response is believed to be rotation of the polarization from the $\langle 111 \rangle_{\text{pc}}$ towards the $\langle 001 \rangle_{\text{pc}}$ axis with applied electric field. The success of this mechanism appears to be tied to a diverging d_{15} coefficient associated with the presence of a lower symmetry (monoclinic or orthorhombic) phase transition, Figure 2.1 [8-11]. The domain configuration of $\langle 001 \rangle_{\text{pc}}$ oriented rhombohedral crystals was found to be stable, giving hysteresis-free strain curves, unlike those of $\langle 111 \rangle_{\text{pc}}$ oriented single crystals. Rhombohedral crystals poled and

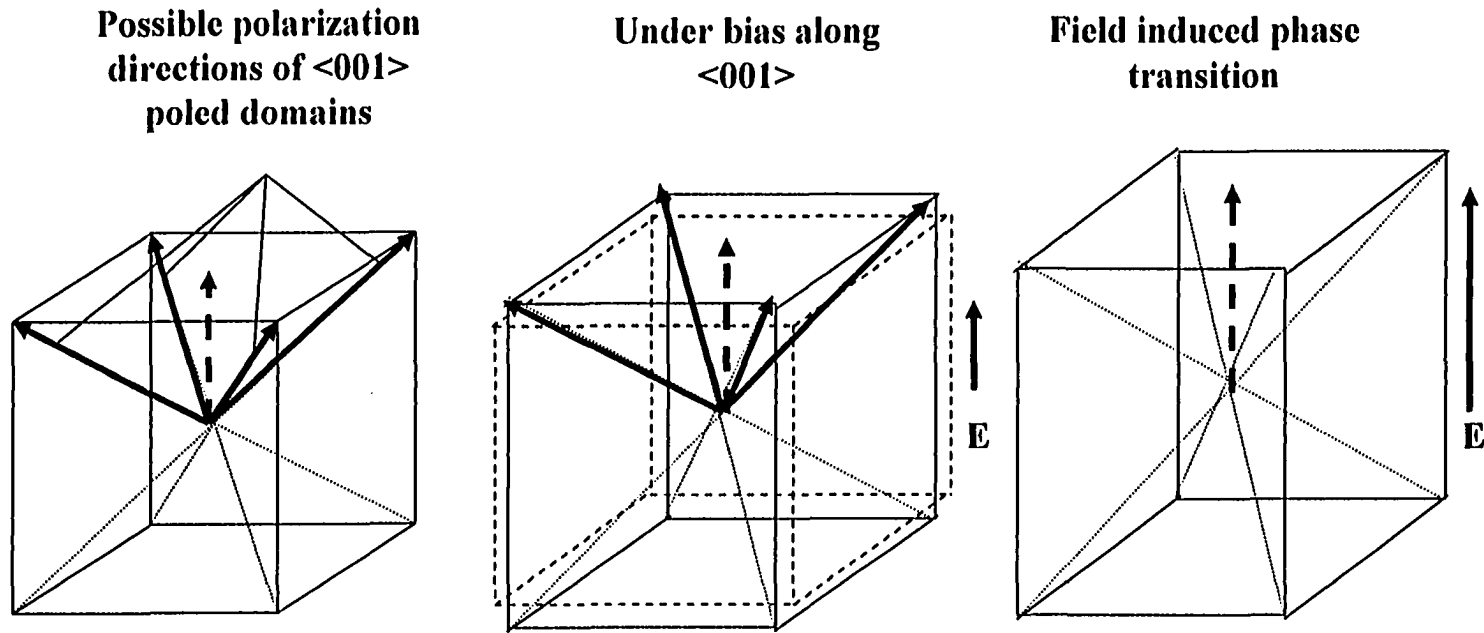


Figure 2.1. Schematic of engineered domain configuration for $\langle 001 \rangle$ poled rhombohedral crystals [6].

measured in the $\langle 111 \rangle_{pc}$ direction showed $k_{33} < 50\%$ and $d_{33} \sim 100$ pC/N [3]. It has been suggested that $\text{Na}_{1/2}\text{Bi}_{1/2}\text{TiO}_3$ benefits from the same type of domain engineering [2].

2.2 SODIUM BISMUTH TITANATE AND ITS SOLID SOLUTIONS

The presence of ferroelectricity in $\text{Na}_{1/2}\text{Bi}_{1/2}\text{TiO}_3$ (NBT) was first reported by Smolenskii et al. [12]. Since then, there have been many studies on $\text{Na}_{1/2}\text{Bi}_{1/2}\text{TiO}_3$ and its solid solutions with other perovskites like BaTiO_3 , SrTiO_3 , CaTiO_3 , and PbTiO_3 , both in polycrystalline and single crystal form.

The crystal structure of $\text{Na}_{1/2}\text{Bi}_{1/2}\text{TiO}_3$ is perovskite (Figure 2.2) with a rhombohedral distortion at room temperature ($R3c$ symmetry) [13-15]. The lattice parameter is 3.89 Å and the rhombohedral distortion angle is small ($\alpha = 89.6^\circ$) [16]. The Na^+ and Bi^{3+} ions are believed to be approximately randomly distributed over the 12-fold cubooctahedral sites. The existence of short-range cation ordering has been reported, in one neutron scattering study [17]. However, Jones and Thomas [14] reported that no ordering is present in the cubic phase, based on another neutron diffraction study. There are two temperature induced phase transitions in $\text{Na}_{1/2}\text{Bi}_{1/2}\text{TiO}_3$. The first one is at 230°C between rhombohedral ferroelectric ($R3c$) \leftrightarrow and a tetragonal phase, and the second one is at 520°C between the tetragonal \leftrightarrow cubic phases ($Pm3m$) [13]. There is controversy in the tetragonal structure rietvelt refinement of the crystal structure.

There are conflicting results reported about the crystallography and dielectric character of the intermediate tetragonal phase. Early reports with double hysteresis in the polarization-electric field curve and a transition temperature shift in biased dielectric

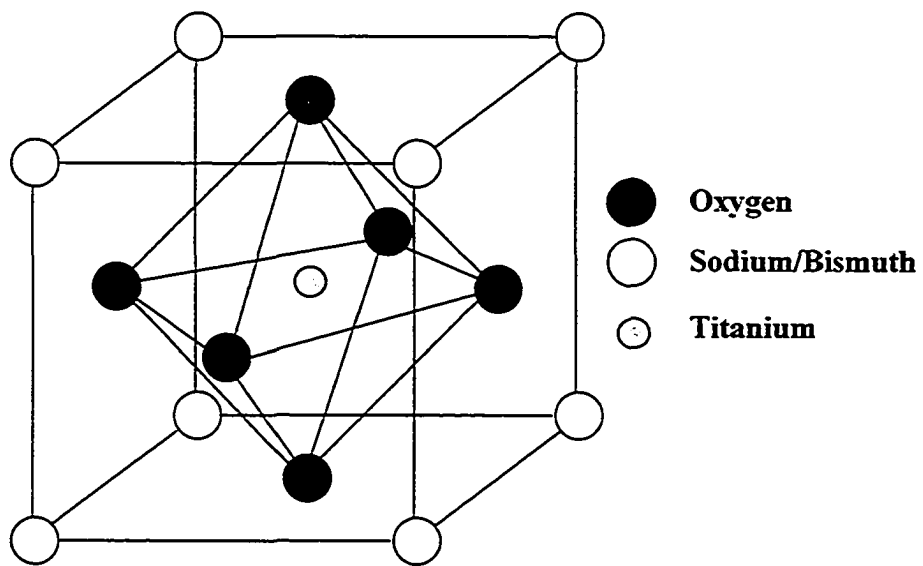


Figure 2.2. Schematic of prototype perovskite structure ($m\bar{3}m$ symmetry).

measurements, were cited as proof for antiferroelectricity [18] (see Figure 2.3). In the same figure, the remanent polarization is also given as a function of temperature. The absence of polarization in the tetragonal region is compatible with the loss (or at least decrease) of ferroelectricity at this temperature. However, some groups have reported an absence of superlattice reflections due to the cell doubling in the XRD (x-ray diffraction) pattern, and no change in the domain pattern [19]. Recent neutron diffraction work, however, does report weak superlattice reflections [14] for the high temperature tetragonal phase. Superstructure reflections of the type h odd, k odd, and l even were observed. Crystal structure refinements reveal an $a^0a^0c^+$ octahedral tilt (Glazer notation) with a tetragonal unit cell given by $2^{1/2}ax2^{1/2}bxc$. Glazer [20] developed a standard notation to describe octahedral tilting distortions in perovskites. The notation describes a tilt system by rotations of BO_6 octahedra about any of three orthogonal Cartesian axes. In Glazer notation [20], the letters indicate the magnitude of the rotation about a given axis, e.g., the letters a , b , and c imply unequal tilts about the x , y , and z axes. Superscript denotes the phase of the octahedral tilting in neighboring layers. A positive superscript would denote the neighboring octahedra tilt in the same direction (in-phase) and a negative superscript implies the tilts of neighboring octahedra tilt in the opposite direction (out of phase). A superscript of 0 signifies no tilting about that axis. As a result for tetragonal NBT there was cell doubling in the $[100]$ and $[010]$ directions but not in the $[001]$ direction [14]. The space group was suggested to be $P4bm$ from Rietveld refinement of neutron diffraction data [14]. In the space group it is suggested that the Bi^{3+} and Ti^{4+} cations are displaced in opposite directions along the c axis so there is nearly no

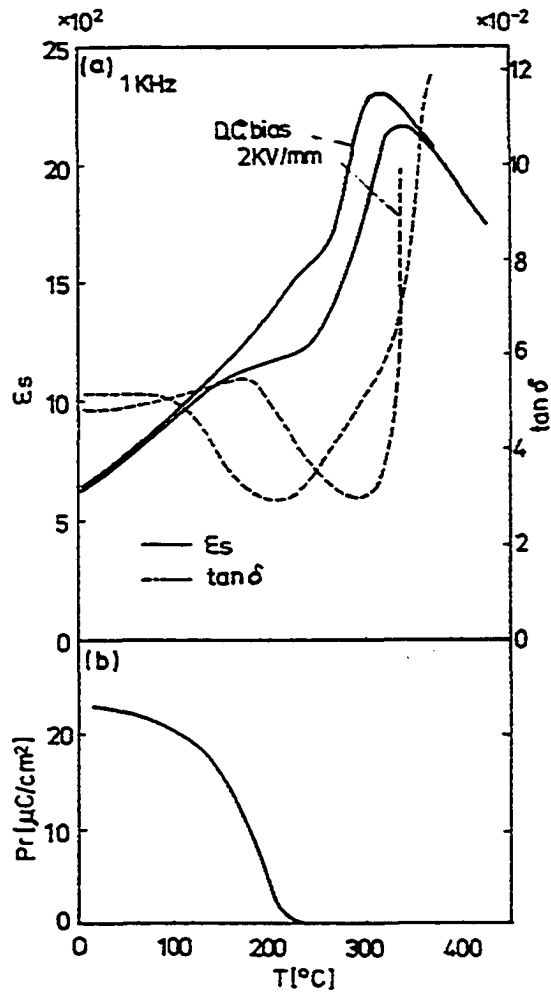


Figure 2.3. (a) Temperature dependence of dielectric constant and $\tan \delta$ for $\text{Na}_{1/2}\text{Bi}_{1/2}\text{TiO}_3$ ceramics at dc biases of 0 and 2 kV/mm. (b) Temperature dependence of remanent polarization for $\text{Na}_{1/2}\text{Bi}_{1/2}\text{TiO}_3$ ceramics determined from pyroelectric measurement [18].

polarization in the structure. However, the presence of weak polarization was suggested by a small second harmonic generation signal [14]. This tetragonal phase is ferroelastic. It is also possible that any disorder in the tilt systems may break-up the long range polarization of the ferroelectric phase.

It is possible that above 230°C, the intermediate region has co-existing rhombohedral (ferroelectric) and tetragonal (non-ferroelectric) phases. Neutron scattering [14, 21] studies confirmed that in the diffuse phase transition region both tetragonal and rhombohedral phases co-exist. They suggested that on cooling, initially unstable polar regions become stable, and finally become the nuclei for the low temperature ferroelectric phase [14]. The regions of mixed phases as a function of temperature were shown in Figure 2.4 [14].

From the specific heat measurements, no anomaly has been observed at the dielectric maximum temperature (320°C) [22].

Antonenko et al. optically studied the domain structure of $\text{Na}_{1/2}\text{Bi}_{1/2}\text{TiO}_3$ single crystals using a polarized light microscope [19]. In his study, no influence of electric field on the domain structure was observed, instead a single domain state was only achieved by applying mechanical stress at high temperature and was preserved upon cooling to room temperature. This is consistent with ferroelastic behavior. The domain structure was observed till 520°C, above which it vanished. This is the transition temperature from the tetragonal to cubic phase. Other authors have confirmed the low mobility of the ferroelastic domain walls [13, 23].

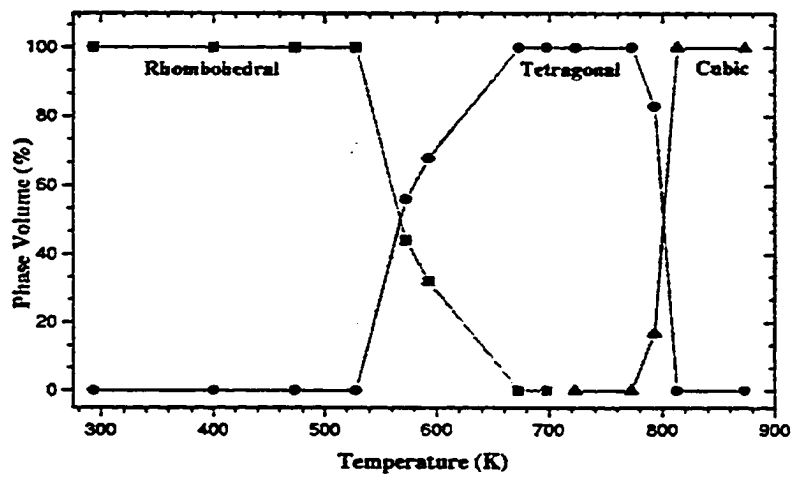


Figure 2.4. Regions of co-existing $\text{Na}_{1/2}\text{Bi}_{1/2}\text{TiO}_3$ phases as a function of temperature [14].

Soukhojak et al. [24] investigated the temperature dependence of the domain patterns of flux grown $\text{Na}_{1/2}\text{Bi}_{1/2}\text{TiO}_3$ single crystal as function of temperature using TEM (Transmission Electron Microscopy). He reported that domains disappeared on heating at 200°C and likewise reappeared at the same temperature on cooling, producing the previous domain pattern. This is unusual because once the domain pattern disappears on heating, usually another domain pattern should reappear on cooling. Park et al. [25] optically studied the domain pattern of $\text{Na}_{1/2}\text{Bi}_{1/2}\text{TiO}_3$ single crystals and reported that domain pattern disappeared on heating at 200°C and reappeared at higher temperatures 320°C which is not observed in Soukhojak's TEM study.

Relaxor behavior has been reported for PbTiO_3 modified $\text{Na}_{1/2}\text{Bi}_{1/2}\text{TiO}_3$ ceramics [16]. The permittivity and dielectric loss of $\text{Na}_{1/2}\text{Bi}_{1/2}\text{TiO}_3$ rich solid solutions show a strong temperature and frequency dependence. The permittivity decreased and its maximum shifted to higher temperatures with increasing frequency. The morphotropic phase boundary is located between 12-18 mol% PbTiO_3 . Similarly, doping with SrTiO_3 resulted in relaxor behavior in $\text{Na}_{1/2}\text{Bi}_{1/2}\text{TiO}_3$, however the transition temperatures (the temperature where dielectric constant is maximum) have been found to decrease by $-5.3^\circ\text{C}/\text{mol SrTiO}_3$ [26]. Likewise, the rhombohedral to tetragonal transition temperature is also shifted to lower temperature.

Ferroelectric $\text{Na}_{1/2}\text{Bi}_{1/2}\text{TiO}_3\text{-BaTiO}_3$ with low BaTiO_3 concentrations has rhombohedral point group symmetry, often reported as 3m with a small rhombohedral distortion at room temperature [21]. The structure of the $\text{Na}_{1/2}\text{Bi}_{1/2}\text{TiO}_3\text{-BaTiO}_3$ solid solution becomes tetragonal with increasing BaTiO_3 . The morphotropic phase boundary

is located at ~6.5 mol% BaTiO₃ [23] as shown in Figure 2.5. It is worth noting that the phase diagram has been redrawn relative to the published one. In particular, the phase which develops at ~230°C in pure Na_{1/2}Bi_{1/2}TiO₃ was originally described as antiferroelectric. It has subsequently been shown that this “phase” is a mixture of ferroelectric rhombohedral and non-ferroelectric tetragonal material for pure Na_{1/2}Bi_{1/2}TiO₃. How the nature of the phase changes as BaTiO₃ is added is not known. For lack of additional information, it was assumed that the entire area was the same, two-phase mixture. Secondly, the cubic (paraelectric) to tetragonal (paraelectric) phase transition temperature (520°C for Na_{1/2}Bi_{1/2}TiO₃) was added as a dotted line. However the cubic to tetragonal transition temperature as a function of BaTiO₃ doping is not known, so an arbitrary slope is given to the line. It is presumed that the stability of this phase decreases as BaTiO₃ is added, since BaTiO₃ itself has a cubic prototype phase. In any event, it is clear that all of the ferroelectric phases near the MPB are cooled through a tetragonally distorted ferroelastic phase.

Single crystals of Na_{1/2}Bi_{1/2}TiO₃ have been grown by high temperature flux methods in which excess Na₂CO₃ and Bi₂O₃ are usually used as the flux [2]. In work by Chiang and co-workers, the melt was slowly cooled from 1350°C at a rate of 5°C/hr. The obtained crystals were cut in the <001>_{pc} direction for measurements. Among the crystals grown, the one with 5.5 mol% BaTiO₃ doped was rhombohedral and showed 0.24% free strain at 60 kV/cm, Figure 2.6. About 20% hysteresis was reported for the same sample.

Park et al. studied single crystals of Na_{1/2}Bi_{1/2}TiO₃ grown by the flux technique and the Czochralski method [13]. The melting point of Na_{1/2}Bi_{1/2}TiO₃ was found to be at

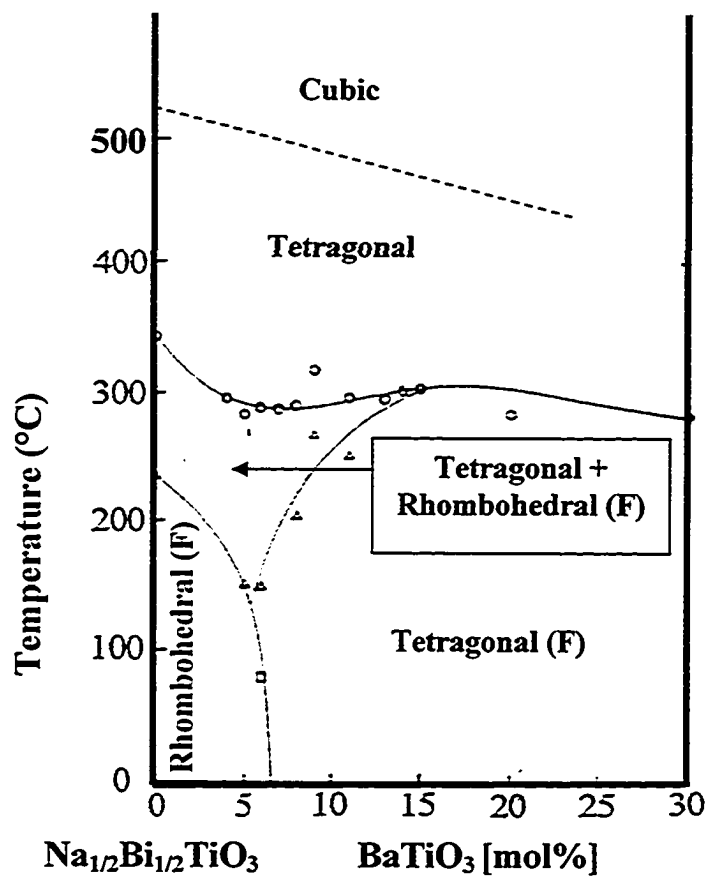


Figure 2.5. Modified phase diagram of $\text{Na}_{1/2}\text{Bi}_{1/2}\text{TiO}_3$ - BaTiO_3 system [27]

(F=Ferroelectric).

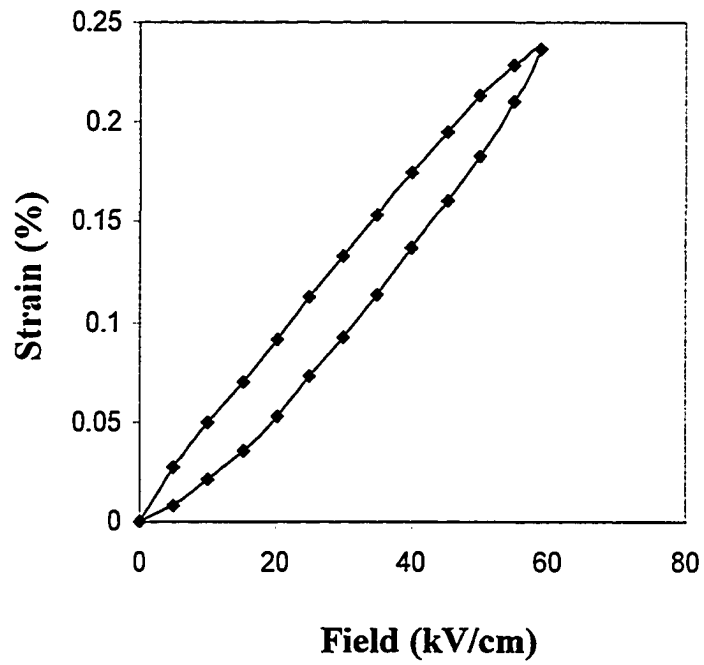


Figure 2.6. Unipolar strain curve for 5.5 mol% BaTiO₃ doped Na_{1/2}Bi_{1/2}TiO₃ single crystal actuated along <001>_{pc}, data from [2].

1290°C. Based on the evidence of Na₂O-TiO₂ rich second phases, they concluded that Na_{1/2}Bi_{1/2}TiO₃ melts incongruently. Crystals grown by the Czochralski method were nonstoichiometric due to Bi volatilization. Flux grown crystals had more rhombohedral distortion. Unipolar strain curve of Na_{1/2}Bi_{1/2}TiO₃-2 mol% PbTiO₃ single crystal oriented in the <001>_{pc} were almost hysteresis free, but the piezoelectric coefficient measured from the slope of the strain vs. electric field curve was low (166 pC/N) [28] as shown in Figure 2.7.

Na_{1/2}Bi_{1/2}TiO₃ has a transition temperature of T_{tr}~230°C (where the transition from rhombohedral to tetragonal starts) and a large room temperature remanent polarization of 38 μC/cm² [23]. In the <001>_{pc} direction, a d₃₃ coefficient as high as 450 pC/N [2] has been reported for flux grown single crystals at the morphotropic phase boundary with BaTiO₃, Figure 2.5 [27]. MPB composition polycrystalline ceramics on the other hand, have been reported to have d₃₃ values of 125 pC/N, d₃₁ of -40 pC/N, d₁₅ of 194, and k₃₃ of 55% [23].

Herabut et al. [29] studied La doped Na_{1/2}Bi_{1/2}TiO₃ ceramics and reported improvements in the piezoelectric properties. The highest piezoelectric coefficient reported was (d₃₃) 91 pC/N when ~2 at.% La was present. The Curie temperature was low (~100°C), grain size was small (<10 μm) and second phases appeared in the microstructure.

Mn additions have been found to enhance the electrical resistivity (3x10¹⁴ Ωcm @ 40°C and 0.2 wt% MnCO₃) of NBT at the expense of decreasing the Curie temperature (T_c). The shift in the T_c was reported to be ~-110°C/wt% MnCO₃ additions [30]. Grain

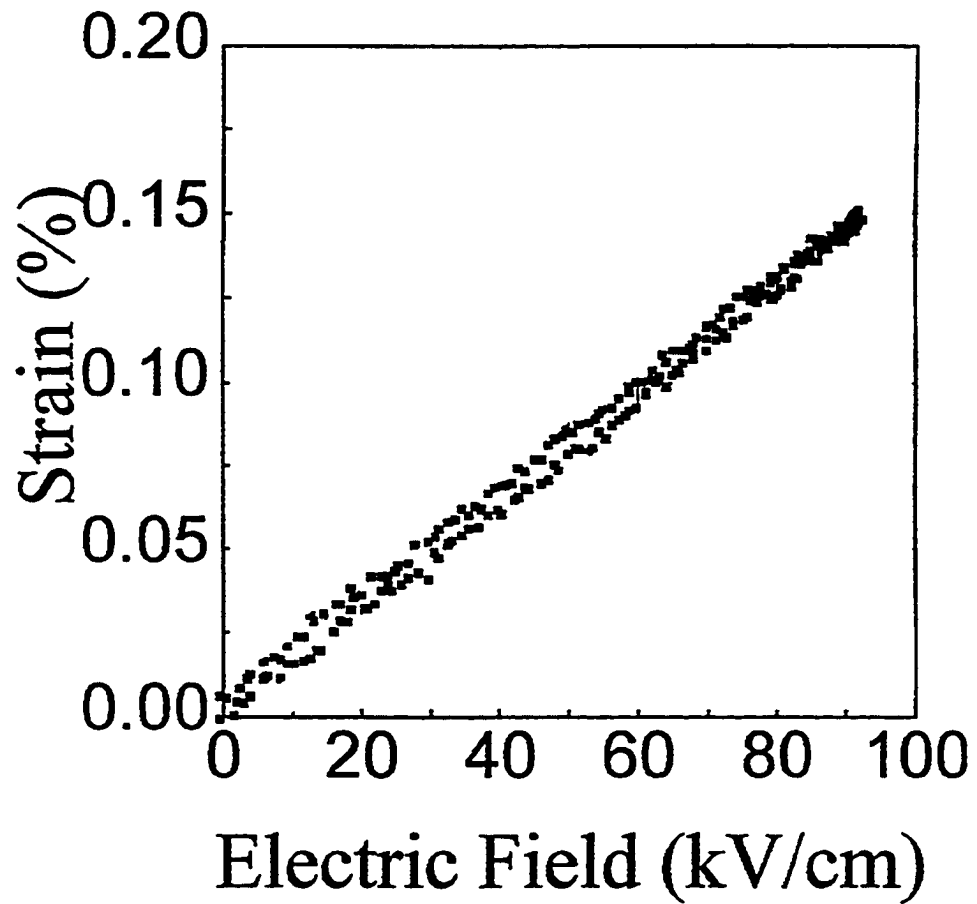


Figure 2.7. Strain behavior of 2% PbTiO₃ doped Na_{1/2}Bi_{1/2}TiO₃ single crystal [28].

growth was also promoted and the coercive field decreased for small concentrations of MnCO_3 , <0.5 wt% [30].

It is clear from the review of the literature that the largest piezoelectric coefficients observed to date in $\text{Na}_{1/2}\text{Bi}_{1/2}\text{TiO}_3$ -based single crystals are coupled with substantial hysteresis. One possible cause for high hysteresis [2] in unipolar strain curves is related to the high temperature ferroelastic phase transition. The ferroelastic domain structure is set at high temperature, and does not move with electric field. It is possible that the presence of this domain structure imposes some type of restoring force on the ferroelectric domain walls, so that an electric field applied to the rhombohedral phase only temporarily moves the domain boundary. If the field is removed the original domain configuration may be recovered, yielding appreciable hysteresis. The work of Park et al. [28] shown in Figure 2.7 suggests that this situation may be avoidable. An alternative explanation might be that the electric field required to induce a tetragonal phase transition is low in $\text{Na}_{1/2}\text{Bi}_{1/2}\text{TiO}_3$ - BaTiO_3 system. This would be consistent with the substantial poling strain observed in the work of Chiang and co-workers [2]. If so, then the extent of hysteresis should depend on proximity to the MPB. A third possibility is that the large hysteresis is associated with either microheterogeneity or large concentrations of point defects. This is reasonable to consider in $\text{Na}_{1/2}\text{Bi}_{1/2}\text{TiO}_3$ due to the volatility of Na, Bi, and O.

Given the controversy in the magnitude of the piezoelectric responses available in $\text{Na}_{1/2}\text{Bi}_{1/2}\text{TiO}_3$ -family materials, as well as the substantial hysteresis observed in many cases, the study was aimed at further investigating the properties, although this time

oriented polycrystalline ceramics were considered. It was hoped that the ability to prepare oriented samples across the MPB would shed some light on the origin of the hysteresis.

2.3 ELECTRICAL AND ELECTROMECHANICAL PROPERTIES OF TEXTURED PIEZOELECTRIC CERAMICS

All crystalline materials show anisotropy in some of their property coefficients. However, due to the random orientation of the crystals (i.e. grains) in a ceramic, averaging of the anisotropic piezoelectric response typically results in lower properties than those displayed by properly oriented single crystals. The macroscopic symmetry in these ceramics is $\infty\infty m$, spherical symmetry (see Figure 2.8) [31]. The symmetry changes to ∞m (conical symmetry) after poling of a ferroelectric, due to alignment of the dipoles along the electric field direction, in accordance with the Curie symmetry superposition principle. The resulting symmetry allows the appearance of the piezoelectric effect as well as other properties. This is extremely useful, and is the basis for the piezoelectric response of piezoelectric ceramics like $\text{Pb}(\text{Zr}_{0.52}\text{Ti}_{0.48})\text{O}_3$. However, the resulting properties are below the single crystal properties calculated on the basis of phenomenology for appropriately oriented single crystals [32]. The properties of the ceramic can be increased if the crystallographic orientation of the grains/domains are controlled by texturing. Higher dielectric, pyroelectric, and piezoelectric properties have been demonstrated in fiber textured $\text{Pb}(\text{Mg}_{1/3}\text{Nb}_{2/3})\text{O}_3$ -32.5% PbTiO_3 [33], $(\text{Sr},\text{Ba})\text{Nb}_2\text{O}_6$ [34], $\text{Bi}_4\text{Ti}_3\text{O}_{12}$ [35-37], PbNb_2O_6 [38], BaTiO_3 [39, 40], $\text{Na}_{0.475}\text{Ca}_{0.05}\text{Bi}_{4.475}\text{Ti}_4\text{O}_{15}$ [41], $\text{CaBi}_4\text{Ti}_4\text{O}_{15}$ [41].

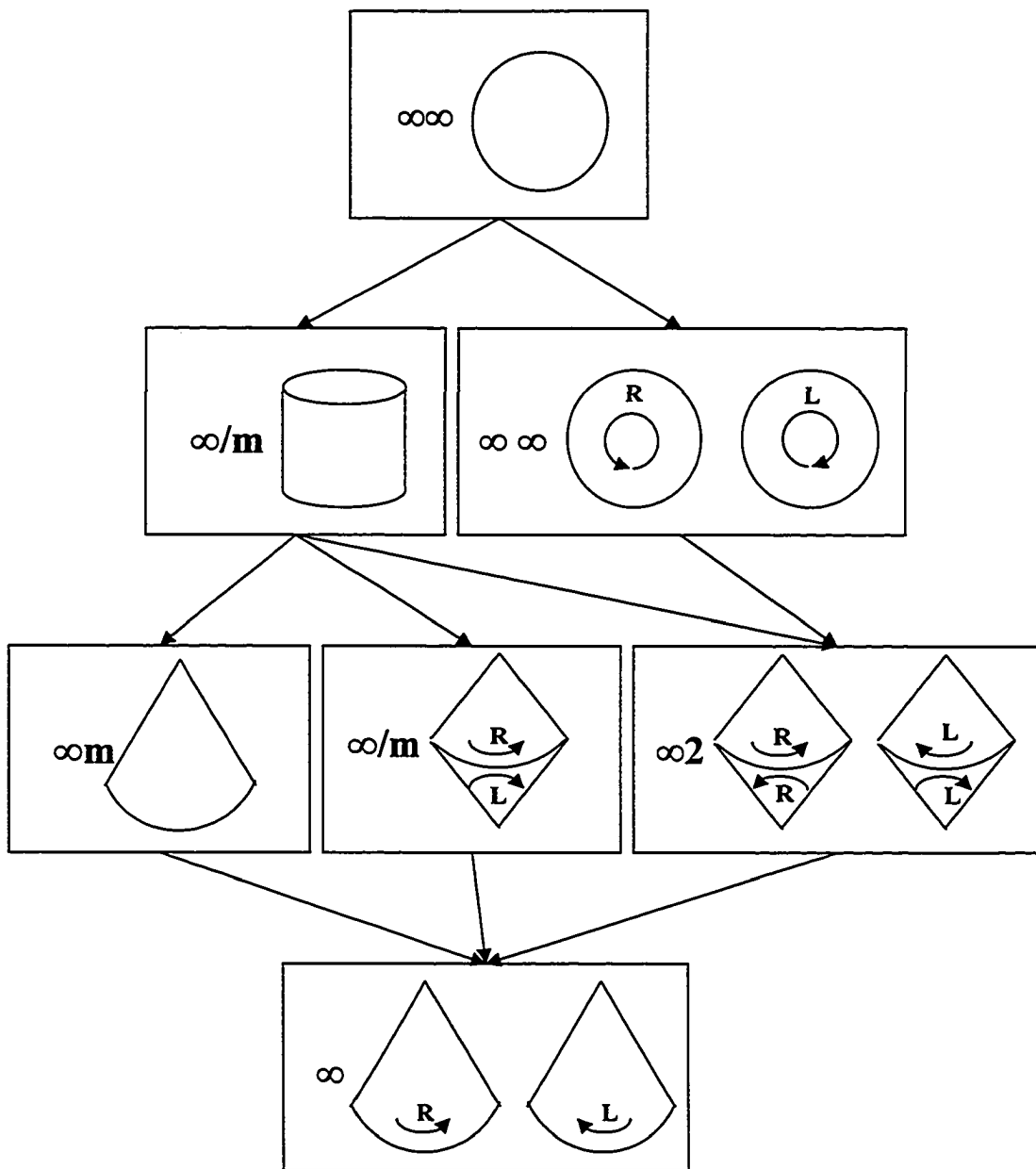


Figure 2.8. Curie groups showing subgroup-supergroup relations [31].

Sabolsky et al. [33] showed that $\langle 001 \rangle_{pc}$ fiber-textured $\text{Pb}(\text{Mg}_{1/3}\text{Nb}_{2/3})\text{O}_3$ –32.5% PbTiO_3 ceramics have enhanced piezoelectric, electromechanical coupling and compliance coefficients. The composition he studied had rhombohedral (3m) symmetry. The d_{33} coefficients of the highly textured $\text{Pb}(\text{Mg}_{1/3}\text{Nb}_{2/3})\text{O}_3$ –32.5% PbTiO_3 ceramics were 1.2 to 1.5 times greater than randomly oriented ceramics. He also reported hysteresis in unipolar strain curves of the textured ceramics which was absent in domain engineered $\text{Pb}(\text{Mg}_{1/3}\text{Nb}_{2/3})\text{O}_3$ –32.5% PbTiO_3 single crystals. He attributed the presence of hysteresis to the mechanical clamping due to the residual random ceramic as well as the BaTiO_3 templates (which affect the poling efficiency and the stability of domain configurations).

Duran et al. [34] showed that [001] fiber-textured $(\text{SrBa})\text{Nb}_2\text{O}_6$ ceramics have enhanced pyroelectric, dielectric and piezoelectric properties. The composition studied had tetragonal (4mm) symmetry. He found that there is a close correlation between texture fraction and electrical and electromechanical properties. These two examples clearly demonstrate that if the grains are oriented in the right crystallographic direction, it is possible to enhance the physical properties of a ceramic.

Grain oriented $(\text{Na,K})_{1/2}\text{Bi}_{1/2}\text{TiO}_3$ (NKBT) ceramics were prepared by Tani's group by a reactive templated grain growth method using plate-like $\text{Bi}_4\text{Ti}_3\text{O}_{12}$ particles for templates [42-44]. Plate-like $\text{Bi}_4\text{Ti}_3\text{O}_{12}$ particles were aligned parallel to the tape casting direction to act as templates for oriented growth of $(\text{Na,K})_{1/2}\text{Bi}_{1/2}\text{TiO}_3$. A Lotgering factor of 92% was achieved and improvements in the electrical properties like dielectric constant (9% increase to 644), planar coupling coefficient (46% increase to

0.43), piezoelectric coefficient d_{31} (71% increase to -63 pC/N) were attributed to the increased crystallographic orientation [42-45].

The mechanism of texture development in RTGG (reactive templated grain growth) of $(\text{Na,K})_{1/2}\text{Bi}_{1/2}\text{TiO}_3$ using $\text{Bi}_4\text{Ti}_3\text{O}_{12}$ platelets was investigated by TEM (transmission electron microscopy) [42-43]. The reaction between $\text{Bi}_4\text{Ti}_3\text{O}_{12}$ templates and the matrix powder was initiated at the template surface and resulted in full conversion of the template particles to the perovskite structure while maintaining the orientation set during the forming process. The reaction probably occurs by solid state diffusion of Na and Ti atoms into the template particles [45]. First, platelet like $(\text{Na,K})_{1/2}\text{Bi}_{1/2}\text{TiO}_3$ particles with $\langle 001 \rangle_{pc}$ orientation perpendicular to the sample surface formed, and then the grain growth took place [45].

2.4 MODELING OF STRUCTURE-PROPERTY RELATIONS OF RANDOM AND ORIENTED CERAMICS

A ceramic consists of many single crystals (grains) randomly oriented in space. In addition, each of these single crystals of the ceramic material are separated into domains with various symmetries, like 4mm (tetragonal), mm2 (orthorhombic), and 3m (rhombohedral). There has been great interest in predicting the macroscopic properties of the ceramic using the single crystal properties only. Fundamentally, the orientation distribution of the domains impacts the overall macroscopic properties, (as does misalignment of the neighbouring grains and the presence of other phases).

One of the ways that ferroelectric ceramics differ from ferromagnetic ceramics is that in most ferroelectric crystals it is not possible to rotate the polarization continuously

in the applied field direction [46]. However, this is not true for some relaxor ferroelectrics in which polarization rotation has been demonstrated [6]. The amount of field-forced domain rotation in $\text{Na}_{1/2}\text{Bi}_{1/2}\text{TiO}_3$ is not known.

One of the main assumptions in the theoretical treatment of polarization direction in each domain is that the polarization direction in each domain lies within a certain solid angle θ with respect to the direction of the electric field, and does not rotate. The angle of distribution depends on the magnitude of the field, the polarization conditions, and symmetry of the crystals [46]. In random ceramics, the minimum solid angle is determined by the allowed polarization directions (governed by the symmetry) and the requirement for a uniform distributed set of orientations. In contrast, in textured ceramics, the minimum solid angle is the same as in random ceramics but the distribution (pole density) is not uniform. The anisotropy, which is an inherent property of the single crystals, is now reflected more effectively in the macroscopic properties of the textured polycrystals.

There have been many attempts to estimate the macroscopic physical properties of polycrystalline materials [47-50]. Analytical expressions relating the piezoelectric properties of single crystals and polycrystals have been studied previously. In most cases, a number of simplifying assumptions were made, including disregarding the mechanical interactions between grains, as well as the existence of imperfections in the crystals [46, 51], and internal mechanical stresses in the ceramics developed during cooling from the sintering temperature. Therefore, the predictions are qualitative in nature and predict the maximum coefficients for these assumed ideal conditions.

The interactions between neighboring grains, which are related to the misorientation angle of one grain with respect to the grains surrounding it, play a crucial role in the overall (effective) macroscopic properties of polycrystalline materials [52]. For example, two piezoelectric grains, oriented differently with respect to the driving electric field, will strain in different amounts due to the inherent anisotropy in piezoelectric coefficient. The grain that strains more will be clamped by the neighboring grain that strains less. Therefore, the overall response of the polycrystalline aggregate to the electric field will be lowered relative to the single crystal. Another fact is that d_{31} in perovskite ferroelectrics is negative; that is, as the grain elongates along the electric field direction it contracts in the direction perpendicular to it. In a real ceramic, grains are attached to each other. The negative strain in the perpendicular direction is different for each grain due to random or non-ideal grain orientation distribution. So, piezoelectric elongation along the electric field will be further clamped to match strain between the grains.

Subnikov [48] was the first who studied the piezoelectric effect and texture in Rochelle salt. He derived the general relations describing the relations between the piezoelectricity and texture, along with the first experimental work on the piezoelectric properties of textured materials [49]. Rochelle salt is a comparatively easy case, because it is a uniaxial ferroelectric.

Shuvalov [46] studied the analytical relations (Eqn. 2.1) between the properties of ceramics and single crystals for tensors of different rank with tetragonal (4mm) and rhombohedral (3m) symmetry. He showed that

$$d_{33}(\text{ceramic}) = \frac{1}{4}(1 + \cos\theta)[(1 + \cos^2\theta)d_{33} + \sin^2\theta(d_{15} + d_{31})] \quad \text{Eqn. 2.1}$$

where θ is the solid angle of distribution of orientations. Those derived relations have the solid angle of distribution as a variable in the equations but do not take into account non-random distribution (texture) of grains. For a tetragonal BaTiO_3 ceramic, the piezoelectric coefficient was given as $0.79d_{ij}$ when 180° and 90° domain switching is allowed, that is when polarizations are within the smallest solid angle possible. The calculated values are often larger than the experimental values [46].

Redin et al. [50], by using an integral approach, systematically evaluated the average remanent polarization in the 10 polar classes of crystals. They calculated that the remanent polarization in a random ceramic with $4mm$ (90° and 180° domain switching) and $3m$ (180° , 71° and 109° domain switching) symmetry should be 83.1% and 86.6% of the single crystal values, respectively. The calculations were specific for $m3m$ as a prototype symmetry.

One of the methods employed in estimating the dielectric, piezoelectric, and elastic constants of polycrystalline materials from single crystal data is the use of Effective Medium Theory (EMT) [52]. This method has been successfully applied for thin films, bulk materials, and phase mixtures with different properties [51]. The benefit of this approach is that piezoelectric interactions between grains are accounted for. The clamping effect of the substrate in ferroelectric thin film applications can also be modeled.

In the work of Pertsev et al., the material properties are modeled by taking into account the interaction of a spherical single domain inclusion in a homogeneous

piezoelectric matrix (Figure 2.9) [52]. Eshelby's "equivalent inclusion technique", adapted to the piezoelectric case, was numerically solved for the piezoelectric inclusion in a dissimilar piezoelectric medium. Pertzev et al. [52] used EMT to estimate the dielectric and piezoelectric properties of 4mm symmetry BaTiO₃ and PbTiO₃ bulk and thin films as a function of normalized remanent polarization in the sample (a different way of expressing texture). The most important findings they report are a nonlinear change in the dielectric (Figure 2.10) and piezoelectric coefficients (Figure 2.11) with respect to the remanent polarization in the sample. The lowering of properties in thin films due to two dimensional clamping from the substrate was also described.

Nan et al. [47] studied the piezoelectric effect in polycrystalline BaTiO₃ ceramics by using linear averaging and effective medium theory to predict d_{33} , d_{31} and d_{15} using single crystal data. The anisotropy present in the BaTiO₃ single crystals was accounted for in their calculations, but matching of the strains in different grains were not accounted for. The predictions made using EMT were closer to the d_{33} , d_{31} and d_{15} values reported by Jaffe [53] than the linear averaging method.

Olson et al. [51] studied the macroscopic dielectric constant, bulk modulus and shear modulus of polycrystals with piezoelectric grains with 4mm symmetry. Grains with electromechanical coupling deform mechanically, which generates stresses on the neighboring grains that affect the overall macroscopic response of polycrystals. He assumed that the grains in the sample are neither completely clamped nor free. An intermediate state is accounted for in their calculations. The experimentally measured dielectric constant for unpoled BaTiO₃ ceramic (1400) agrees well with the predicted one (1320).

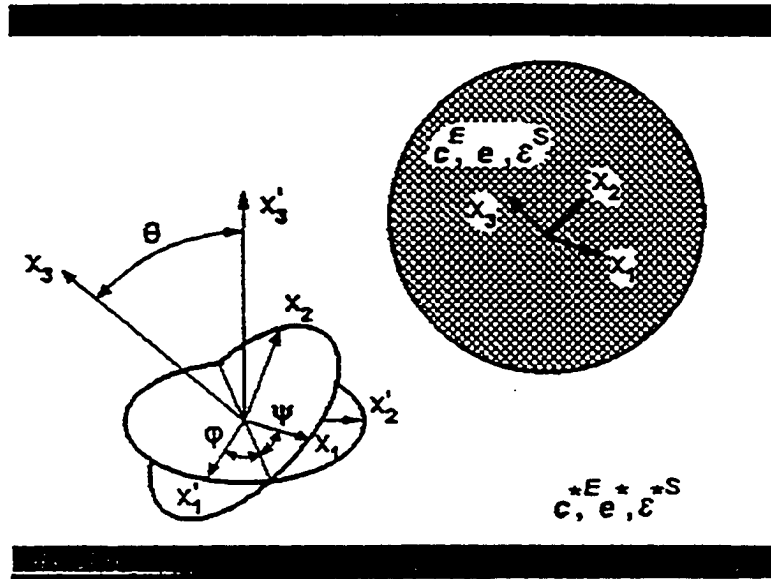


Figure 2.9. The drawing of the model system used in EMT [52]. Spherical ferroelectric crystal in a homogeneous piezoelectric matrix. The Euler angles ϕ , ψ , and θ relate the crystal coordinate system (x_1, x_2, x_3) to the sample coordinate system (x'_1, x'_2, x'_3) . c =elastic stiffness, e =piezoelectric constant, ϵ = permittivity, E =constant electric field, S = constant strain, $*$ =macroscopic property [52].

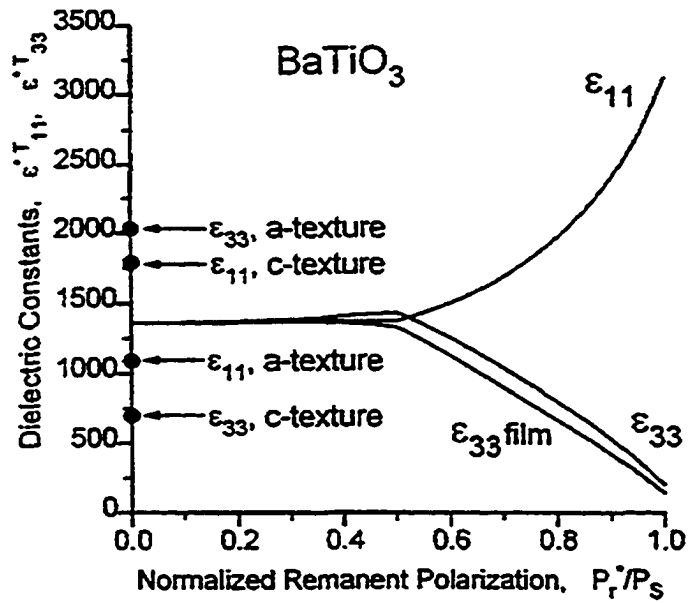


Figure 2.10. Relative dielectric constant of BaTiO₃ bulk ceramics vs. normalized polarization, calculated theoretically. $\epsilon_{33}^{\text{film}}$ represents the effect of clamping by the substrate on the dielectric constant of the thin film. The dielectric constant of unpoled c- and a-textured BaTiO₃ thin films are shown as dots [52].

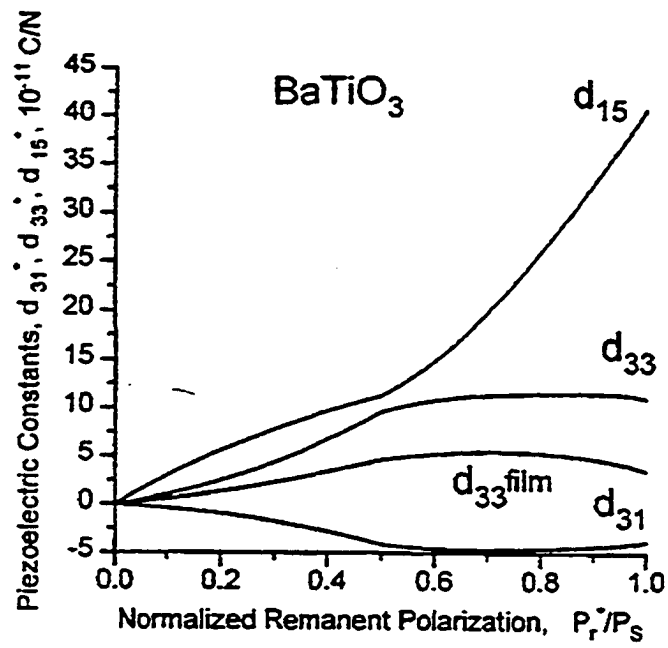


Figure 2.11. Piezoelectric charge coefficient vs. remanent polarization in bulk BaTiO_3 ceramics. d_{33}^{film} represents the macroscopic piezoelectric response of a BaTiO_3 film [52].

2.5 TEMPLATED GRAIN GROWTH AND TEMPLATE CHARACTERISTICS

There have been several ways of producing textured ceramics, e.g., tapecasting, extrusion, centrifugal casting, slip casting, sinter forging, or hot pressing [54-55]. In the TGG (templated grain growth) approach, anisotropically shaped template particles are aligned in a matrix powder by shear stress, Figure 2.12. Upon heat treatment, template particles coarsen at the expense of small size matrix grains (Figure 2.13) due to the size advantage. The presence of a liquid phase enhances material transport toward the template particles [33, 56].

The choice of template particle is also a critical parameter that needs attention. Not every anisotropically shaped particle can be used as a template. First of all, the template has to be chemically stable in the matrix powder at elevated temperatures. Furthermore, the crystal structure and lattice parameter of the template particle has to be similar to that of the matrix material in order to enable epitaxial growth on the template particle surface [33].

In certain cases, there might not be a suitable template particle available that satisfies the above mentioned requirements. Reactive template grain growth (RTGG) is another approach that might be used. In this case, first the template particles chemically react with the matrix powder and then grow at the expense of the fine matrix powder [39, 45]. During chemical reaction, the shape and single crystallinity of the template particle have to be conserved. Controlling the chemical reaction between the template particle and the matrix powder can control the degree of texture development [42-43].

The degree of texture in the resulting materials is strongly dependent on the degree of template alignment during the forming process, assuming the other

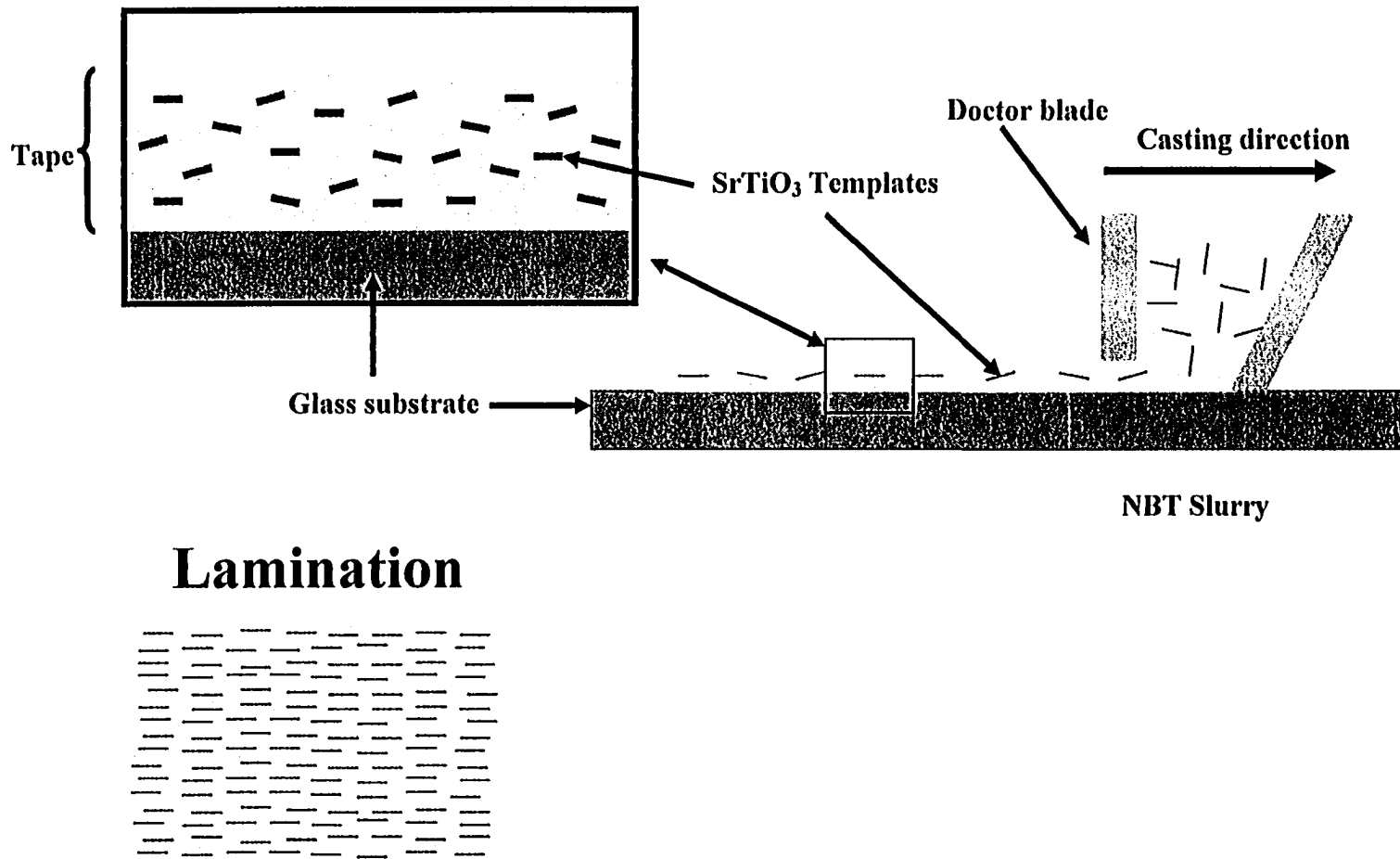


Figure 2.12. Schematic of template alignment in tape casting and sample preparation.

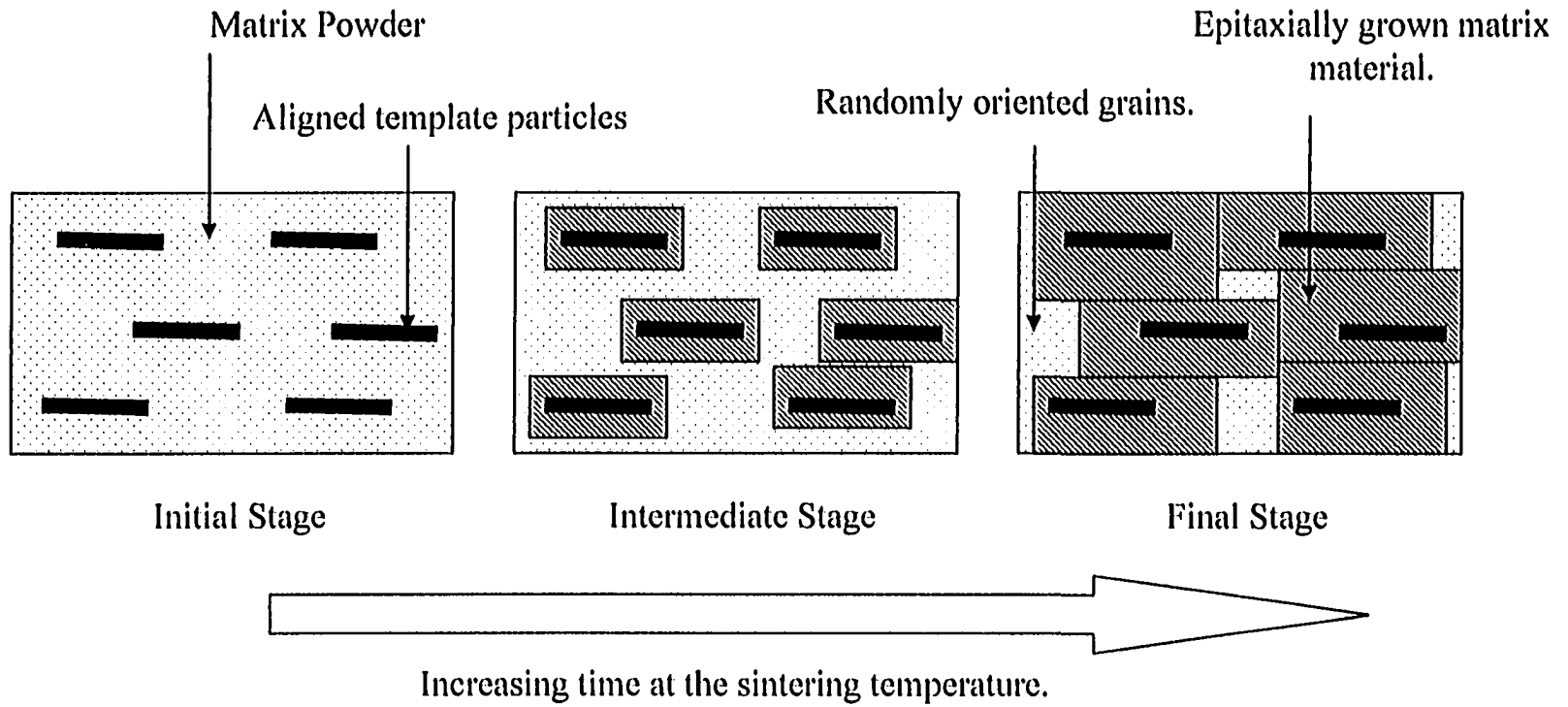


Figure 2.13. Schematic of templated grain growth at high temperatures from initial (green) stage to final stage.

requirements are fulfilled. It is the alignment of the template particles that determines the orientation of the grains in the sintered ceramics. This is how fiber-texture or biaxial texture is incorporated in the ceramic by TGG methods. If the template alignment is controlled biaxially, as in the case of blade-shaped templates, then the ceramic can be biaxially textured [55]. On the other hand, needle shaped or platelet shaped template particles yield fiber-textured ceramics [33, 38].

2.6 REFERENCES

1. K. Uchino, Ferroelectric Devices. Marcel Decker, Inc., New York (2000).
2. Y. M. Chiang, G. W. Farrey, A. N. Soukhovjak, "Lead-Free High-Strain Single-Crystal Piezoelectrics in the Alkaline-Bismuth-Titanate Perovskite Family," *Applied Physics Letters*, **73**, 3683 (1998).
3. S. E. Park, S. Wada, L. E. Cross, and T. R. ShROUT, "Crystallographically Engineered BaTiO₃ Single Crystals for High Performance Piezoelectrics," *J. Appl. Phys.*, **86** [5] pp. 2746-50 (1999).
4. P. W. Rehrig, S. E. Park, S. Trolier-McKinstry, G. L. Messing, B. Jones, and T. R. ShROUT, "Piezoelectric Properties of Zirconium-Doped Barium Titanate Single Crystals Grown by Templated Grain Growth," *J. Appl. Phys.*, **86** [3] pp. 1657-61 (1999).
5. P.W. Rehrig, *Templated Grain Growth of Perovskite Single Crystals*, Ph.D. Thesis, The Pennsylvania State University, University Park, PA (1999).
6. S. E. Park and T. R. ShROUT, "Ultrahigh Strain and Piezoelectric Behavior in Relaxor Based Ferroelectric Single Crystals", *J. Appl. Phys.*, **82** (4) 1804-1811 (1997).
7. S. E. Park and T. R. ShROUT, "Characteristics of Relaxor-Based Piezoelectric Single Crystals for Ultrasonic Transducers," *IEEE Trans. Ultrasonics, Ferroelectrics, and Frequency Control*, **44** [5] pp. 1140-47 (1997).
8. A. J. Bell, "Phenomenologically Derived Electric Field-Temperature Phase Diagrams and Piezoelectric Coefficients for Single Crystal Barium Titanate Under Fields Along Different Axes," *J. Appl. Phys.*, **89** [7] pp. 3907-14 (2001).

9. Z. G. Ye, "Relaxor Ferroelectric Complex Perovskites: Structure, Properties and Phase Transitions," *Key Eng. Mater.*, **155-56** pp. 81-122 (1998).
10. M. J. Haun, Z. Q. Zhuang, S. J. Jang, H. A. McKinstry, and L. E. Cross, "A Phenomenological Theory for the Second Order Region of the PZT Solid Solution System," in *Proc. 6th IEEE Int. Symp. App. Ferroelec.*, Lehigh, PA, 1986, pp. 398-401.
11. R. Guo, L. E. Cross, S. E. Park, B. Nohada, D. E. Cox, and G. Shirane, "Origin of High Piezoelectric Response in $\text{PbZr}_{1-x}\text{Ti}_x\text{O}_3$," *Phys. Rev. Lett.*, **84** [3] pp. 5423-26 (2000).
12. G. A. Smolenskii, V. A. Isupov, A. I. Agranovskaya, and N. N. Krainik, "New Ferroelectrics of Complex Composition IV," *Sov. Phys. Solid State*, **2** [11] pp. 2651-54 (1961).
13. S. E. Park, S. J. Chung, I. T. Kim, and K. S. Hong, "Nonstoichiometry and Long-Range Cation Ordering in Crystals of $(\text{Na}_{1/2}\text{Bi}_{1/2})\text{TiO}_3$," *J. Am. Ceram. Soc.*, **77** [10] pp. 2641-47 (1994).
14. G. O. Jones and P. A. Thomas, "Investigation of the Structure and Phase Transitions in the Novel A-site Substituted Distorted Perovskite Compound $\text{Na}_{1/2}\text{Bi}_{1/2}\text{TiO}_3$," *Acta Crystallographica*, **B58** [2] pp. 168-178 (2002).
15. G. O. Jones and P. A. Thomas, "The Tetragonal Phase of $\text{Na}_{1/2}\text{Bi}_{1/2}\text{TiO}_3$ – a New Variant of the Perovskite Structure," *Acta Crystallographica* **B56** [3] pp. 426-30 (2000).

16. S. Said, J. P. Mercurio, "Relaxor Behavior of Low Lead and Lead Free Ferroelectric Ceramics of the $\text{Na}_{1/2}\text{Bi}_{1/2}\text{TiO}_3\text{-PbTiO}_3$ and $\text{Na}_{1/2}\text{Bi}_{1/2}\text{TiO}_3\text{-K}_{1/2}\text{Bi}_{1/2}\text{TiO}_3$ Systems," *J. Eur. Cer. Soc.*, **21** pp. 1133-36 (2001).
17. S. B. Vakhrushev, B. E. Kvyatkovskii, R. S. Malysheva, N. M. Okuneva, and P. Symirkov, "Investigation of a Broad Phase Transition in $(\text{Na}_{1/2}\text{Bi}_{1/2})\text{TiO}_3$ by the Neutron Scattering Methods," *Soviet Phys.-Solid State (Engl. Transl.)*, **27** [3] pp. 455-57 (1985).
18. K. Sakata and Y. Masuda, "Ferroelectric and Antiferroelectric Properties of $(\text{Na}_{1/2}\text{Bi}_{1/2})\text{TiO}_3\text{-SrTiO}_3$ Solid Solution Ceramics," *Ferroelectrics*, **7** pp. 347-51 (1974).
19. A. M. Antonenko, M. G. Gavshin, and A. Y. Kudzin, "Growth of Single Crystals in the Morphotropic Region of Sodium Bismuth Titanate Solid Solutions," *Phys. Solid State*, **39** [8] pp. 1281-83 (1997).
20. A. M. Glazer, "The Classification of Tilted Octahedra in Perovskites," *Acta Cryst.* **B28** [11] pp. 3384-3392 (1972).
21. S. B. Vakhrushev, B. G. Ivanitskii, B. E. Kvyatkovskii, and A. N. Maistrenko, "Neutron Scattering Studies of the Structure of Sodium Bismuth Titanate," *Sov. Phys. Solid State*, **25** [9] pp. 1504-6 (1983).
22. J. Suchanics, R. Poprawski, and S. Matyjasic, "Some Properties of $\text{Na}_{1/2}\text{Bi}_{1/2}\text{TiO}_3$," *Ferroelectrics*, **192** pp. 329-333 (1997).
23. T. Takenaka and H. Nagata, "Present Status of Non-Lead Based Piezoelectric Ceramics," *Key Engineering Materials*, **157-158**, 57-64 (1999).

24. A.N. Soukhojak, H. Wang, G.W. Farrey and Y.-M. Chiang, "Superlattice in Single Crystal Barium-Doped Sodium Bismuth Titanate," *J. Phys. Chem. Solids*, **61** [2] pp.301-304 (2000).
25. S. E. Park and S. J. Chung, "Ferroic Phase Transitions in $(\text{Na}_{1/2}\text{Bi}_{1/2})\text{TiO}_3$ Crystals," *J. Am. Ceram. Soc.*, **79** [5] pp. 1290-96 (1996).
26. S. E. Park and K. S. Hong, "Variation of Structure and Dielectric Properties on Substituting A-site Cations for Sr^{2+} in $(\text{Na}_{1/2}\text{Bi}_{1/2})\text{TiO}_3$," *J. Mater. Res.*, **12** [8] pp. 2152-57 (1997).
27. T. Takenaka, K. Maruyama, and K. Sakata, " $\text{Na}_{1/2}\text{Bi}_{1/2}\text{TiO}_3$ - BaTiO_3 System for Lead-Free Piezoelectric Ceramics," *Jap. J. Appl. Phys.*, **30** [9b], 2236-9 (1991).
28. S. E. Park, private communication.
29. A. Herabut and A. Safari, "Processing and Electromechanical Properties of $(\text{Na}_{1/2}\text{Bi}_{1/2})_{(1-1.5x)}\text{La}_x\text{TiO}_3$ Ceramics," *J. Am. Ceram. Soc.*, **80** [11] pp. 2954-58 (1997).
30. H. Nagata and T. Takenaka, "Additive Effects on Electrical Properties of $(\text{Bi}_{1/2}\text{Na}_{1/2})\text{TiO}_3$ Ferroelectric Ceramics," *J. Eur. Cer. Soc.*, **21** pp. 1299-302 (2001).
31. R. E. Newnham, "Composite Electroceramics," *Ferroelectrics*, **68** pp. 1-32 (1986).
32. X. H. Du, U. Belegundu, and K. Uchino, "Crystal Orientation Dependence of Piezoelectric Properties in Lead Zirconate Titanate: Theoretical Expectations for Thin Films," *Jpn. J. Appl. Phys.*, **36** [9A] pp. 5580-87 (1997).

33. E. M. Sabolsky, Grain-Oriented $\text{Pb}(\text{Mg}_{1/3}\text{Nb}_{2/3})\text{O}_3\text{-PbTiO}_3$ Ceramics Prepared by Templated Grain Growth, Ph.D. Thesis, The Pennsylvania State University, University Park, PA (2001).
34. C. Duran, Fabrication and Electrical Properties of Textured $\text{Sr}_{0.53}\text{Ba}_{0.47}\text{Nb}_2\text{O}_6$ Ceramics Prepared by Templated Grain Growth. Ph.D. Thesis, Penn State University (2001).
35. J. A. Horn, S. C. Zhang, U. Selvaraj, G. L. Messing, and S. Trolier-McKinstry, "Templated Grain Growth of Textured Bismuth Titanate," *J. Am. Ceram. Soc.*, **82** [4] 921-26 (1999).
36. J. A. Horn, S. Trolier-McKinstry and G. L. Messing, "Dielectric and Electromechanical Properties of Textured Niobium-Doped Bismuth Titanate Ceramics," *J. Am. Ceram. Soc.*, **83** [1] pp. 113-18 (2000).
37. S. Swartz, W. A. Schulze, and J. V. Biggers, "Fabrication and Electrical Properties of Grain Oriented $\text{Bi}_4\text{Ti}_3\text{O}_{12}$," *Ferroelectrics*, **38** [10] pp. 765-68 (1981).
38. K. Nagata and K. Okazaki, "One-Dimensional Grain-Oriented Lead Metaniobate Ceramics," *Jap. J. Appl. Phys.*, **24** [7] pp. 812-14 (1985).
39. Y. Ohara, T. Taki, K. Koumoto, and H. Yanagida, "Crystal-axis Oriented Ceramics Prepared from Fibrous Barium Titanate," *J. Mater. Sci. Lett.*, **11** pp. 1327-29 (1992).
40. Y. Ohara, K. Koumoto, and H. Yanagida, "Barium Titanate Ceramics with High Piezoelectricity Fabricated from Fibrous Particles," *J. Am. Ceram. Soc.*, **68** [4] pp. C108-109 (1985).

41. T. Takeuchi, T. Tani, and Y. Saito, "Piezoelectric Properties of Bismuth Layer-Structured Ferroelectric Ceramics with a Preferred Orientation Processed by the Reactive Templated Grain Growth Method," *Jpn. J. Appl. Phys., Part 1*[9B] pp. 5553-56 (1999).
42. E. Fukuchi, T. Kimura, T. Tani, and T. Takeuchi, "Oriented $\text{Bi}_{0.5}(\text{Na},\text{K})_{0.5}\text{TiO}_3$ Ceramics", in *Perovskite Oxides for Electronic, Energy Conversion, and Energy Efficiency Applications*, Edited by W. Wong-Ng, T. Holesinger, G. Riley, and R. Guo, *Ceramic Transactions* vol. 104, Published by The American Ceramic Society, Westerville, OH, 2000.
43. Y. Seno and T. Tani, "TEM Observation of a Reactive Template for Textured $\text{Bi}_{0.5}(\text{Na}_{0.87}\text{K}_{0.13})_{0.5}\text{TiO}_3$ Polycrystals", *Ferroelectrics*, **224** 365-372 (1999).
44. T. Tani, "Crystalline-oriented Piezoelectric Bulk Ceramics with a Perovskite-type Structure", *Journal of the Korean Physical Society*, **32** S1217-S1220 (1998).
45. E. Fukuchi and T. Kimura, "Effect of Potassium Concentration on the Grain Orientation in Bismuth Sodium Potassium Titanate," *J. Am. Ceram. Soc.*, **85** [6] pp. 1461-66 (2002).
46. L. A. Shuvalov, "Dielectric and Piezoelectric Properties of Polarized Ceramic BaTiO_3 in its Various Ferroelectric Phases," *Kristallografiya*, **2** pp. 115-24 (1954).
47. C. W. Nan and D. R. Clarke, "Piezoelectric Moduli of Piezoelectric Ceramics," *J. Am. Ceram. Soc.*, **79** [10] pp. 2563-66 (1996).
48. A. V. Shubnikov, "Piezoelectric Textures," *Izd. Akad. Nauk. SSSR*, (1946).

49. A. V. Shubnikov, I. S. Zheludev, V. P. Konstantinova, and I. M. Silvestrova, "Research on Piezoelectric Textures," *Izd. Akad. Nauk. SSSR*, (1955).
50. R. D. Redin, G. W. Marks, and C. E. Antoniak, "Symmetry Limitations to Polarization of Polycrystalline Ferroelectrics," *J. Appl. Phys.*, **34** [3] pp. 600-10 (1963).
51. T. Olson and M. Avellaneda, "Effective Dielectric and Elastic Constants of Piezoelectric Polycrystals," *J. Appl. Phys.*, **71** [9] pp. 4455-64 (1992).
52. N. A. Pertzev, A. G. Zembilgotov, and R. Waser, "Aggregate Linear Properties of Ferroelectric Ceramics and Polycrystalline Thin Films: Calculation by the Method of Effective Piezoelectric Medium," *J. Appl. Phys.*, **84** [3] pp. 1524-29 (1998).
53. B. Jaffe, W. R. Cook, and H. Jaffe, Piezoelectric Ceramics. Academic Press, New York, 1971.
54. B. Brahmaroutu, G. L. Messing, S. Trolier-McKinstry, and U. Selvaraj, "Templated Grain Growth of Textured $\text{Sr}_2\text{Nb}_2\text{O}_7$," *Proceedings of the Tenth IEEE International Symposium on Applications of Ferroelectrics*, edited by B. Kulwicki, A. Amin, and A. Safari (The Institute of Electrical and Electronic Engineers, Piscataway, NJ, 1996), Vol. 2, pp. 883-86 (1996).
55. B. Brahmaroutu, *Templated Grain Growth of Textured Strontium Niobate Ceramics*, Ph.D. Thesis, The Pennsylvania State University, University Park, PA (1999).
56. M. M. Seabaugh, I. H. Kerscht, and G. L. Messing, "Texture Development by Templated Grain Growth in Liquid-Phase-Sintered α -Alumina," *J. Am. Ceram. Soc.*, **80** [5] 1181-88 (1997).

Chapter 3

(REACTIVE) TEMPLATED GRAIN GROWTH OF TEXTURED SODIUM BISMUTH TITANATE ($\text{Na}_{1/2}\text{Bi}_{1/2}\text{TiO}_3\text{-BaTiO}_3$) CERAMICS

3.1 INTRODUCTION

Sodium bismuth titanate (NBT) is an interesting non-lead based piezoelectric material with a high transition temperature ($T_c \sim 230^\circ\text{C}$) and remanent polarization ($38 \mu\text{C}/\text{cm}^2$) [1]. In the $[001]_{pc}$ direction, a d_{33} coefficient as high as 450 pC/N [2] has been reported for flux grown single crystals at the morphotropic phase boundary with BaTiO_3 (BT), Figure 3.1 [3] (the phase diagram has been redrawn relative to the published one as explained in chapter 2). In contrast, the highest reported piezoelectric coefficient for polycrystalline $(\text{Na}_{1/2}\text{Bi}_{1/2})\text{TiO}_3$ ceramics is 125 pC/N [1]. If the reported single crystal properties can be achieved in a textured ceramic, while simultaneously reducing the level of hysteresis [2], the resulting material might be an alternative for lead-based piezoelectrics like lead zirconate titanate.

Grain oriented $(\text{Na,K})_{1/2}\text{Bi}_{1/2}\text{TiO}_3$ (NKBT) ceramics were prepared by Tani's group by the reactive templated grain growth method using $\text{Bi}_4\text{Ti}_3\text{O}_{12}$ templates [4-6]. Plate-like $\text{Bi}_4\text{Ti}_3\text{O}_{12}$ particles were aligned parallel to the tape casting direction to act as templates for oriented growth of NKBT. A Lotgering factor of 92% was achieved and improvements in the electrical properties like dielectric constant (9% increase to 644), planar coupling coefficient (46% increase to 0.43), piezoelectric coefficient d_{31} (71% increase to -63 pC/N) were attributed to the increased crystallographic orientation [4-6].

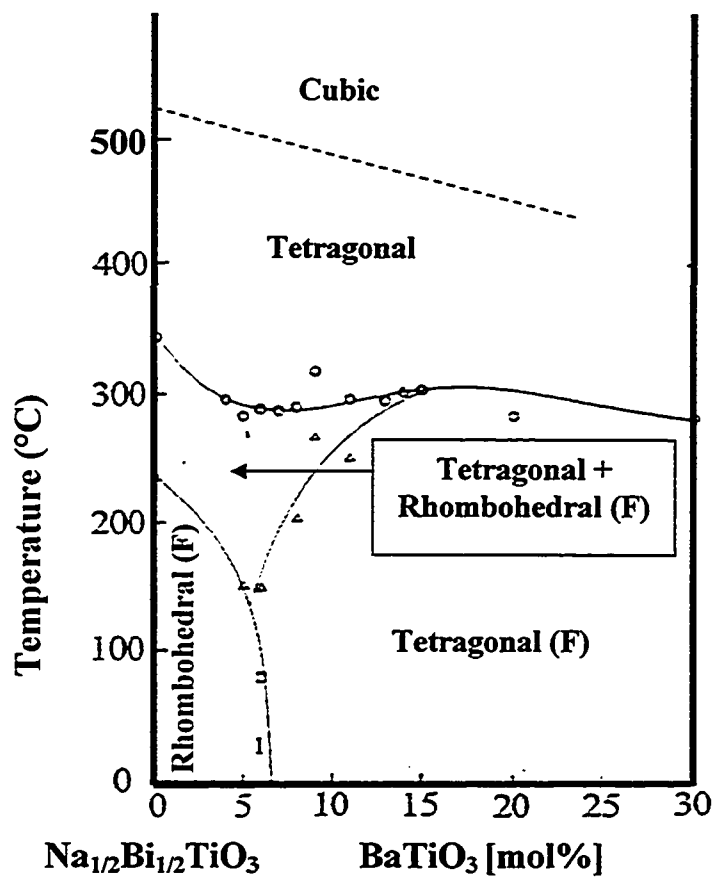


Figure 3.1. Modified phase diagram of $\text{Na}_{1/2}\text{Bi}_{1/2}\text{TiO}_3$ - BaTiO_3 system [3].
(F=Ferroelectric).

The best candidate template for seeding (and also for texturing) NBT would, of course, be NBT templates. However, anisotropically-shaped NBT templates are not available. Alternative candidates include single crystals of other perovskites, which have the same crystal structure and a lattice parameter similar to NBT-BT.

Preliminary experiments showed that BaTiO_3 was unstable in a matrix of NBT, whereas SrTiO_3 was able to template growth of oriented NBT. The objective of this study was to texture $\text{Na}_{1/2}\text{Bi}_{1/2}\text{TiO}_3$ -5.5mol% BaTiO_3 (NBT-5.5 mol% BT) solid solutions by either templated grain growth (TGG) using SrTiO_3 (ST) templates or reactive templated grain growth using $\text{Bi}_4\text{Ti}_3\text{O}_{12}$ (BIT) templates. The composition close to the morphotropic phase boundary (~5.5 mol% BT) was specifically chosen because the electromechanical properties are reported to be the best at this composition. In chapter 4 the piezoelectric and dielectric properties of textured NBT-BT are correlated to the texture quality and compared to those of single crystals.

3.2 EXPERIMENTAL PROCEDURE

3.2.1 TEMPLATE SYNTHESIS

SrTiO_3 platelets were synthesized by a two step process [7]; in the first reaction, fumed TiO_2 (P25, Degussa-Huls, Frankfurt-Main, Germany) and SrCO_3 (Alfa Aesar 99% (1% Ba), Ward Hill, MA, USA) powders were reacted in a KCl (Alfa Aesar, Ward Hill, MA, USA) flux at 1300°C for 4 hours to obtain $\text{Sr}_3\text{Ti}_2\text{O}_7$ platelets. In the second reaction, $\text{Sr}_3\text{Ti}_2\text{O}_7$ platelets were reacted with TiO_2 at 1200°C for 4 hours in a KCl flux to obtain SrTiO_3 platelets with {100} major faces. Both reactions were in sealed alumina crucible. The reactions yield anisometric SrTiO_3 particles, (see Figure 3.2). Residual KCl was

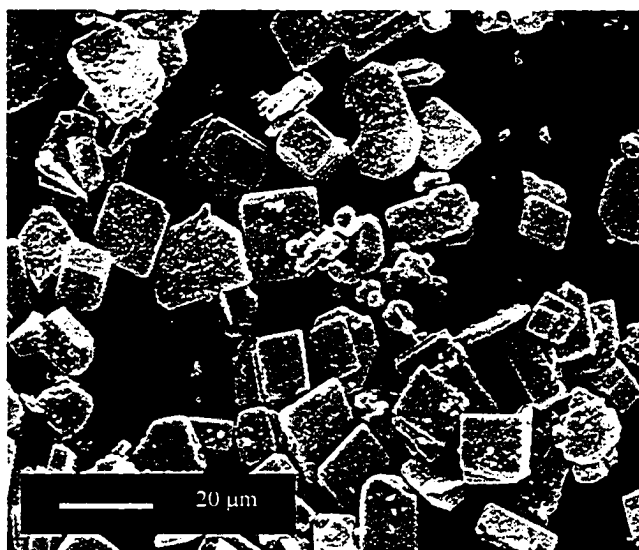


Figure 3.2. SEM image of molten salt synthesized SrTiO₃ particles.

removed from the platelets by repeated washing in deionized water. SrTiO₃ platelets having an edge length of 10-20 μm and a thickness of 2-5 μm were obtained. The aspect ratio of the particles was 2-10. More details on the template synthesis are given in [7,8].

Plate-like Bi₄Ti₃O₁₂ (BiT) particles were prepared by mixing equal weights of Bi₂O₃ (Alfa Aesar 99.99%, Ward Hill, MA, USA) (79.5 wt%) and TiO₂ (P25, Degussa-Huls, Frankfurt-Main, Germany) (20.5 wt%) powders with a eutectic mixture of NaCl (44 wt%) and KCl (56 wt%) in a sealed alumina crucible and by heating to 1100°C, above the eutectic temperature (645°C) of the salt [9,10]. The mixture was heated at a rate of 10°C/min from RT (room temperature), and held at temperature for 30 mins. before slow cooling. It was then washed with warm deionized water to remove the alkali metals and chlorine. The particles were 5-20 μm in diameter and ~0.5 μm in thickness (Figure 3.3).

3.2.2 SAMPLE PREPARATION

For TGG, chemically pure Na₂CO₃ (J.T. Baker Chemical Co, NJ, USA), Bi₂O₃ (Alfa Aesar 99.99%, Ward Hill, MA, USA), TiO₂ (P25, Degussa-Huls, Frankfurt-Main, Germany), BaCO₃ (J.T. Baker Chemical Co 99.9%, NJ, USA) and MnCO₃ (0.3 wt%, Alfa Aesar 99.9%, Ward Hill, MA, USA) powders, corresponding to the (Na_{1/2}Bi_{1/2})_{0.945}Ba_{0.055}TiO₃ stoichiometry, were ball milled in isopropanol with 3 mm ZrO₂ balls in a Nalgene bottle for 16 hours. Mn additions have been found to enhance the electrical resistivity and grain growth and to lower coercive field [11]. The mixture was calcined at 800°C for 2 hours and then ball milled in isopropanol with 3 mm ZrO₂ balls in

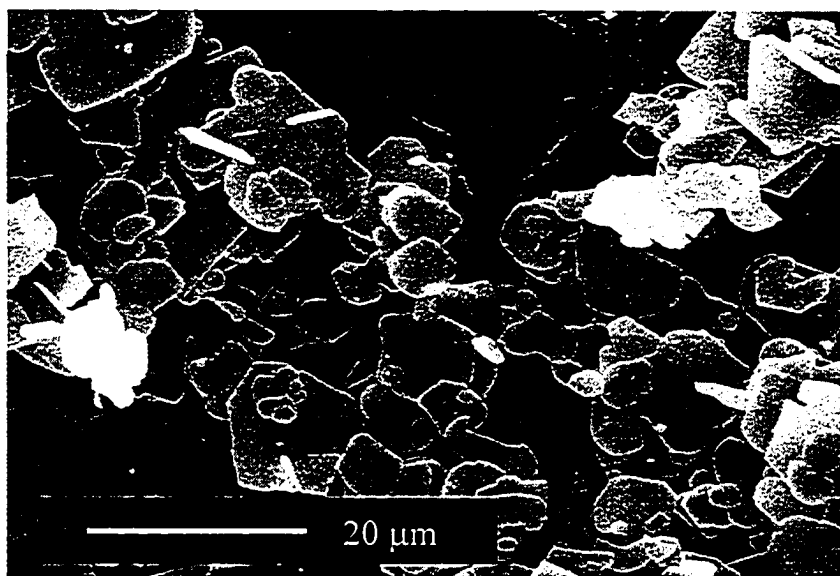


Figure 3.3. SEM image of molten salt synthesized Bi₄Ti₃O₁₂ platelets.

Nalgene bottles for 16 hours. The resulting milled powder was mixed with a commercial binder system (Ferro 73210, Ferro Corp., Cleveland, OH) in toluene (J.T. Baker Chemical Co, NJ, USA) for tape casting. SrTiO_3 ($\rho_{\text{NBT}} \approx 5.116 \text{ g/cm}^3$) platelets, corresponding to 5 vol% of the $(\text{Na}_{1/2}\text{Bi}_{1/2})_{0.945}\text{Ba}_{0.055}\text{TiO}_3$ ($\rho_{\text{NBT}} \approx 6 \text{ g/cm}^3$) powder, were added to the slurry.

For the RTGG approach, the chemicals mentioned above, i.e. Na_2CO_3 , Bi_2O_3 , TiO_2 , BaCO_3 and MnCO_3 , were ball milled in isopropanol with 3 mm ZrO_2 balls in Nalgene bottles for 16 hours. Extra Na_2CO_3 and Bi_2O_3 were added to the mixture to account for the deficiency in the $\text{Bi}_4\text{Ti}_3\text{O}_{12}$ templates. The resulting milled powder mixture was mixed with a commercial binder system (Ferro 73305, Ferro Corp., Cleveland, OH) in toluene for tape casting. $\text{Bi}_4\text{Ti}_3\text{O}_{12}$ platelets corresponding to 6 vol% of the $(\text{Na}_{1/2}\text{Bi}_{1/2})_{0.945}\text{Ba}_{0.055}\text{TiO}_3$ powder were added to the slurry.

In both approaches, the slurry was cast with a doctor blade on a glass substrate with a blade opening of 200 μm at a shear rate of $\sim 200 \text{ s}^{-1}$. The viscosity of the slurry was 150 mPa.s. The dried tapes were cut into 1.5 cm by 2.5 cm pieces and 60 tapes were laminated at 80 MPa. The binder was burned out by heating at 600°C for 1 hour with heating and cooling rates of 0.86 °C/min. For TGG, the samples were heated in O_2 at 10 °C/min to 1200°C and held for up to 12 hours. For RTGG, the sample was reacted between 600°C and 1000°C for up to 4 hours before sintering at 1200°C. Samples were sintered on a Pt foil in an alumina crucible.

SEM images of the samples were taken after etching at 1050°C for 30 minutes. The surfaces of the etched samples were cleaned in an ultrasonic bath and then gently rubbed with Q-tips.

The Lotgering factor, rocking curves and x-ray pole figures were used to quantify texture. The Lotgering factor [12] is a semi-quantitative method and does not give any information about the grain orientation distribution. Crystallographic texture was characterized using X-ray based rocking curves [13] in order to obtain quantitative information about the grain orientation distribution. Rocking curve measurements were performed around the (002) peak (i.e. 2 theta: 46.6°) of NBT with a rocking curve in ω of -20° to +20° θ using a standard X-ray diffractometer (Scintag, Inc., CA, PAD V, theta-2-theta goniometer, Si(Li) Peltier detector). The data were corrected to eliminate defocusing and absorption effects using a computer program developed by Vaudin [14]. The March-Dollase function, Eqn. 3.1, was used to quantify the texture distributions from the rocking curve analysis [15]. $F(f,r,\omega)$, the texture compensation factor, is given by

$$F(f,r,\omega) = f \left(r^2 \cos^2 \omega + \frac{\sin^2 \omega}{r} \right)^{-\frac{3}{2}} + (1-f) \quad \text{Eqn. 3.1}$$

where ω is the angle between the texture (orientation) axis and the scattering vector, r is the degree of orientation, and f is the volume fraction of oriented material. The r parameter characterizes the width of the texture (orientation) distribution. $r=1$ for a random sample and for a perfectly textured sample of tabular grains $r=0$.

Pole figures were measured using a four-circle diffractometer and $\text{CuK}\alpha$ radiation. Pole figures were measured in steps of $\Delta\alpha=5^\circ$ and $\Delta\beta=5^\circ$ in the ranges of

$0^\circ \leq \alpha \leq 70^\circ$ and $0^\circ \leq \beta \leq 360^\circ$, with a measuring time of 10 seconds/point, where α is the tilt angle and β is the azimuthal angle.

3.3 RESULTS AND DISCUSSION

3.3.1 TEMPLATED GRAIN GROWTH OF $\text{Na}_{1/2}\text{Bi}_{1/2}\text{TiO}_3$ CERAMICS USING SrTiO_3 TEMPLATE PARTICLES

Figure 3.4 shows that $\langle 001 \rangle_{\text{pc}}$ oriented NBT grows on a $\langle 001 \rangle_{\text{pc}}$ oriented SrTiO_3 single crystal at 1200°C . After 6 hrs at 1200°C , there was $\sim 20 \mu\text{m}$ of epitaxial NBT grown on the surface of SrTiO_3 single crystal. Thus, SrTiO_3 template particles are expected to be stable enough for the TGG of textured NBT ceramics. BaTiO_3 single crystals were also embedded into NBT powder matrix and sintered at the same conditions as explained above. BaTiO_3 single crystals, however, did not survive and dissolved in the matrix. Therefore, BaTiO_3 template particles to texture NBT ceramics were not studied further.

For TGG of textured NBT, 5 vol% molten salt synthesized SrTiO_3 templates were added to the NBT matrix, which gave strong $\langle 001 \rangle_{\text{pc}}$ texture. Sakata and Masuda [16] determined the phase diagram of the NBT- SrTiO_3 system in the composition range of $0 \leq x \leq 0.5$, where x denotes the mole fraction of SrTiO_3 . They found that NBT and SrTiO_3 form solid solutions over this composition range. Therefore, the interaction of SrTiO_3 templates with the NBT matrix was studied with an electron microprobe. The Sr content in the NBT matrix $6 \mu\text{m}$ away from a SrTiO_3 template was determined to be $< 0.3 \text{ wt}\%$. Based on microprobe compositional line scans from the template into the NBT grown

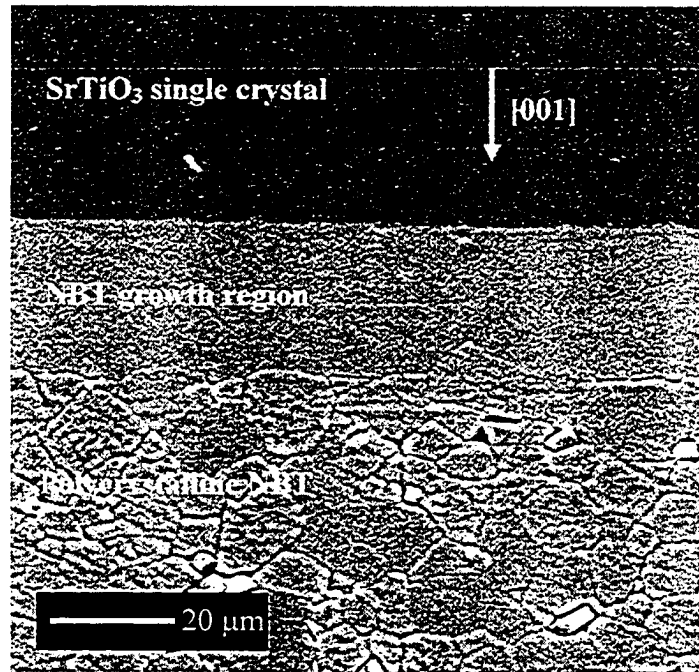


Figure 3.4. Growth of $(\text{Na}_{1/2}\text{Bi}_{1/2})_{0.945}\text{Ba}_{0.055}\text{TiO}_3$ crystal on single crystal SrTiO_3 at 1200°C .

region, the Sr content in the NBT matrix is constant and < 0.3 wt% (0.7 mol%). Since there is no Sr compositional gradient in the NBT growth region, it can be inferred that there is little Sr diffusion into the matrix from SrTiO₃ template. This is useful, since Sr is known to decrease the T_{\max} (-5.3 °C/mol%) of NBT [17].

3.3.2 SINTERING AND MICROSTRUCTURE

The microstructure of a NBT-5.5 mol% BT ceramic templated with 5 vol% SrTiO₃ sintered at 1200°C for 12 hrs. is shown in Figure 3.5. The SrTiO₃ templates can be easily distinguished from the NBT matrix, i.e. SrTiO₃ templates are darker than the NBT matrix phase. All SEM images were taken in the tape casting direction, i.e. perpendicular to the sample normal. There is an NBT growth region on the templates. It appears that the amount of growth of the NBT on each surface of the SrTiO₃ templates is equal. This is reasonable because all of the SrTiO₃ templates are largely bounded by {100} faces [7].

The weight loss in the samples was less than 1.4 % at 1200°C for all sintering times. It is very likely that weight loss is associated with the volatility of Bi and/or Na oxides. Up to 6 % weight loss has been observed for the samples sintered at 1250°C for 8 hrs. For NBT the incongruent melting temperature is around 1240°C [18]. To minimize this problem, in this study the sintering temperature did not exceed 1200°C. The volatility of *pure* Bi₂O₃ and Na₂O is 0.98 Pa and 1650 Pa at 1200°C, respectively [19-20]. These vapor pressure values are not valid for NBT-BT solid solutions, but it should be kept in

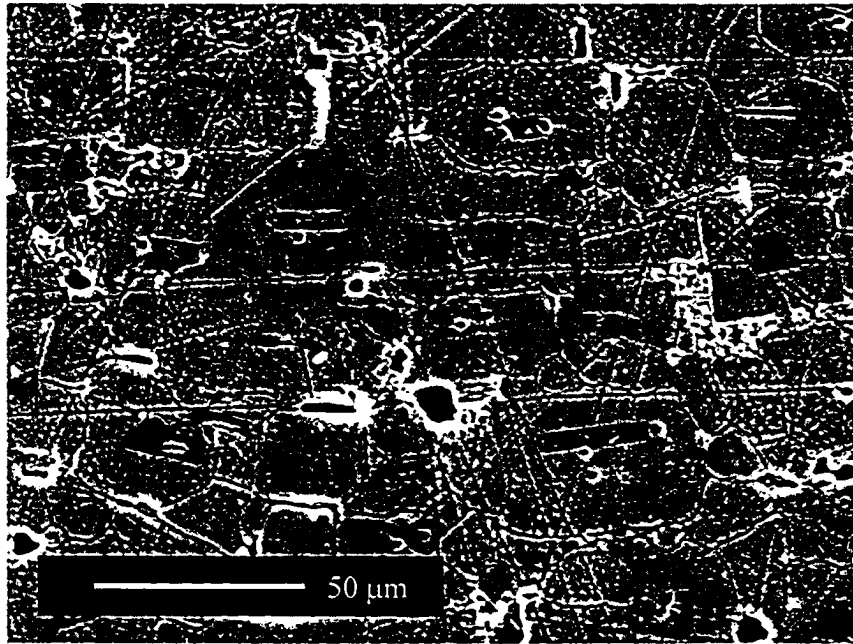


Figure 3.5. SEM microstructure of NBT-5.5 %BT ceramic sintered at 1200°C for 12 hrs. Dark regions are SrTiO₃ templates whereas the light regions are the matrix material.

mind that these two elements have high vapor pressures that might change the stoichiometry of the ceramic. This may have important consequences on the concentration of point defects present in the textured samples, since better texturing was achieved for longer hold times, where volatility may increase.

In Figure 3.6, the texture fraction, as calculated from the Lotgering factor, is plotted as a function of sintering time. It can be seen that $f=70\%$ after only one hour at 1200°C . The Lotgering factor increases slowly with longer sintering times. It takes about 12 hrs. to reach a texture fraction of $f=94\%$. The density of these samples is 5.9 g/cm^3 ($\sim 98\%$ of the theoretical density). Random ceramics sintered at the identical conditions with no SrTiO_3 templates were transparent (fully dense).

The evolution of texture as indicated by Figure 3.6 can be explained as follows. Textured microstructures evolve by dissolution of randomly oriented matrix particles and precipitation on the oriented template particles. The driving force for grain growth comes from the size difference between the template particles and matrix particle, similar to Ostwald ripening. In the initial stage of sintering, the driving force is large and rapid grain growth takes place on the SrTiO_3 templates at the expense of small matrix particles. Therefore, $f=70\%$ texture was obtained for 1 hr of sintering at 1200°C . Coarsening of matrix particles also takes place during templated growth. As a result, the driving force for the relatively large, randomly oriented, matrix particle to dissolve and precipitate on the template particle decreases. The slowing down of the texture development at longer sintering times can be explained by considering the size dependency of solubility, Eqn. 3.2. The solubility of a particle is size dependent [21] and is given by

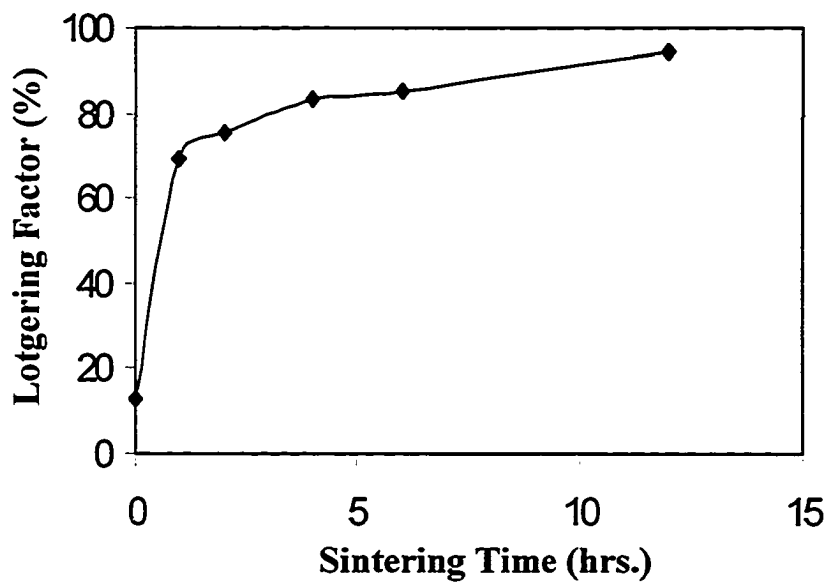


Figure 3.6. Texture evolution as function of sintering time at 1200°C, 5 vol% SrTiO₃ templated NBT-5.5 mol% BT samples.

$$c_R = c_0 \exp\left(\frac{2\gamma\Omega}{RT_r}\right) \quad \text{Eqn. 3.2}$$

where R is the gas constant, T is the temperature, c_0 is the saturation solubility, c_R is the solubility at the surface of a particle with radius r , Ω is the molar volume of the solid, and γ is the surface energy of the solid-liquid interface.

Another reason for the slowing down of the texture development is grain “impingement”, as indicated by arrows in Figure 3.7. Although SrTiO_3 templates were well dispersed in the NBT matrix powder, early grain impingement takes place between templates that are closer to each other. Further growth of these grains at the contact point is not expected, i.e. these grains are at about the same size and grain boundary is flat. Therefore, there is significantly less driving force for the grain boundary to move. As a result, the randomly oriented grains will affect the overall macroscopic physical response of the textured ceramic. The properties are expected to be maximum when all the grains are oriented in the same direction ($\langle 001 \rangle_{pc}$).

In Figure 3.8, the XRD patterns of random and textured NBT-5.5 mol% BT ceramics after sintering at 1200°C for 12 hrs are shown. In a randomly oriented ceramic $\{110\}$ is the main peak. In contrast, the $\{200\}$ peak is the most intense one in the SrTiO_3 templated ceramic. A texture fraction of 94% was measured using the Lotgering factor.

The rocking curve of the sample with a 5 vol% SrTiO_3 template concentration and heated at 1200°C for 12 h is shown in Figure 3.9. The March-Dollase [15] equation was used to model texture and is plotted in the same figure. The texture fraction f was determined to be 80% with an orientation parameter of $r=0.23$. The March-Dollase

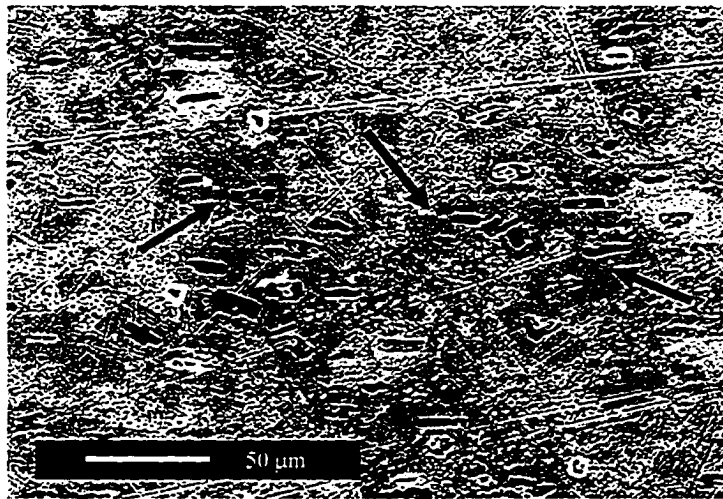


Figure 3.7. SEM image of intermediate stage of sintering of SrTiO₃ templated NBT-5.5 mol% BT ceramics. Arrows mark impingement.

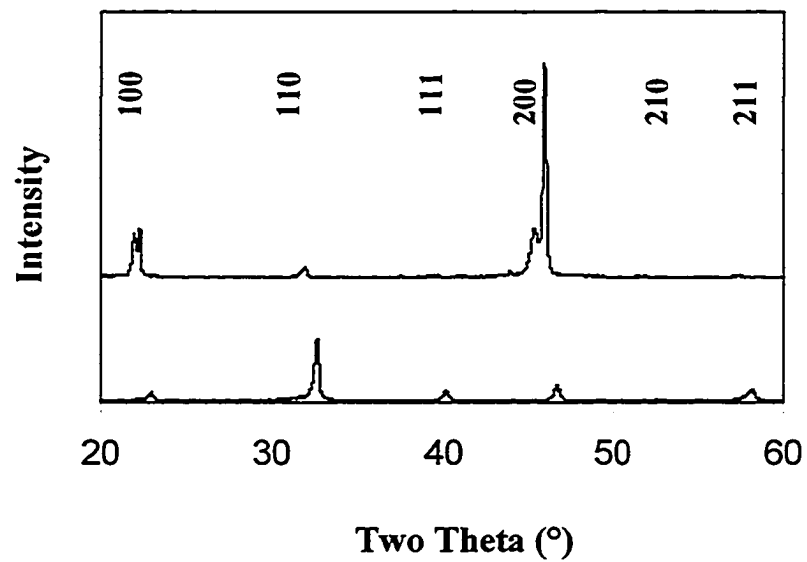


Figure 3.8. XRD pattern of textured $(\text{Na}_{1/2}\text{Bi}_{1/2})_{0.945}\text{Ba}_{0.055}\text{TiO}_3$ ceramic using 5 vol% SrTiO_3 templates sintered at 1200°C for 12 hours (top), and powder of same chemical composition (bottom).

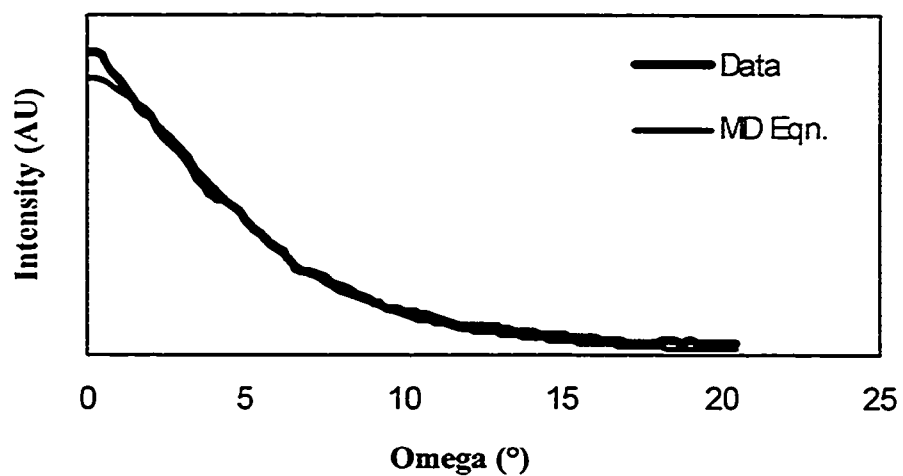


Figure 3.9. Rocking curve of textured $(\text{Na}_{1/2}\text{Bi}_{1/2})_{0.945}\text{Ba}_{0.055}\text{TiO}_3$ ceramic using 5 vol% SrTiO_3 template sintered at 1200°C for 12 hours (MD Eqn.=March-Dollase equation).

equation deviates from the experimental intensity at small rocking angles, so the texture fraction in the sample may be underestimated by about 2-3%. The width of the distribution was narrow, with a Full Width at Half Maximum (FWHM) of 8°. Furthermore, the FWHM was the same in perpendicular directions to the sample normal, confirming fiber texture in the sample, that is, there is no improvement in template alignment parallel and perpendicular to the casting direction within the plane of the tape.

Pole figures of the (002)_{pc} and (111)_{pc} planes are shown in Figure 3.10. Both (002)_{pc} and (111)_{pc} pole figures are axisymmetric, i.e. the sample is fiber-textured and there is no in-plane preferential orientation. For the (111)_{pc} pole figure, the intensity is a maximum at about 53° from the sample normal, which is very close to the angle between [001]_{pc} and [111]_{pc}.

3.3.3 REACTIVE TEMPLATED GRAIN GROWTH USING Bi₄Ti₃O₁₂ TEMPLATE PARTICLES

NBT-BT ceramics were also textured using Bi₄Ti₃O₁₂ platelets using the RTGG approach. The synthesized BiT platelets are single crystals (monoclinic at room temperature) with the *c*-axis perpendicular to the major surface, Figure 3.3. Six vol% anisotropically shaped Bi₄Ti₃O₁₂ platelets were aligned by tape casting in a reactive matrix powder. The prepared samples were either directly heated to sintering temperature or pre-reacted at 700°C or 800°C for 1 hr. before heating to the sintering temperature. These samples were also sintered at 1200°C for 12 hrs.

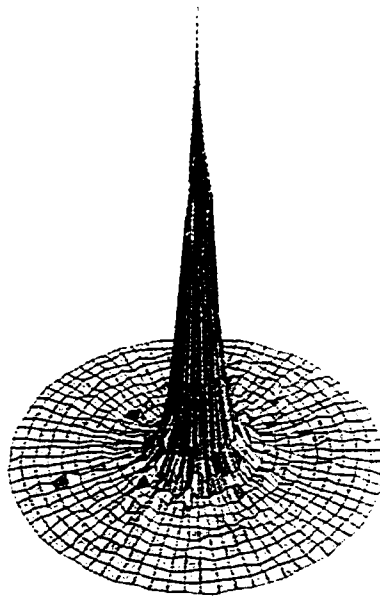


Figure 3.10. (a) XRD-pole figure of (002) planes of textured $(\text{Na}_{1/2}\text{Bi}_{1/2})_{0.945}\text{Ba}_{0.055}\text{TiO}_3$ ceramic using 5 vol% SrTiO_3 templates sintered at 1200°C for 12 hours. (Tilt angle= 70° , Azimuthal angle= 360°).

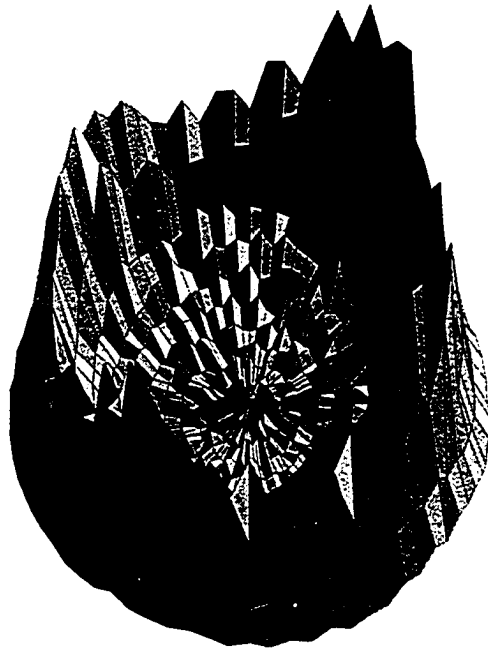


Figure 3.10. (b) XRD-pole figure of (111) planes of textured $(\text{Na}_{1/2}\text{Bi}_{1/2})_{0.945}\text{Ba}_{0.055}\text{TiO}_3$ ceramic using 5 vol% SrTiO_3 templates sintered at 1200°C for 12 hours. (Tilt angle= 70° , Azimuthal angle= 360°).

Pre-reaction at low temperature was found to be a key step in texture development. Samples that were pre-reacted at $\geq 900^\circ\text{C}$, or directly heated to the sintering temperature showed almost no evidence of texturing as measured by a Lotgering factor of $f=8\%$, Figure 3.11. However, if the samples were pre-reacted at 700°C or 800°C , about $f=80\%$ texturing was achieved for both cases. It should be noted that the reproducibility of texture development in the RTGG samples was inferior to the TGG samples

The difference between RTGG and TGG is when the initial reaction occurs at elevated temperature. This reaction has been studied for potassium modified $(\text{Na}_{0.85}\text{K}_{0.15})_{1/2}\text{Bi}_{1/2}\text{TiO}_3$ NBT ceramics which were textured via the RTGG approach by Tani [4-6] using molten salt synthesized $\text{Bi}_4\text{Ti}_3\text{O}_{12}$ template particles. Tani et al. observed *in situ* reactions by transmission electron microscopy (TEM). There was a rapid diffusion of Na and K atoms from the matrix into the BiTi template particles, changing the layered perovskite to a regular perovskite. This *in-situ* reaction of the RTGG processing was regarded as topotactic, in which the template itself changes structure [6]. It is also evident that the single crystallinity of the template particle does not change during this process. This is one of the major differences between the RTGG and TGG processes. In the TGG process, usually heteroepitaxial (because the template used is usually a different phase) growth takes place on the template, as in the case of NBT-5.5 mol% BT ceramics textured using 5 vol% SrTiO_3 templates. These two phases have the same crystal structure and therefore, heteroepitaxial growth takes place on the SrTiO_3 template.

Figure 3.12 shows the microstructure of textured NBT-5.5%BT textured ceramics using $\text{Bi}_4\text{Ti}_3\text{O}_{12}$ templates which were sintered at 1200°C for 12 hours. A grain size up to

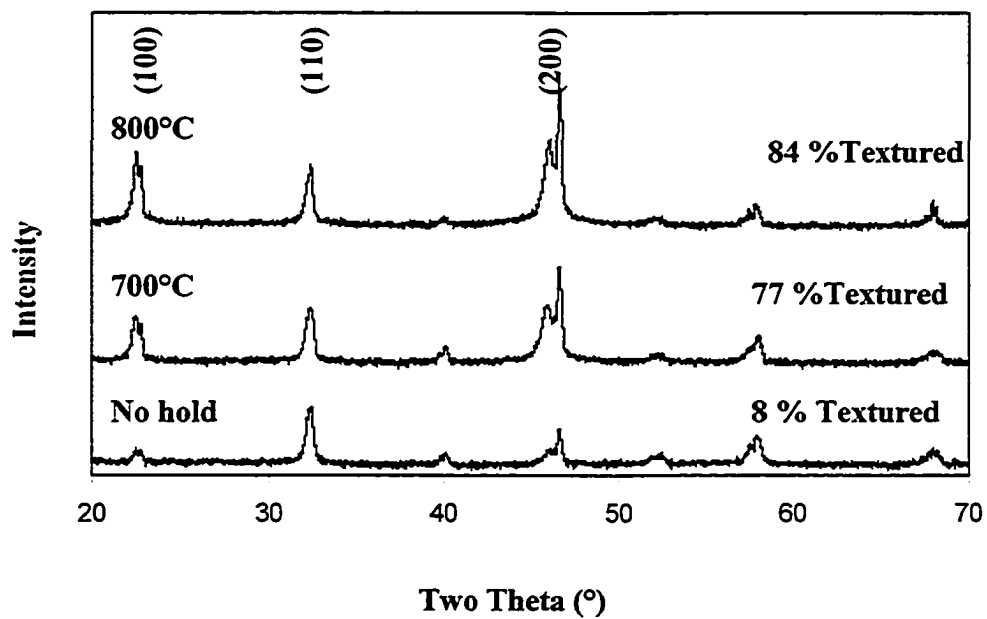


Figure 3.11. XRD patterns of NBT-5.5%BT ceramics textured using $\text{Bi}_4\text{Ti}_3\text{O}_{12}$ templates at different heat treatment conditions.

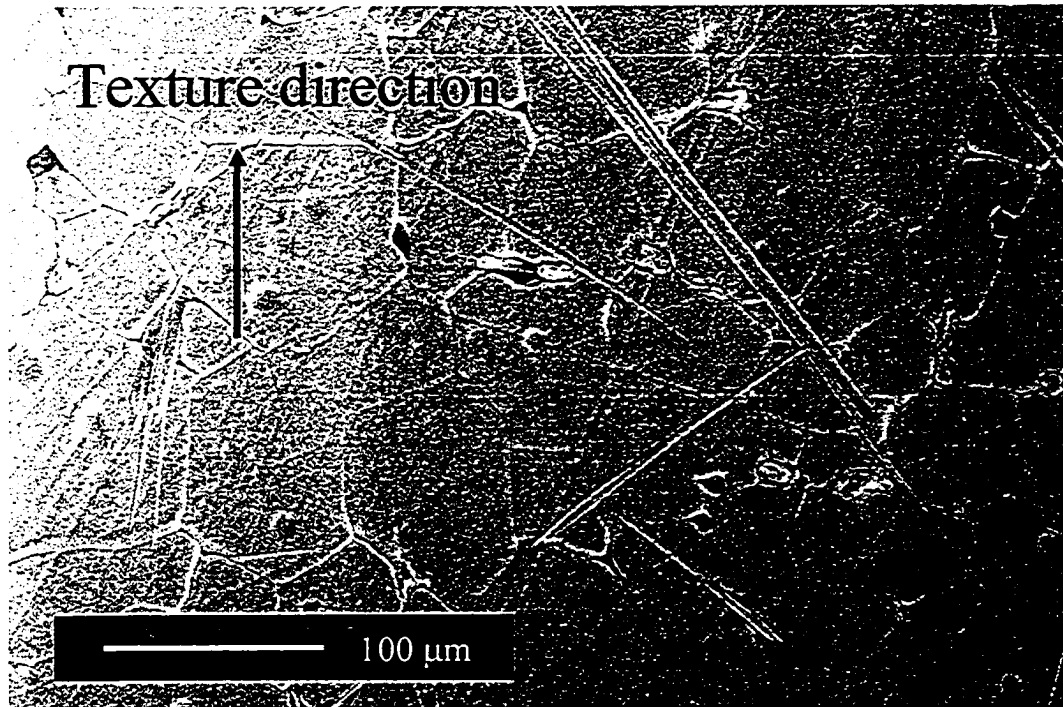


Figure 3.12. SEM image of NBT-5.5%BT ceramics textured using $\text{Bi}_4\text{Ti}_3\text{O}_{12}$ templates after 12 hours at 1200°C , side view.

80 μm was obtained, but there is no evidence of morphological texture in this sample. A brick-wall microstructure was not obtained. In addition, the morphology and grain size were distinctly different than the BiT template size and morphology. Needle like features in the image are a TiO_2 phase [11].

Both TGG and RTGG approaches resulted in $\langle 001 \rangle_{\text{pc}}$ textured NBT-BT ceramics. In the RTGG approach, texture was strongly dependent on the pre-reaction temperature and a texture fraction of up to $f=80\%$ was achieved. The SrTiO_3 templated NBT ceramics resulted in $f=94\%$ texture after sintering at identical sintering conditions.

The two approaches resulted in different microstructures. SrTiO_3 templated ceramics had a narrow grain size distribution ($<50\mu\text{m}$) with a brick wall-like microstructure whereas BiT templated ceramics had a wide grain size distribution (up to 80 μm) and no evidence of morphological texture.

The final grain size can be controlled by the number density of templates. The higher the number density of template particles, the smaller the grain size of the templated grains would be. In this study 5 vol% SrTiO_3 and 6 vol % BiT template particles were aligned in the NBT matrix. Even though the volume of each BiT template particle ($10 \times 10 \times 0.5 \mu\text{m}^3$) was smaller than the volume of SrTiO_3 template particle ($15 \times 15 \times 5 \mu\text{m}^3$) and therefore, there were a larger number (frequency) of BiT template particles per unit volume, the resultant grain size in the ceramic was larger than the grain size in the SrTiO_3 templated samples. This suggests that not all of the BiT template particles act as templates [22]. The reason might be that BiT template particles are $<0.5 \mu\text{m}$ in thickness or that the nucleation did not occur from each template. The size

difference between template particles and matrix powder is relatively small, and therefore the driving force for the template to grow is relatively small. This might also be related to the low reproducibility of texture in the RTGG process.

NBT ceramics were also textured using reactive matrix powder (uncalcined) with SrTiO₃ template particles. Highly textured ceramics (f~90%) have been obtained. The disadvantage of using reactive matrix powder instead of calcined matrix powder is the high amount of sintering shrinkage. Unless there is real benefit from using reactive matrix powder, like template stability, templated grain growth with pre-calcined matrix powder is the most suitable approach. In this study, textured NBT ceramics had similar electrical properties no matter which texturing approach had been used.

3.4 CONCLUSIONS

(Na_{1/2}Bi_{1/2})_{0.945}Ba_{0.055}TiO₃ ceramics were textured by using two kinds of template particles, i.e. SrTiO₃ and Bi₄Ti₃O₁₂ template particles. Growth of sodium bismuth titanate on the strontium titanate template surfaces was heteroepitaxial. A brick wall microstructure resulted after sintering at 1200°C, with a SrTiO₃ template located at the core of each grain. 94% textured NBT-BT ceramics, measured by Lotgering factor, were obtained by using 5 vol% SrTiO₃ template particles. The FWHM of the texture distribution was 8°, measured by rocking curve. Reproducible results were easily obtained with SrTiO₃ templates using the TGG approach.

Reactive templated grain growth of NBT ceramics was performed using Bi₄Ti₃O₁₂ template particles. A texture fraction of 80% was obtained as measured by Lotgering factor. Pre-reaction at 700°C or 800°C before heating the sample to sintering temperature

was critical, because samples directly heated to the sintering temperature did not show any evidence of texturing. During pre-reaction, all the $\text{Bi}_4\text{Ti}_3\text{O}_{12}$ templates were converted to NBT with the perovskite structure [4-6], so no residual $\text{Bi}_4\text{Ti}_3\text{O}_{12}$ phase was expected in the grains.

3.5 REFERENCES

1. T. Takenaka and H. Nagata, "Present Status of Non-Lead Based Piezoelectric Ceramics," *Key Engineering Materials*, **157-158**, 57-64 (1999).
2. Y. M. Chiang, G. W. Farrey, A. N. Soukhovjak, "Lead-Free High-Strain Single-Crystal Piezoelectrics in the Alkaline-Bismuth-Titanate Perovskite Family," *Applied Physics Letters*, **73** 3683-85 (1998).
3. T. Takenaka, K. Maruyama, and K. Sakata, " $\text{Na}_{1/2}\text{Bi}_{1/2}\text{TiO}_3\text{-BaTiO}_3$ System for Lead-Free Piezoelectric Ceramics," *Jap. J. Appl. Phys.*, **30** [9b], 2236-9 (1991).
4. E. Fukuchi, T. Kimura, T. Tani, and T. Takeuchi, "Oriented $\text{Bi}_{0.5}(\text{Na,K})_{0.5}\text{TiO}_3$ Ceramics," in *Perovskite Oxides for Electronic, Energy Conversion, and Energy Efficiency Applications*, Edited by W. Wong-Ng, T. Holesinger, G. Riley, and R. Guo, *Ceramic Transactions vol. 104*, American Ceramic Society, Westerville, OH, 2000.
5. T. Tani, "Crystalline-oriented Piezoelectric Bulk Ceramics with a Perovskite-type Structure," *Journal of the Korean Physical Society*, **32** S1217-S1220 (1998).
6. Y. Seno and T. Tani, "TEM Observation of a Reactive Template for Texture $\text{Bi}_{0.5}(\text{Na}_{0.87}\text{K}_{0.13})_{0.5}\text{TiO}_3$ Polycrystals," *Ferroelectrics*, **224** 365-372 (1999).
7. K. Watari, B. Brahmaroutu, G. L. Messing, S. Trolier-McKinstry and S. C. Cheng, "Epitaxial Growth of Anisotropically Shaped, Single Crystal Particles of Cubic SrTiO_3 ," *J. Mater. Res.*, **15**, 846-849 (2000).
8. K. Watari, G. L. Messing, and S. T. McKinstry, "Preparation of Anisotropic Perovskite Particles," Penn State patent disclosure

9. J. A. Horn, S. C. Zhang, U. Selvaraj, G. L. Messing, and S. Trolier-McKinstry, "Templated Grain Growth of Textured Bismuth Titanate," *J. Am. Ceram. Soc.*, **82** [4] 921-26 (1999).
10. S. H. Hong, S. Trolier-McKinstry, and G. L. Messing, "Dielectric and Electromechanical Properties of Textured Niobium-Doped Bismuth Titanate Ceramics," *J. Am. Ceram. Soc.*, **83** [1] 113-118 (2000).
11. H. Nagata and T. Takenaka, "Additive Effects on Electrical Properties of $(\text{Bi}_{1/2}\text{Na}_{1/2})\text{TiO}_3$ Ferroelectric Ceramics," *J. Eur. Cer. Soc.*, **21** pp. 1299-302 (2001).
12. F. K. Lotgering, "Topotactical Reactions with Ferrimagnetic Oxides Having Hexagonal Crystal Structures-I," *J. Inorg. Nucl. Chem.*, **9**, pp 113, (1959).
13. M. D. Vaudin, M. W. Ruprich, and J. F. Bingert, "A Method for Crystallographic Texture Investigations Using Standard X-ray Equipment," *J. Mater. Res.*, **13** [10] 2910-2919 (1998).
14. M. D. Vaudin, TexturePlus, National Institute of Standards and Technology, Gaithersburg, MD, USA. Available upon request from NIST.
15. W. A. Dollase, "Correction of Intensities for Preferred Orientation in Powder Diffractometry: Application of the March Model," *J. Appl. Crystallogr.*, **19** 267-272 (1986).
16. K. Sakata, and Y. Masuda, "Ferroelectric and Antiferroelectric Properties of $(\text{Na}_{0.5}\text{Bi}_{0.5})\text{TiO}_3\text{-SrTiO}_3$ Solid Solution Ceramics," *Ferroelectrics*, **7** 347-49 (1974).

17. S. E. Park, "Variation of Structure and Dielectric Properties on Substituting A-site Cations for Sr^{2+} in $(\text{Na}_{0.5}\text{Bi}_{0.5})\text{TiO}_3$ ", *J. Mat. Res.*, **12** 2152-57 (1997).
18. S. E. Park, S. J. Chung, I. T. Kim, and K. S. Hong, "Nonstoichiometry and Long-Range Cation Ordering in Crystals of $(\text{Na}_{1/2}\text{Bi}_{1/2})\text{TiO}_3$," *J. Am. Ceram. Soc.*, **77** [10] pp. 2641-47 (1994).
19. L. N. Sidorov, I. I. Minayeva, E. Z. Zasorin, I. D. Sorokin, and A. Ya. Borshchevsky, "Mass Spectrometric Investigation of Gas-Phase Equilibria over Bismuth Trioxide," *High Temp. Sci.*, **12** pp. 175-96 (1980).
20. M. Steinberg and K. Schofield, "A Reevaluation of the Vaporization Behavior of Sodium Oxide and the Bond Strengths of Na_2O : Implications for the Mass Spectrometric Analyses of Alkali/Oxygen Systems," *J. Chem. Phys.*, **94** [5] pp. 3901-07 (1991).
21. Principles of Colloid and Surface Chemistry, P. C. Heimenz, Marcel Dekker, New York, 1986.
22. E. Suvaci, Oxidation Kinetics, Microstructure Evolution and Texture Development in the Reaction-Bonded Aluminum Oxide (RBAO) Process. Ph.D. Thesis, The Pennsylvania State University, 1999.

Chapter 4

ELECTRICAL AND ELECTROMECHANICAL PROPERTIES OF (REACTIVE) TEMPLATED GRAIN GROWTH TEXTURED SODIUM BISMUTH TITANATE (Na_{1/2}Bi_{1/2}TiO₃-BaTiO₃) CERAMICS

4.1 INTRODUCTION

Sodium bismuth titanate-barium titanate, (Na_{1/2}Bi_{1/2})TiO₃-BaTiO₃ (NBT-BT), is a candidate lead-free piezoelectric material which has been shown to have comparatively high piezoelectric response [1]. One means of comparing the performance of piezoelectric materials is the strain energy density [2],

$$e_{\max} = \frac{1}{\rho} \cdot \frac{1}{4} \cdot \left[\frac{1}{2} \cdot E (s_{\max})^2 \right] \quad \text{Eqn. 4.1}$$

where e_{\max} is the maximum strain energy density, E is the actuator's elastic modulus, s_{\max} is the maximum field induced strain, and ρ is the actuator's density. $\frac{1}{4}$ is a factor appropriate for an actuator when its impedance matches its surroundings [2]. Using this metric, NBT-BT has a lower density than PZT and PMN (6 g/cm³ vs. 7.5-8.5 g/cm³) and higher elastic moduli (100-110 GPa vs 60-70 GPa in PZT) [1]. Consequently, rhombohedrally distorted NBT-BT single crystals have been reported to have an actuation energy density 1.4 times greater than of polycrystalline PbMg_{1/3}Nb_{2/3}O₃-PbTiO₃ [2].

Ferroelectric NBT-BT with low BaTiO₃ concentrations has R3c point group symmetry with a small rhombohedral distortion ($90^\circ - \alpha < 0.05^\circ$) at room temperature. The

structure of NBT-BT solid solution becomes tetragonal with increasing BT. The MPB is located at ~6.5 mol% BT [3].

Furthermore, NBT-5.5 mol% BT has a high transition temperature ($T_c \sim 230^\circ\text{C}$) and a large remanent polarization ($38 \mu\text{C}/\text{cm}^2$) [3]. In the $\langle 001 \rangle_{pc}$ direction, a d_{33} coefficient as high as 450 pC/N [1] has been reported for flux grown single crystals at the morphotropic phase boundary with BaTiO_3 [4]. Polycrystalline ceramics on the other hand, have been reported to have d_{33} values of 125 pC/N [3]. If the reported single crystal properties can be achieved in a ceramic, while simultaneously reducing the level of hysteresis [1], the resulting material would be an attractive alternative for lead-based piezoelectrics. One approach to achieving this economically is to texture a polycrystalline sample.

Texture in a polycrystalline sample refers to a preferred orientation distribution of the many crystallites (grains) in the sample with respect to a coordinate system in the sample. Since the individual crystallites (grains) have anisotropic properties, grain orientation and its statistical distribution have an important influence on material properties. This is the motivation for almost all texturing studies [5]. There are three attributes that govern the properties of materials [5]:

- Macroanisotropy due to nonrandom texture.
- Discontinuity of properties across the grain boundaries.
- Grain boundary properties deviating from the bulk properties.

The first factor is mainly influenced by the orientation of the crystallites (texture). The second and third attributes depend on the misorientation across the grain boundaries

and the grain boundary character. For instance, the stresses at the grain boundary are orientation dependent. If these stresses exceed the grain boundary strength then boundary fracture may occur. If the property under consideration is controlled by the grain boundary, as in the case of critical current density in high T_c superconductors, then it is essential to control the grain boundary [5]. The generation of macroanisotropy in NBT-BT ceramics by TGG was the focus of Chapter 3.

The electromechanical properties of single crystal NBT-BT are anisotropic and the electromechanical properties are largest along $\langle 001 \rangle_{pc}$, as is the case for many rhombohedrally distorted perovskites [2]. Therefore, ceramics with grains oriented along $\langle 001 \rangle_{pc}$ should display higher electromechanical properties than randomly oriented ceramics. A composition near the morphotropic phase boundary was specifically chosen because the properties are increased due to higher polarizability.

4.2 EXPERIMENTAL PROCEDURE

NBT-BT ceramics were textured using either SrTiO_3 platelets (TGG approach) or $\text{Bi}_4\text{Ti}_3\text{O}_{12}$ (BiT) platelets (RTGG approach). Both TGG and RTGG approaches resulted in $\langle 001 \rangle_{pc}$ textured NBT-BT ceramics. Details of sample preparation procedures were described in Chapter 3. $\langle 001 \rangle_{pc}$ oriented surfaces were first fine polished using 5000 grit paper and then sputtered with Pt for electrical property measurements. A multi-frequency meter (HP 4284A LCR meter) was used in conjunction with a computer controlled temperature chamber (Delta Design Inc., Model MK 9023) to determine the dielectric constant as a function of temperature on heating and cooling (0°C to 475°C) at

frequencies between 1 kHz and 100 kHz. Samples were heated and cooled at 2°C/min. The samples were poled by applying 60 kV/cm at 100°C for 15 mins. and then cooled to room temperature while maintaining the field.

Simultaneous polarization (P) and strain (S) hysteresis curves were measured as a function of field up to 80 kV/cm on $\langle 001 \rangle_{pc}$ textured ceramics using a computer controlled modified Sawyer Tower system and a linear variable displacement transducer (LVDT) sensor driven by a lock in amplifier (Stanford Research Systems, Model SR830). The electric fields were applied using an amplified triangular wave form at 0.2 Hz, using a Trek 609C-6 high voltage DC amplifier. During testing, the samples were submerged in Fluorinert (FC-40, 3M, St. Paul, MN), an insulating liquid, to prevent arcing. The same system was used to measure unipolar strain curves on poled $\langle 001 \rangle_{pc}$ textured ceramics, with a unipolar wave form. The value of d_{33} was determined from the decreasing slope of the unipolar strain vs. electric field curve between 0 and 10 kV/cm.

In addition, the piezoelectric charge coefficient, d_{33} , of poled samples was measured 24 h after poling, using a Berlincourt d_{33} meter (Model ZJ-2) operating at 100 Hz.

4.3 RESULTS AND DISCUSSION

4.3.1 X-RAY DIFFRACTION ANALYSIS

The rhombohedral distortion close to the MPB was checked with textured samples in order to determine if seeding affected the position of the MPB. Figures 4.1 and 4.2 show the variation of the (111) and (200) peaks with BT doping. Diffraction data were collected at 0.01° steps with a hold of 13 seconds at each step. The XRD-patterns correspond to (bottom to top) SrTiO_3 templates, randomly oriented NBT-5.5 mol% BT, textured NBT-5.5 mol% BT (5 vol% SrTiO_3), and textured NBT-6.5 mol% BT (5 vol% SrTiO_3), respectively.

As it is shown in Figures 4.1 and 4.2, the NBT-BT samples studied here are predominantly rhombohedral in the composition range studied, although the weak broad peaks at lower 2θ angles might indicate a small amount of tetragonal phase. High temperature X-ray diffraction of textured NBT-5.5 mol% BaTiO_3 ceramic was also done, Figure 4.3. The integrated intensity ratio of the (002) and (200) peaks (which is due to the tetragonal splitting) decreases as the temperature is increased. The integrated intensity ratio ($I_{(002)}/I_{(200)}$) of the respective peaks are 0.67 (@ 150°C) and 0.09 (@ 550°C).

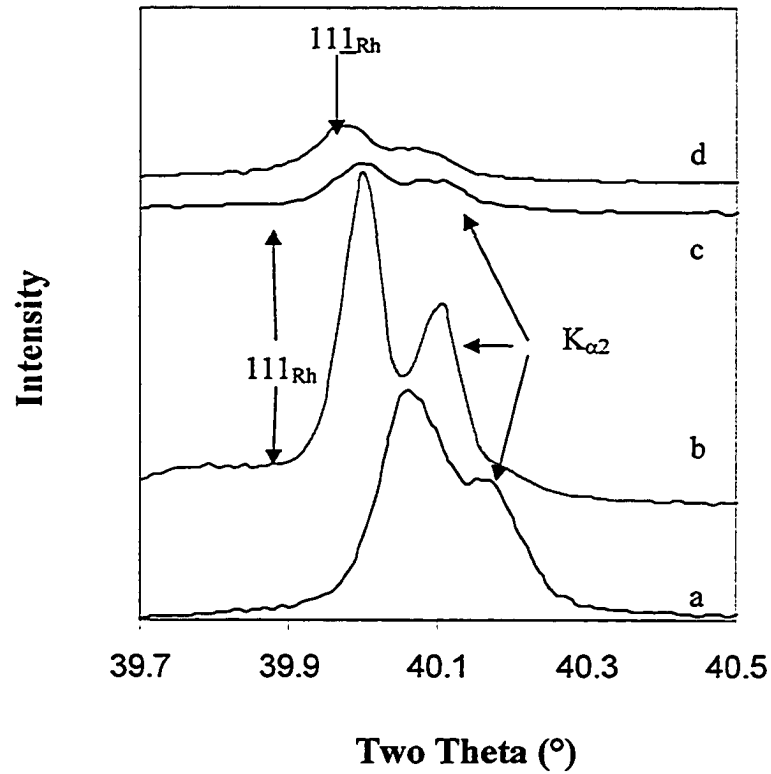


Figure 4.1. (a) (111) x-ray pattern of SrTiO₃ templates, (b) randomly oriented NBT-5.5 mol% BT, (c) textured NBT-5.5 mol% BT, and (d) textured NBT-6.5 mol% BT ceramics (textured ceramics contain 5 vol% SrTiO₃ templates), sintered at 1200°C for 12 hrs.

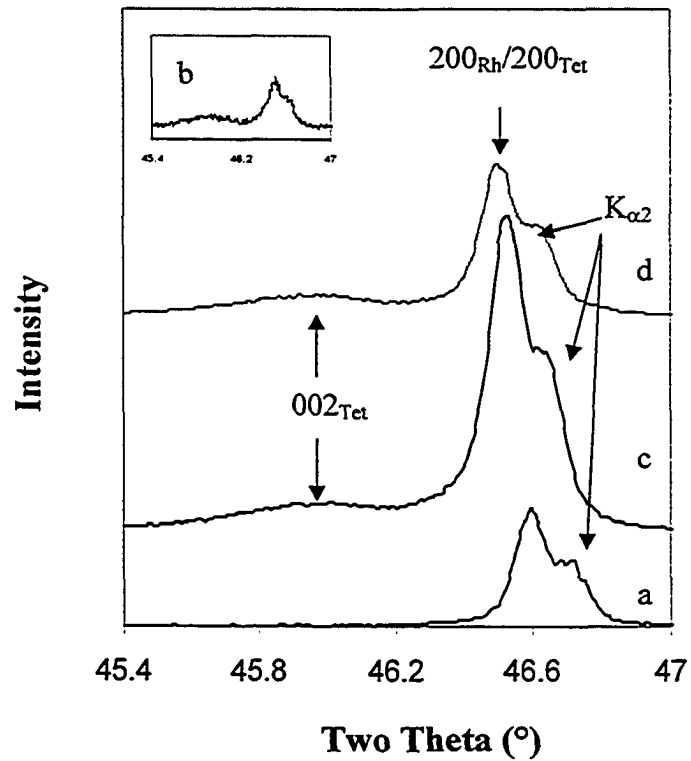


Figure 4.2. (a) (200) x-ray pattern of SrTiO₃ templates, (b) randomly oriented NBT-5.5 mol% BT, (c) textured NBT-5.5 mol% BT, and (d) textured NBT-6.5 mol% BT ceramics (textured ceramics contain 5 vol% SrTiO₃ templates), sintered at 1200°C for 12 hrs.

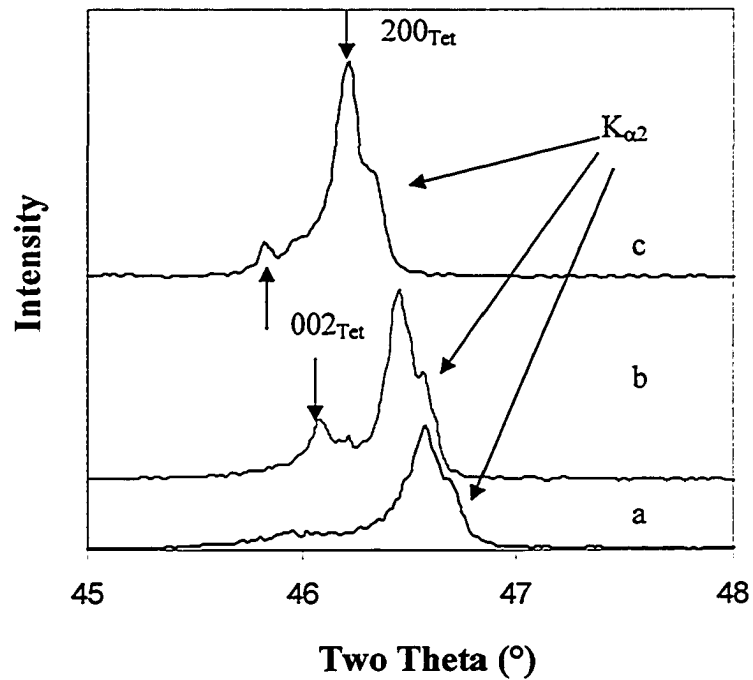


Figure 4.3. (200) x-ray pattern of textured NBT- 5.5 mol% BaTiO₃ ceramics sintered at 1200°C for 12 hrs (a) @ RT, (b) @ 150°C, (c) @ 550°C, (textured ceramics contain 5 vol% SrTiO₃ templates).

4.3.2 HIGH FIELD ELECTRICAL PROPERTIES OF RANDOMLY ORIENTED AND TEXTURED $\text{Na}_{1/2}\text{Bi}_{1/2}\text{TiO}_3\text{-BaTiO}_3$ CERAMICS

4.3.2.1 POLARIZATION

As a reference, randomly oriented NBT-BT ceramics were also characterized. These samples were made without addition of any template particles. The polarization vs. electric field curves for undoped and 5.5 mol% BT doped samples are shown in Figure 4.4. As can be seen the loops are well saturated. The variation of the polarization and the coercive field as a function of BT content for randomly oriented NBT ceramics are shown in Figure 4.5. Samples were sintered at 1200°C for 12 hrs. Undoped NBT has a remanent polarization of 36 $\mu\text{C}/\text{cm}^2$ and a coercive field of 53 kV/cm. The coercive field of undoped NBT is large compared to lead-based ferroelectrics like PZT and PMN-PT ceramics. Coercive fields up to 73 kV/cm have been reported in the literature [3-4]. The poling process is, therefore, difficult. For compositions close to the MPB (5.5 mol% BT), the remanent polarization increases to 45 $\mu\text{C}/\text{cm}^2$ and the coercive field decreases to 34 kV/cm. The remanent polarization and coercive values for 6.5 mol% BT containing sample were 41 $\mu\text{C}/\text{cm}^2$ and 28 kV/cm, respectively. The maximum remanent polarization (45 $\mu\text{C}/\text{cm}^2$) was achieved for 5.5 mol% BT containing samples.

In the same figure, the remanent polarizations and coercive fields for NBT-BT ceramics textured using 5 vol% SrTiO_3 template particles were also plotted as a function of BT content. The remanent polarization values were lower than random ceramics for the same level of BT doping. These results can be explained by crystal symmetry and the presence of a non-ferroelectric phase that does not contribute to the polarization.

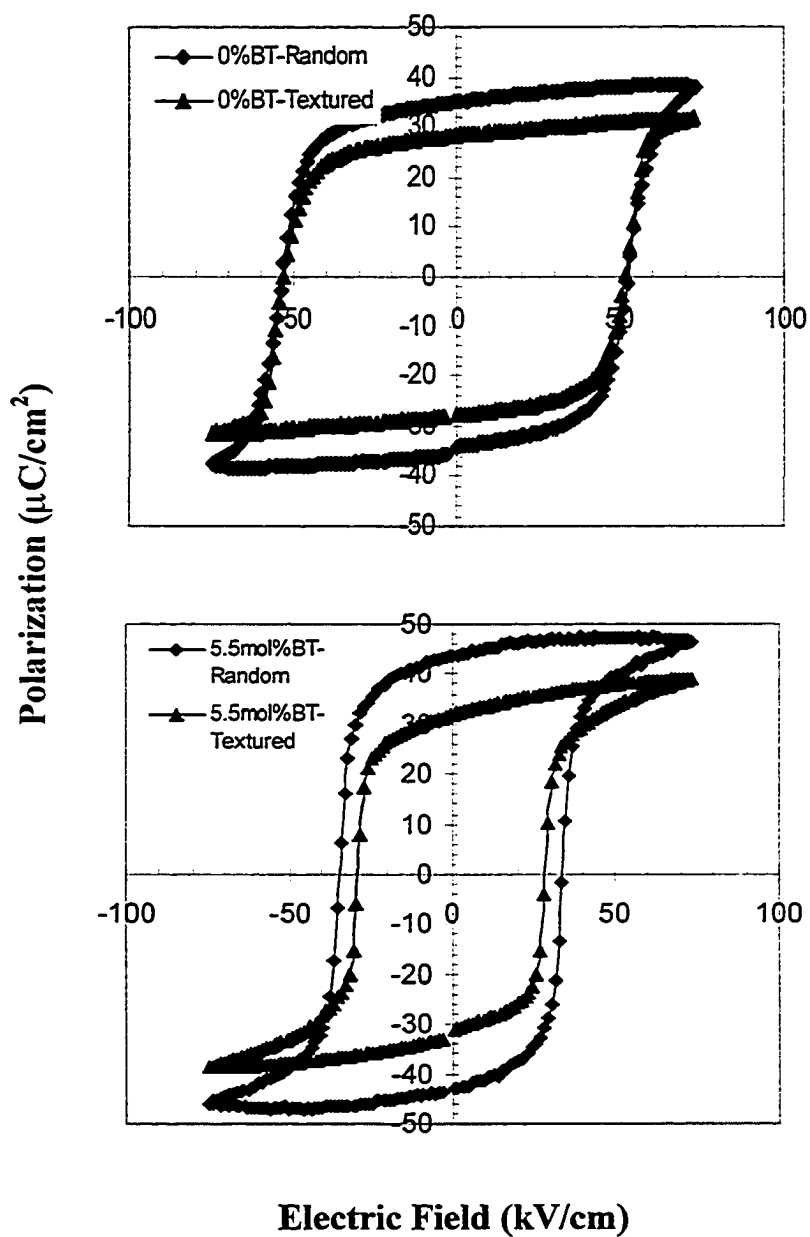


Figure 4.4. Polarization vs. electric field curves of randomly oriented and textured (5 vol % SrTiO_3) NBT-BT ceramics. All samples were sintered at 1200°C for 12 hrs.

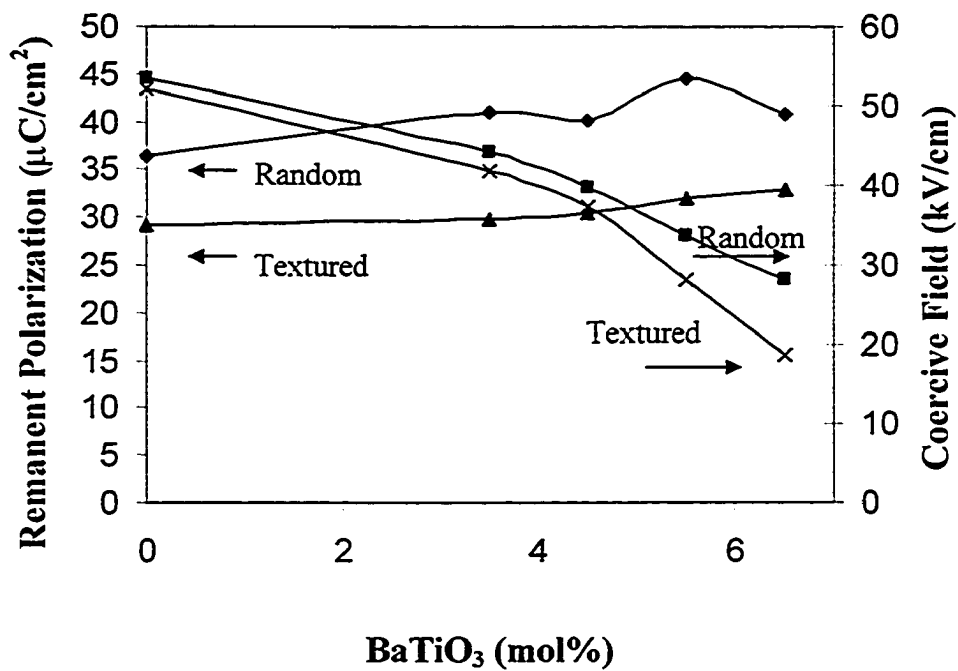


Figure 4.5. Polarizations and coercive fields of randomly oriented and textured (5 vol % SrTiO₃) NBT ceramics plotted as a function of % BT doping. All samples were sintered at 1200°C for 12 hrs.

The remanent polarization of an $\langle 001 \rangle_{pc}$ oriented rhombohedral single crystal must be $1/\sqrt{3} P_s$. Furthermore, in randomly oriented ceramics, $\langle 111 \rangle_{pc}$ is randomly distributed in 3-D space. The angle between the measurement direction and the polarization direction ($\langle 111 \rangle_{pc}$) varies from 0 to 54.7° , with equal pole density in between. However, for textured ceramics, the angle between the measurement direction (texture direction) and polarization direction ($\langle 111 \rangle_{pc}$) is about 54.7° [6], similar to the $\langle 001 \rangle_{pc}$ oriented rhombohedral single crystal case. Therefore, due to the averaging of the polarization of each domain in 3-D space, randomly oriented ceramics have higher P_r than $\langle 001 \rangle_{pc}$ textured materials.

In textured ceramics, there were 5 vol % SrTiO_3 templates which mostly persist due to the modest interdiffusion at the sintering temperature. These templates were aligned in and surrounded by NBT-BT matrix phase. Since SrTiO_3 is a non-ferroelectric phase, its contribution to the polarization was negligible. Thus the remanent polarizations of the textured NBT-BT ceramics were also lowered by the smaller value of polarizable volume. It is also possible that the dielectric and elastic mismatch between the seed and the matrix reduces the efficiency of polarization reversal.

The coercive fields of randomly oriented and textured NBT-BT ceramics using 5 vol% SrTiO_3 template particles are shown in Figure 4.5. Undoped NBT ceramics (random or textured) have similar coercive fields (~ 52 kV/cm), whereas at compositions close to the MPB, textured ceramics have appreciably lower coercive fields than randomly oriented ceramics. The coercive field of randomly oriented NBT-5.5 mol% BT ceramics was 34 kV/cm, whereas it was 28 kV/cm for textured ceramics with the same

level of BT doping. The difference between coercive fields of randomly oriented and textured ceramic with 6.5 mol% BT doping level was ~10 kV/cm.

In Figure 4.6, the remanent polarization of a textured NBT-5.5 mol % BT ceramic is plotted as a function of Lotgering factor (texture fraction). Different levels of texture fraction were obtained by keeping the sintering temperature fixed at 1200°C and varying the sintering times from 1 min. to 12 hrs. Samples sintered less than 1 hr were discarded due to lower density. Densities were greater than 90% (up to 98%) for the samples sintered longer than 1 hr. with varying texture fractions. Since those samples have comparable densities, polarization values were more or less determined by texture fraction only. It was observed that sintering for 1 hr. resulted in a polarization value of 33 $\mu\text{C}/\text{cm}^2$ with a Lotgering factor of $f=69\%$. This polarization value is lower than that of the randomly oriented ceramic (45 $\mu\text{C}/\text{cm}^2$) due to the symmetry of the crystal and the presence of a non-ferroelectric phase, as explained above. Further increases in sintering time resulted in a higher texture fraction and therefore slightly lower polarization values. For example, sintering for 12 hrs. resulted in polarization value of 32 $\mu\text{C}/\text{cm}^2$ with a Lotgering factor of $f=94\%$. It is important to note that these changes are opposite to those expected based on density. That is, the remanent polarization is expected to increase with increasing sample densities. Microprobe analysis had also confirmed that Sr diffusion to the matrix is low, so the decrease of remanent polarization with increasing texture fraction cannot be related only to the Sr diffusion to the matrix. High texture fractions and sintering times were related since high texture fractions were obtained by longer sintering times. If Sr diffusion occurred readily, then there should be more Sr in the

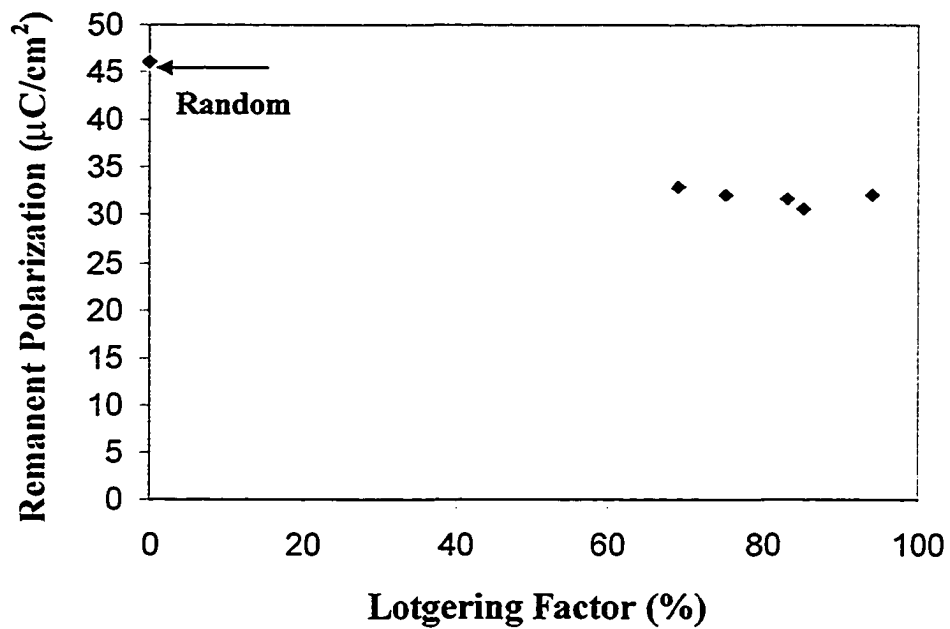


Figure 4.6. Polarization of textured (5 vol % SrTiO_3) NBT-5.5 mol% BT ceramics plotted as function of Lotgering factor. The random ceramics had no SrTiO_3 .

matrix for highly textured samples due to the longer sintering times. However, little Sr diffusion into the matrix was observed in this study by microprobe analysis (0.7 mol% SrTiO₃).

4.3.2.2 ELECTROMECHANICAL PROPERTIES

Figure 4.7 shows the variation of maximum strain of randomly oriented ceramics as a function of % BT doping. Samples were sintered at 1200°C for 12h. The maximum strain is the strain measured when the peak in the electric field (driving field) was reached. Undoped NBT reached 0.06% strain at 50 kV/cm and 0.09% strain at 70 kV/cm. For compositions close to the MPB, higher strains were achieved. Maximum strains of 0.12% at 50 kV/cm and 0.17% at 70 kV/cm were achieved in ceramics containing 5.5 mol% BT. The hysteresis of these samples will be discussed in section 4.3.2.3.

In Figure 4.8 unipolar strain measurement is shown for textured NBT-BT ceramics. Figure 4.9 shows the variation of maximum strain of textured NBT-BT ceramics as a function of % BT doping. 5 vol% SrTiO₃ templates were added, and samples were sintered at 1200°C for 12h. Again, the highest strains were obtained for textured samples close to the MPB. NBT-5.5 mol% BT ceramics reached 0.16% strain at 50 kV/cm and 0.26% strain at 70 kV/cm. This value (0.26% strain) is 62% higher than random ceramics and close to the value reported for single crystals (0.3% strain [1]) of similar composition.

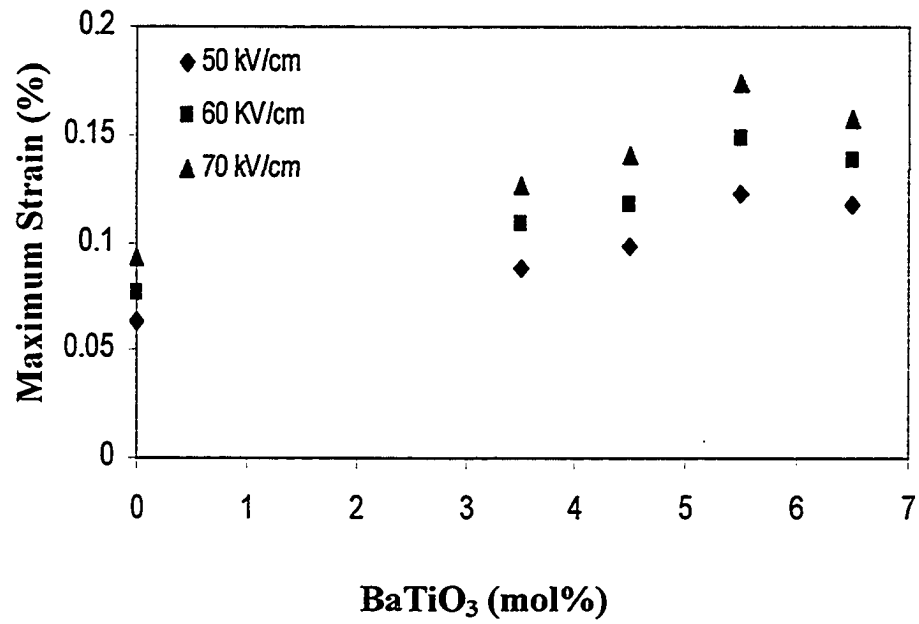


Figure 4.7. Unipolar maximum strain of randomly oriented ceramics plotted as function of % BT doping, sintered at 1200°C for 12 hrs.

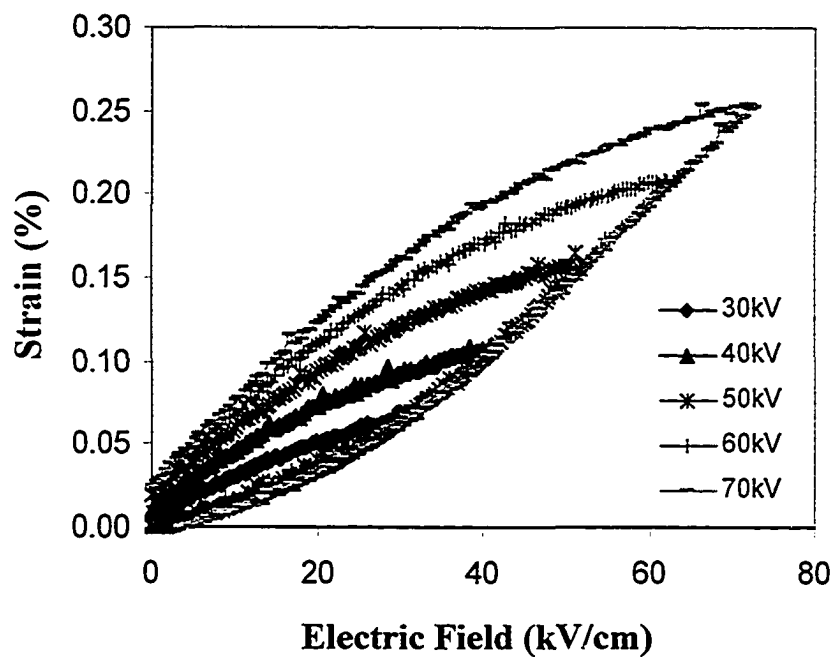


Figure 4.8. Unipolar maximum strain of textured NBT-5.5% BT ceramics textured with 5 vol% SrTiO₃.

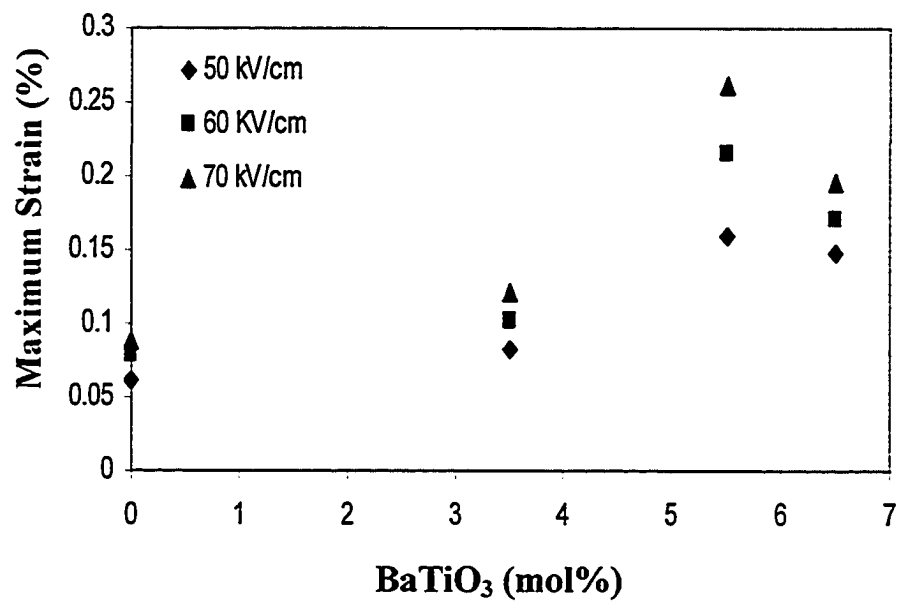


Figure 4.9. Unipolar maximum strain and maximum hysteresis of textured NBT-BT ceramics textured with 5 vol% SrTiO₃ plotted as function of % BT doping.

Figure 4.10 shows the variation of the high field piezoelectric coefficient of randomly oriented ceramic as a function of % BT doping. The piezoelectric coefficient (d_{33}) were estimated from the slope of the unipolar strain vs. electric field E curve. First, a unipolar electric field (driving field) was applied, and then, a linear fit was made to the 0 to 10 kV/cm segment of the decreasing electric field. Driving fields ranged from 30 to 70 kV/cm with 10 kV/cm increments. The d_{33} coefficients of undoped random NBT ceramics ranged showed between 120 (at 30 kV/cm) and 170 (at 70 kV/cm) pC/N. Small driving fields resulted in small piezoelectric coefficients, whereas high driving fields resulted in high piezoelectric coefficients. The highest d_{33} values were obtained for NBT-5.5 mol% BT random ceramics, which showed d_{33} coefficients between 230 (at 30 kV/cm) to 360 (at 70 kV/cm) pC/N.

Figure 4.11 shows the variation of the high field piezoelectric coefficient of textured NBT ceramics (5 vol% SrTiO₃) as a function of % BT doping. Undoped textured NBT ceramics showed d_{33} coefficients from 120 (at 30 kV/cm) to 150 (at 70 kV/cm) pC/N. Again, the highest d_{33} values were obtained for NBT-5.5 mol% BT textured ceramics, which showed d_{33} coefficients between 270 (at 30 kV/cm) to 520 (at 70 kV/cm) pC/N. This value (520 pC/N) is 44% higher than random ceramics and close to the value reported for single crystals (450 pC/N) of similar composition [1]. Since the d_{33} values for ceramic cannot be larger than single crystal values with similar domain status, it is likely that extra response is due to the higher hysteresis in the textured ceramics.

Figure 4.12 shows the variation of unipolar maximum strain of textured NBT-5.5 mol% BT ceramics textured with 5.5 vol% SrTiO₃ template particles plotted as function of Lotgering factor. Strains were reported at three different driving fields; namely 50, 60,

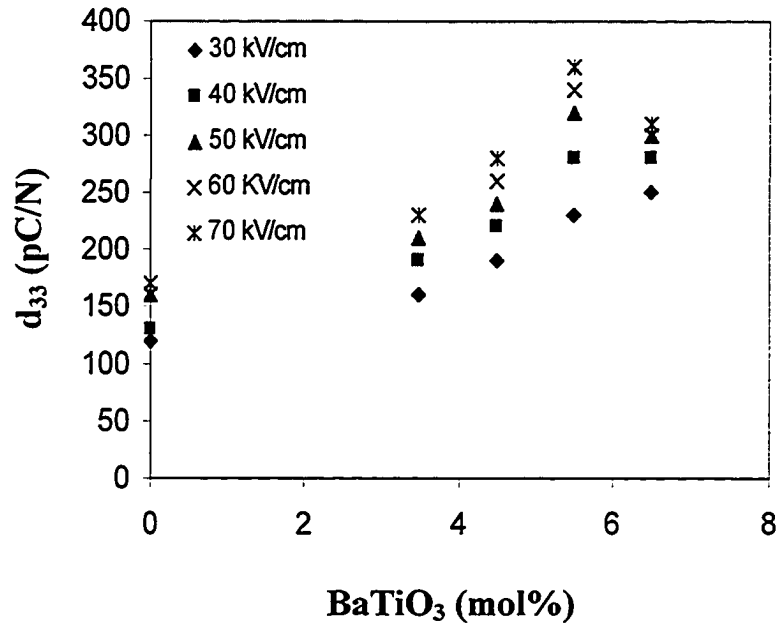


Figure 4.10. d_{33} coefficient of random ceramics plotted as function of % BT doping.

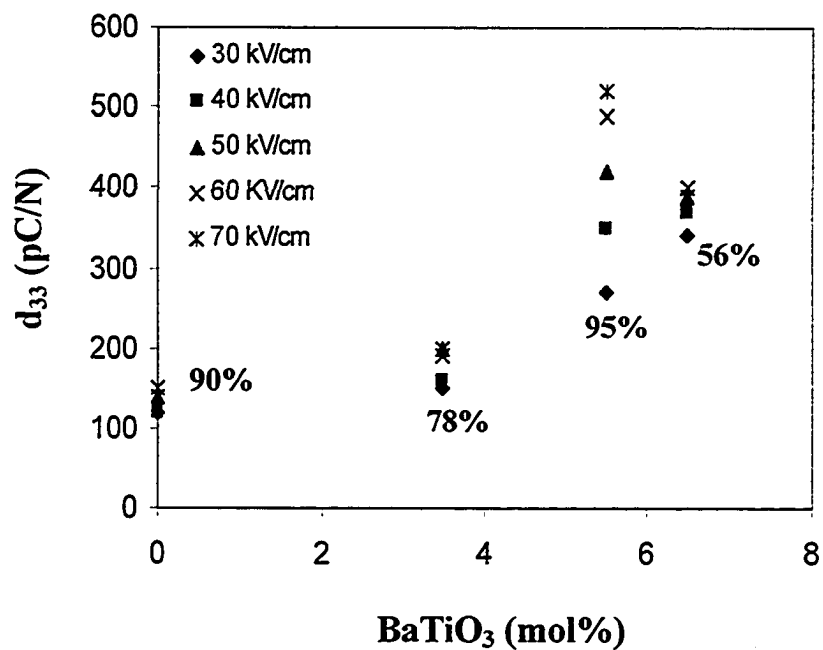


Figure 4.11. d_{33} coefficients of textured ceramics plotted as function of % BT doping, sintered at 1200°C for 12 h with 5 vol% SrTiO₃ templates. Numbers specify amount of texture (Lotgering factor).

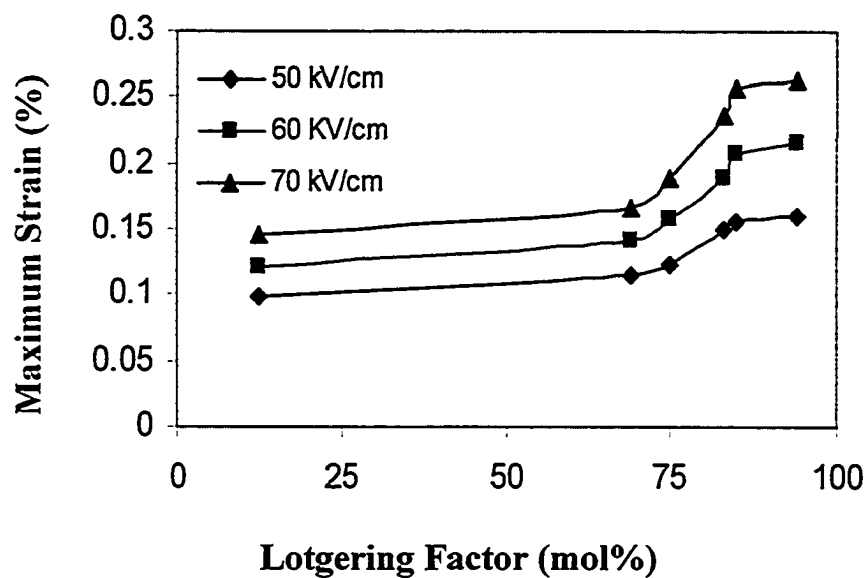


Figure 4.12. Unipolar maximum strain and maximum hysteresis of textured NBT-5.5 mol% BT ceramics textured with 5 vol% SrTiO₃ plotted as function of Lotgering factor.

and 70 kV/cm. It seems that for texture fractions lower than $f=70\%$, the maximum strain shown is a weak function of texture. For texture fractions greater than $f=70\%$ the maximum strain shown by the sample starts to increase when measured for the same driving field. The sample with $f=94\%$ texture shows 0.26% strain when measured at 70 kV/cm.

Figure 4.13 shows the variation of the high field d_{33} coefficient of NBT-5.5 mol% BT ceramics sintered at 1200°C for 12 hrs. with 5 vol% SrTiO₃ template particles. d_{33} coefficients were measured from the slope of unipolar strain-electric field curve as explained above. Measurements were performed at electric fields between 30 and 70 kV/cm. High field piezoelectric coefficients, for $f<70\%$ texture, were similar to the random ceramic values (~360 pC/N, measured @ 70 kV/cm). Ceramics with high texture ($f>70\%$) showed enhanced actuation (d_{33}). The highest d_{33} coefficient (520 pC/N) was obtained for the ceramic with $f=94\%$ texture. The d_{33} from Berlincourt measurement of random sample at MPB was 110 pC/N.

4.3.2.3 HYSTERESIS IN NBT CERAMICS

In all cases, the unipolar strain curves were accompanied by substantial hysteresis. Two approaches were taken to quantify the hysteresis. First hysteresis present in the samples was normalized, that is the maximum opening in the increasing and decreasing electric field was divided by the maximum strain in the sample. Secondly, the large signal $\tan\delta$, which is equivalent to large signal dielectric loss factor, were reported

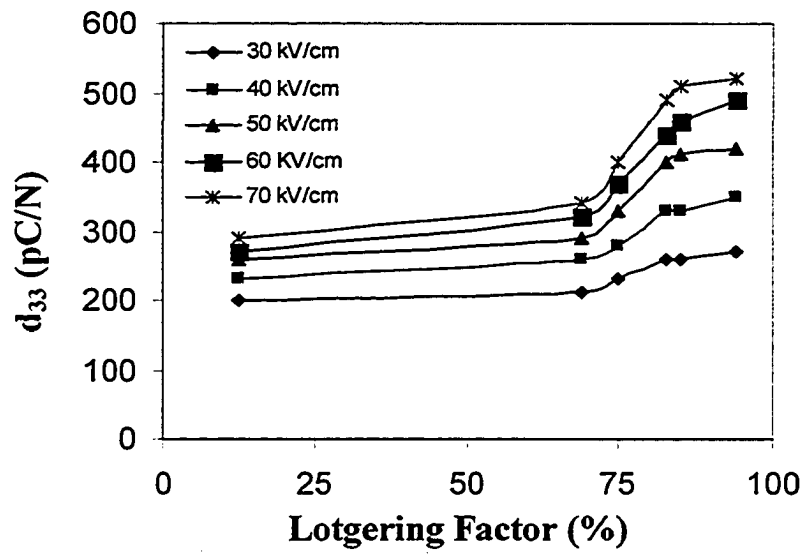


Figure 4.13. d_{33} coefficient of textured NBT-5.5 mol% BT ceramics textured with 5 vol% SrTiO_3 plotted as function of Lotgering factor, sintered at 1200°C for 12 h.

according to the protocol for calculation of the dielectric constant and piezoelectric coefficients for piezoelectric single crystals [9]. In this calculation polarization-electric field curves were divided into two sets; one set is the part that represents the polarization under increasing electric field curve and another set that represent the polarization under decreasing electric field. Then, the polarization data were curve fit to a fifth order polynomial, all fits were better than $R^2=99.8\%$. A third function (polynomial) is obtained from the average of the two fit equations. The large signal $\tan\delta$ were calculated using the fitted curves and the formula,

$$\tan \delta = \frac{A_{loop}}{[\pi(A_1 + A_2)]} \quad \text{Eqn. 4.2}$$

where A_{loop} is the area bound by the upper and lower curve, A_1 and A_2 are the areas as shown in the Figure 4.14.

The hysteresis (normalized hysteresis and large signal $\tan\delta$) vs. % BT graph is given in Figure 4.15. The driving electric field was 70 kV/cm. The first point to notice is that textured NBT ceramics were less hysteretic than the randomly oriented ceramics. The normalized hysteresis and large signal $\tan\delta$ for textured NBT ceramics were 15 % and 22 %, respectively. In contrast, the normalized hysteresis and large signal $\tan\delta$ for randomly oriented NBT ceramics were 27 % and 39 %, respectively. For undoped NBT ceramics the coercive field is high (~52 kV/cm) and almost the same for random and textured ceramics (Figure 4.5). Thus, it is believed that the lowering of hysteresis in the unipolar strain-field curves is due to the orientation distribution control in textured ceramics (Figures 4.16 and 4.17). The shape of the hysteresis curves are different for textured and randomly oriented ceramics.

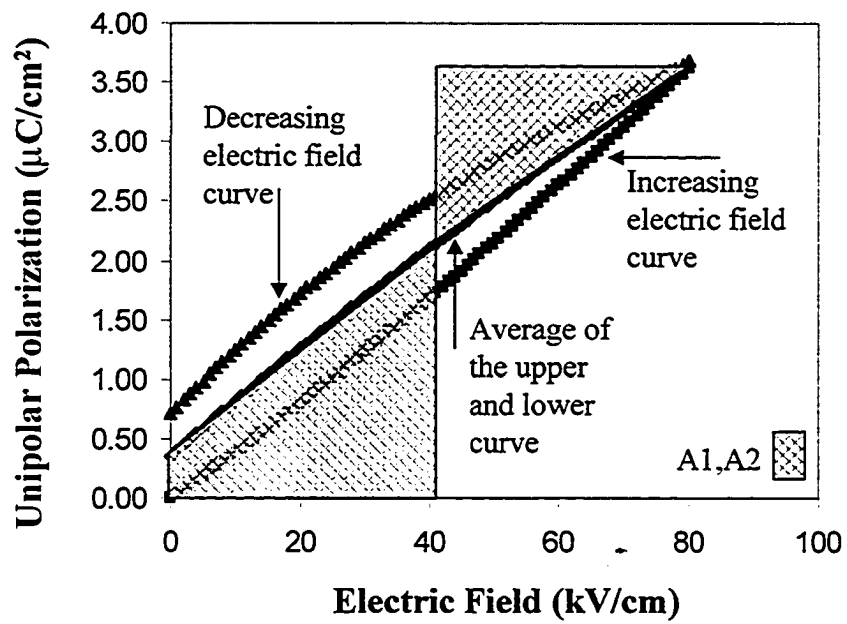


Figure 4.14. Schematic showing the areas used in the calculation of large signal dielectric loss factor.

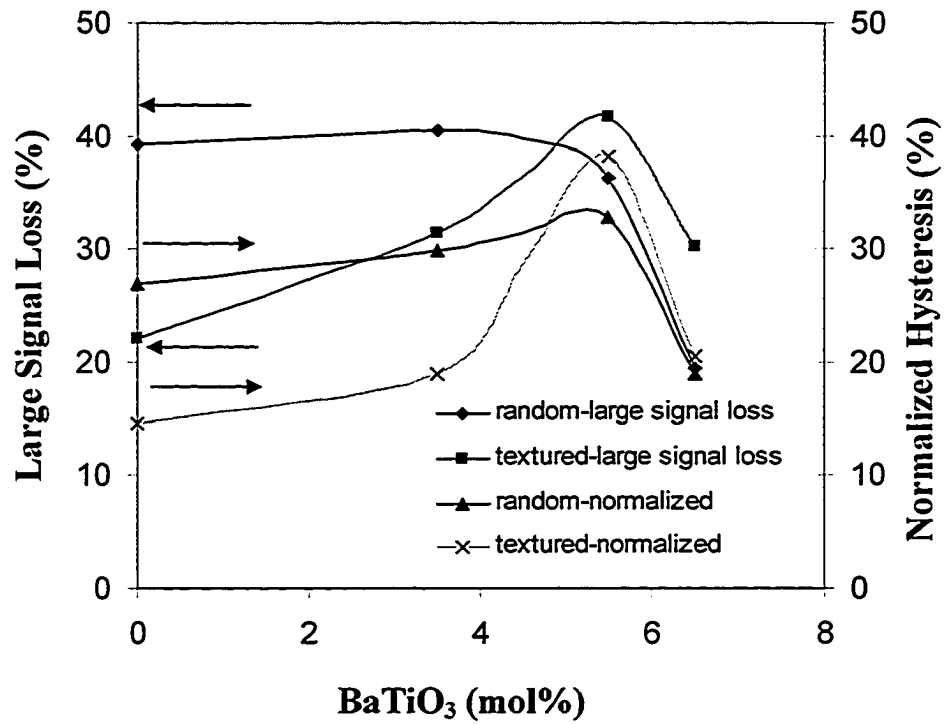


Figure 4.15. Comparison of large signal dielectric loss factor and normalized hysteresis measurements for randomly oriented and textured NBT ceramics at different BT doping levels. @70 kV/cm.

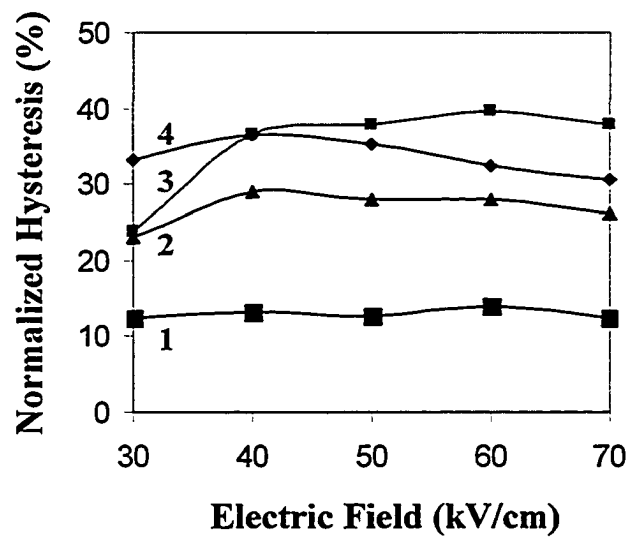


Figure 4.16. Normalized hysteresis measured for randomly oriented and textured NBT-0 % BT and NBT-5.5 % BT ceramics. 1) 0 mol% BT doped NBT textured ceramics, 2) 0 mol % BT doped NBT randomly oriented ceramics, 3) 5.5 mol% BT doped NBT textured ceramics, 4) 5.5 mol % BT doped NBT randomly oriented ceramics.

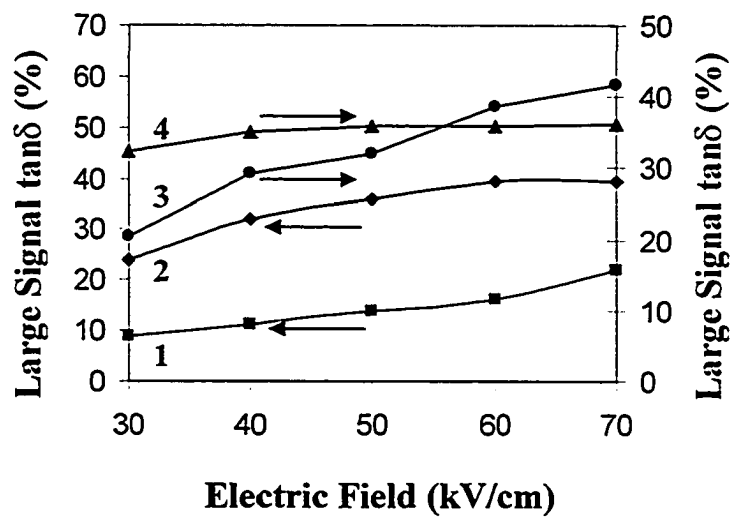


Figure 4.17. Large signal dielectric loss factor measured for randomly oriented and textured NBT-0 % BT and NBT-5.5 % BT ceramics. 1) 0 mol% BT doped NBT textured ceramics, 2) 0 mol % BT doped NBT randomly oriented ceramics, 3) 5.5 mol% BT doped NBT randomly oriented ceramics, 4) 5.5 mol % BT doped NBT textured ceramics.

On the other hand, the 5.5 mol % BT doped (MPB composition) textured samples were more hysteretic than randomly oriented samples. The normalized hysteresis and large signal $\tan\delta$ for textured 5.5 mol %BT doped ceramics were 38 % and 42 %, respectively. In contrast, the normalized hysteresis and large signal $\tan\delta$ for randomly oriented 5.5 mol %BT doped ceramics were 33 % and 36 %, respectively. The coercive fields for 5.5 mol %BT doped textured and randomly oriented ceramics were 28 and 34 kV/cm, respectively (Figure 4.5). As the composition gets closer to the MPB, due to the lowering of the coercive field and therefore easier switching in the domains, the curve gets more hysteretic.

In Figure 4.16, the normalized hysteresis for 0 and 5.5 mol% BT doped NBT ceramics are plotted as a function of driving fields. The undoped but textured ceramics showed half the hysteresis of the randomly oriented ceramics. The textured samples with MPB compositions were less hysteretic than the randomly oriented samples if the driving fields were below the coercive field (<40 kV/cm). However, if the driving fields were above the coercive field (>50 kV/cm), the hysteresis for textured MPB composition was large compared to the random sample. Randomly oriented and textured ceramics have different coercive fields. It is easier in the textured ceramic to move domain boundaries compared to the randomly oriented ceramics. Basically there are two mechanisms competing against each other. Orientation control favors low hysteresis whereas ease of domain movement due to low coercive field, as in textured ceramics, compensates for the lowering of hysteresis.

The large signal $\tan\delta$ vs. the driving field were also calculated using the navy protocol and are given in Figure 4.17 for two compositions, namely 0 and 5.5 mol % BT

doped randomly oriented and textured case. Undoped but textured NBT ceramics were less hysteretic than randomly oriented ones at all driving fields. At 70 kV/cm, the large signal $\tan\delta$ were 22 % and 39 % for textured and randomly oriented ceramics, respectively. For the MPB composition (5.5 mol % BT) large signal $\tan\delta$ for textured ceramics were smaller than the randomly oriented ones at low driving fields (<50 kV/cm). However, at high driving fields (>60 kV/cm), the large signal $\tan\delta$ for textured ceramics were a little higher than the randomly oriented ones. At 30 kV/cm, the large signal $\tan\delta$ were 20 % and 32 % for textured and randomly oriented ceramics, respectively. At 70 kV/cm, the large signal $\tan\delta$ were 42 % and 36 % for textured and randomly oriented ceramics, respectively. Comparing the two methods used to quantify texture, large signal $\tan\delta$ better picks up the electric field contribution to domain movement. That is, at higher driving fields the observed hysteresis is bigger. High piezoelectric coefficients were measured at high electric fields which is a clear indication of the contribution of the hysteresis to the piezoelectric coefficient. Similar effects have been reported in PZT [10-11], where the piezoelectric coefficient (d_{33}) has been reported to be a function of the amplitude of the electric field.

For undoped NBT ceramics the coercive field is high (~52 kV/cm) and almost the same for random and textured ceramics (Figure 4.5), therefore there is less domain movement that contributes to the hysteresis in the strain curve. So, the lowering of hysteresis is due to the orientation distribution control in textured ceramics (Figures 4.16 and 4.17). The coercive fields for 5.5 mol % BT doped textured and randomly oriented ceramics were 28 and 34 kV/cm, respectively (Figure 4.5), As the composition gets to the

MPB, due to the lowering of the coercive field and therefore easier switching in the domains, the curve gets more hysteretic.

The hysteresis behavior of the NBT ceramics calculated using normalized hysteresis and navy standards (large signal $\tan\delta$) are similar. However, the amount of hysteresis measured with these methods are different from each other. Hysteresis reported as large signal $\tan\delta$ were larger than the normalized hysteresis. Normalized hysteresis values were smaller because as the curve gets more hysteretic, the unipolar strain in the samples, which appears in the denominator, gets bigger, which leads to small values.

A comparison of the hysteresis data reported here to single crystal data would be of great importance. Since only unipolar strain curves were reported for single crystals, only normalized hysteresis data were compared. The unipolar strain curve of a $\text{Na}_{1/2}\text{Bi}_{1/2}\text{TiO}_3$ -2 mol% PbTiO_3 single crystal oriented in the $\langle 001 \rangle_{pc}$ was almost hysteresis free ($\sim 7\%$), but the piezoelectric coefficient measured from the slope of the strain vs. electric field curve was low (~ 165 pC/N) [12] as shown in Figure 2.7 in Chapter 2. The unipolar strain was about 0.1 % at 70 kV/cm [12]. The undoped but textured NBT ceramics showed a maximum unipolar strain of 0.09% at 70 kV/cm with a hysteresis of $\sim 15\%$. The samples prepared here are more hysteretic than the single crystal data. Much more of the loop is open, so that the average hysteresis is higher. It can be concluded that the normalized hysteresis in textured NBT ceramics was approximately twice the value reported for single crystals. Furthermore, the d_{33} coefficients were also comparable. d_{33} was 120 pC/N on the average (~ 170 pC/N when measured from the decreasing slope) for the textured ceramic (in this study) and ~ 165 pC/N for the single crystal doped with 2 mol% PbTiO_3 [12].

The unipolar strain data reported by Chiang et al. [1] would be more appropriate for comparison of the properties for MPB compositions. They reported that 5.5 mol% BaTiO₃ doped NBT single crystal was rhombohedral and showed 0.24% free strain at 60 kV/cm, (Figure 2.6 in Chapter 2). About 20% hysteresis was reported for the same sample. In the $\langle 001 \rangle_{pc}$ direction, a d_{33} coefficient as high as 450 pC/N [1] has been reported for flux grown single crystals at the morphotropic phase boundary with BaTiO₃. The following values were obtained for the textured ceramics with the same composition. NBT-5.5 mol% BT ceramics reached 0.26% strain at 70 kV/cm. This value (0.26% strain) is 62% higher than random ceramics. A high field d_{33} coefficient of 520 pC/N was measured. It is very encouraging that d_{33} values were comparable to the single crystal values and the hysteresis for textured ceramics were lower than the randomly oriented ceramics. However, it should be kept in mind that those single crystals were grown using flux method, that is it is highly probable that there are compositional variations in the single crystal, and defect formation due to the volatility of A site ions at high temperatures. In the textured ceramics these artifacts should not be as severe as in the case of single crystals. First of all, compositional variations in the sample were not expected as the ceramic was prepared from well mixed and calcined powders. The main source for compositional variations would be the vaporization of the A site cations from the sample at the sintering temperature. The weight loss from the sample at 1200°C was 0.6 % after a 1 min hold and 1 % after a 12 hour hold. It is also expected that most the weight loss is from the top and bottom surfaces of the sample. To minimize the impact of this on the properties, at least 250 μm of material was removed from the top and bottom

surfaces before applying any electrode for electrical property measurement. No compositional gradient across the sample thickness was detected in microprobe analysis.

It is clear from the review of the literature that the largest piezoelectric coefficients observed to date in $\text{Na}_{1/2}\text{Bi}_{1/2}\text{TiO}_3$ -based single crystals is coupled with substantial hysteresis [1]. One possible cause for high hysteresis [1] in the unipolar strain curve is related to the high temperature ferroelastic phase transition. The ferroelastic domain structure is set at high temperature, and does not move with electric field [13]. It is possible that the presence of this domain structure imposes some type of restoring force on the ferroelectric domain walls, so that an electric field applied to the rhombohedral phase only temporarily moves the domain boundary. If the field is removed the original domain configuration may be recovered, yielding appreciable hysteresis. The work of Park et al. [12] shown in Figure 2.7 in Chapter 2 suggests that this situation may be avoidable. An alternative explanation might be that the electric field required to induce a tetragonal phase transition is low in $\text{Na}_{1/2}\text{Bi}_{1/2}\text{TiO}_3$ - BaTiO_3 system. This would be consistent with the substantial poling strain observed in the work of Chiang and co-workers [1]. If so, then the extent of hysteresis should depend on proximity to the MPB in NBT-BT ceramics.

A third possibility is that some of the hysteresis is associated with either microheterogeneity or large concentrations of point defects. This is reasonable to consider in $\text{Na}_{1/2}\text{Bi}_{1/2}\text{TiO}_3$ due to the volatility of Na, Bi, and O. Then, it is highly likely that the defect dipoles present in the ceramics might pin the domain walls as acceptor doped PZT [14-15]. In Fe^{3+} doped PZT, Fe^{3+} -oxygen vacancy ($\text{V}_\text{O}^{\cdot\cdot}$) defect dipoles are formed. $\text{V}_{\text{Pb}^{\cdot\cdot}}-(\text{V}_\text{O}^{\cdot\cdot})$ complexes can also be formed due to lead vaporization during

sintering. The lead vacancies are positively charged and oxygen vacancies are negatively charged with respect to the neutral lattice [14-15]. Similarly, in NBT ceramics A site vacancies can be formed due to vaporization of Na and/or Bi from the perovskite lattice and lead to V_{Na} or $V_{Bi}(V_{O^{\cdot-}})$ defect dipole formation. One of the consequences of defect dipole formation is that domain boundary motion might be partially pinned, which contributes to the high levels of hysteresis seen in the ceramics.

4.3.2.4 DIELECTRIC PROPERTIES

In this section all dielectric behavior of randomly oriented and textured NBT ceramics were reported at 1 kHz unless otherwise notified. Ceramics were poled before measurement and $\tan\delta$ were about ~1 %. Undoped NBT has a room temperature dielectric constant of ~350. For compositions close to the morphotropic phase boundary the dielectric constant increases and the highest dielectric constants were measured for NBT-6.5 mol% BT ceramics. The dielectric constant for randomly oriented ceramics was ~750 whereas the dielectric constant for a textured ceramic was ~950, with the same composition. The maximum dielectric constants measured for the composition with 5.5 mol% BT doped ceramics were for randomly oriented ($\epsilon_{max}\approx 6600$) and textured ceramics ($\epsilon_{max}\approx 5800$).

The transition temperatures (T_{tr}) were obtained based on dielectric property measurements. The transition from rhombohedral to tetragonal for undoped NBT starts at ~230°C [3]. In our measurements, this transition temperature was lower than the one reported in the literature because of the presence of Mn (0.3 wt% $MnCO_3$) doping to

increase the resistivity and enhance grain growth. A T_r of $\sim 184^\circ\text{C}$ was measured for randomly oriented ceramics, whereas a T_r of $\sim 146^\circ\text{C}$ was measured for textured NBT ceramics with 5 vol% SrTiO_3 templates. The further lowering of the transition temperature with texturing may be attributed to dissolution of the small SrTiO_3 template particles (0.7 mol% SrTiO_3). In all of the compositions (< 6.5 mol% BT) studies, T_r was lower for textured ceramics than randomly oriented ceramics. All the measurements were done on heating of poled ceramics. Figure 4.18 shows the dielectric constant vs. temperature behavior of randomly oriented and textured NBT-5.5 mol% BT (5 vol% SrTiO_3 template particles) ceramics sintered at 1200°C for 12 hrs. The rhombohedral-tetragonal transition temperatures (to mixed phase region) for randomly oriented and textured ceramics were 125°C and 105°C , respectively. The transition temperatures of textured samples did not change with sintering time. The maximum dielectric constant was also suppressed for the textured ceramic relative to the random materials, probably due to the presence of a low dielectric constant phase, i.e. SrTiO_3 template particles.

Figure 4.19 shows the variation of dielectric constant of NBT-5.5 mol% BT ceramics textured using 5 vol% SrTiO_3 template particles as a function of texture fraction. The dielectric constant increases with increasing texture fraction from ~ 510 for randomly oriented ceramic to ~ 650 for $f=94\%$ textured ceramics. From the directional dependence of dielectric constant, the maximum dielectric constant of many rhombohedral ferroelectric perovskites is observed in the direction perpendicular to the

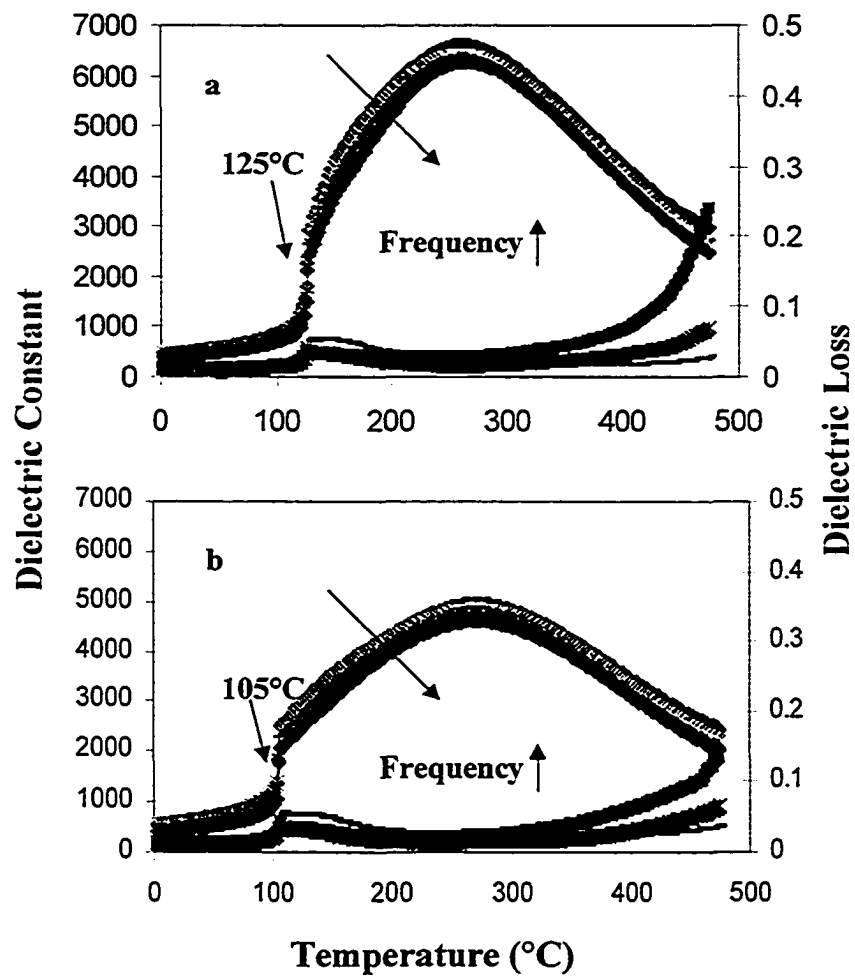


Figure 4.18. Dielectric constant (@ 1, 10, 100, and 1000 kHz) vs. temperature behavior of randomly oriented (a) and textured (b) NBT-5.5 mol% BT ceramics, sintered at 1200°C for 12 hrs. and measured on heating. Dielectric loss is reported @ 1, 10 and 100 kHz.

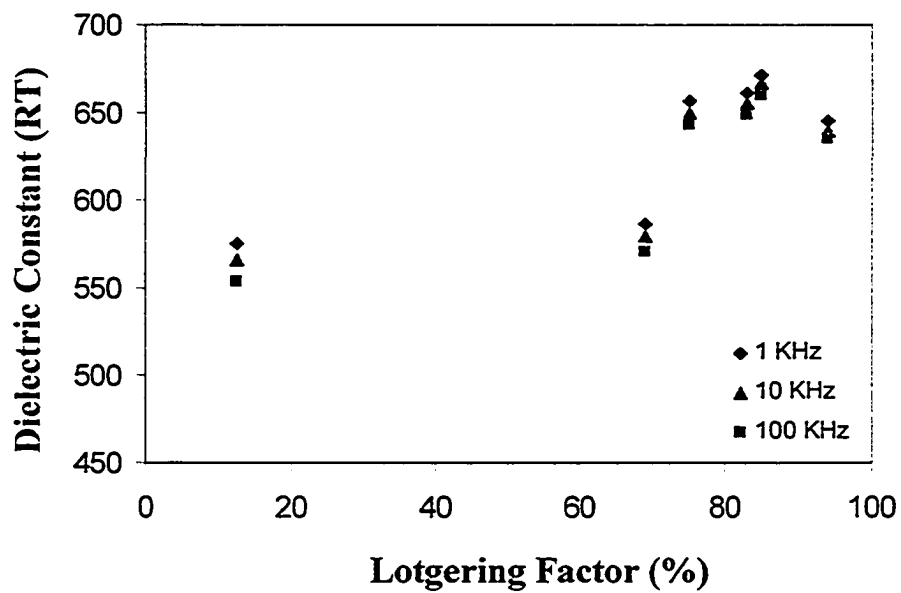


Figure 4.19. The variation of room temperature dielectric constant of NBT-5.5 mol% BT ceramics (5 vol% SrTiO₃ templates) as function of texture fraction, sintered at 1200°C for 12 h.

polarization direction, i.e. $\langle 111 \rangle_{pc}$ [8]. So, for the textured ceramic, the maximum dielectric constant is located at around 35.7° away from measurement direction. However, for the randomly oriented ceramic, in which the pole density of maximum dielectric constant is equal in all directions, the averaging of dielectric constant in all possible directions resulted in lower dielectric constant than textured ceramics. Another source for the difference in room temperature dielectric constant is the shift in T_r .

4.4 ELECTRICAL PROPERTIES OF $\text{Bi}_4\text{Ti}_3\text{O}_{12}$ TEMPLATED $\text{Na}_{1/2}\text{Bi}_{1/2}\text{TiO}_3$ - BaTiO_3 CERAMICS

The objective in studying the BiT templated ceramic was to compare the electrical properties to the ceramic textured using SrTiO_3 templates. The presence of a non-ferroelectric phase at the center of each grain might degrade the electrical and electromechanical properties due to dilution, clamping and field inhomogeneities. The NBT-5.5 mol% BT composition was textured using 6 vol% BiT template particles. As noted in Chapter 3, BiT templated systems were very sensitive to the pre-reaction condition.

In Figure 4.20 the dielectric constant measured as a function of temperature for textured and untextured NBT-5.5 mol% BT ceramics were given. These measurements were performed for unpoled ceramics. The room temperature dielectric constant for textured ceramic (~ 1400) was higher than the randomly oriented ceramics (~ 1000), as it is expected for a ceramic with rhombohedral symmetry. The maximum dielectric constants and the corresponding temperatures for textured and untextured ceramics were 7000 - 250°C and 7100 - 245°C , respectively.

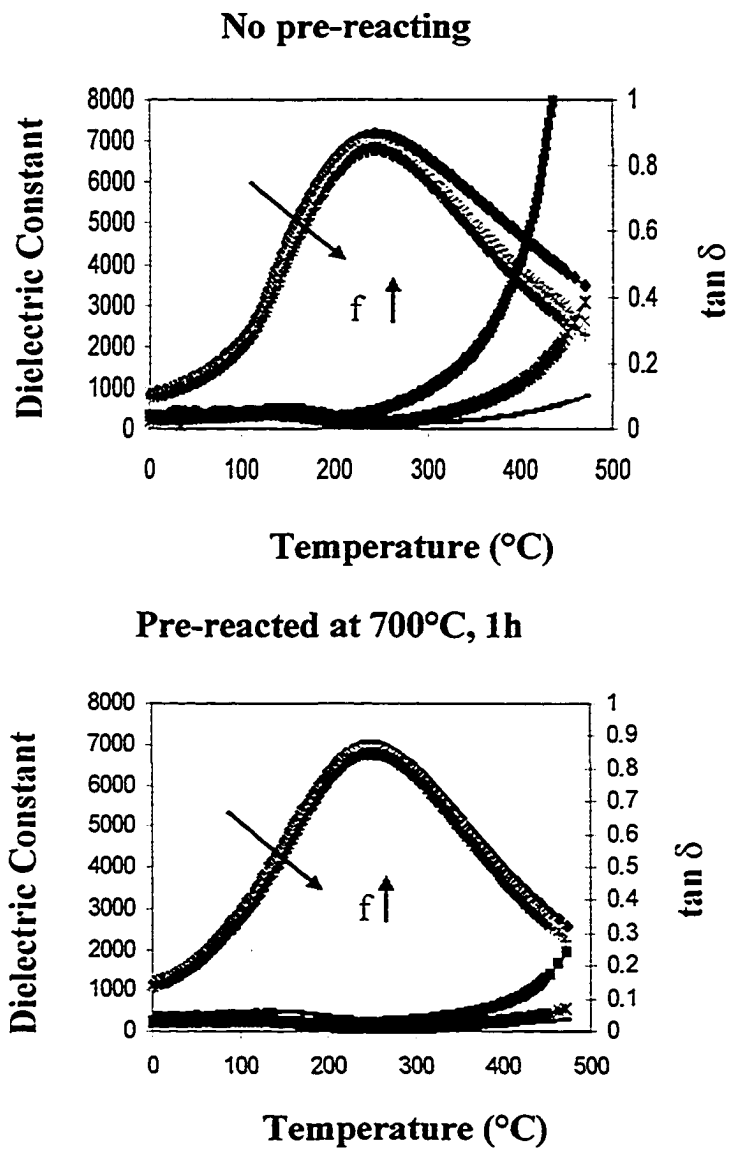


Figure 4.20. Dielectric constant of NBT-5.5 mo% BT ceramics: a) randomly oriented ceramics, b) textured using 6 vol% BiT template particles.

The amount of texture in BiT templated systems are dependent on the pre-reaction temperature and time. The unipolar strain curves for the same ceramics but for different pre-reaction conditions are given in Figure 4.21. Those ceramics were all sintered at 1200°C for 12 hrs. However, two of them were pre reacted at 700 and 800°C for 1 hr before they were taken to the sintering temperature. The ceramic that was directly heated to the sintering temperature did not develop any texture. Therefore, the maximum unipolar strain was low, ~0.15% strain with a d_{33} of ~260 pC/N @ 70 kV/cm was measured from the slope of decreasing electric field as described before. However, the other two ceramics that were pre-reacted were textured to about $f=80\%$. Therefore, those ceramics had much steeper unipolar strain curves. The maximum unipolar strain of ~0.26% strain with a d_{33} of ~490 pC/N @ 70 kV/cm were measured from the slope of decreasing electric field for the ceramic that was pre-reacted at 800°C for 1 hr.

However, it should be noted that for the textured ceramics, the unipolar strain curve gets more hysteretic. This result is consistent with the previous hysteresis behavior of SrTiO₃ templated MPB composition ceramics, where randomly oriented ceramics were more hysteretic than textured ceramics. The normalized hysteresis for the ~80 % textured ceramic was ~34 % whereas it was ~28 % for untextured ceramics Figure 4.21. Untextured ceramics obtained either by sintering the matrix powder without any template particles or by sintering BiT templated ceramics without any pre-reaction yield similar unipolar maximum strain (~0.15 %) and normalized hysteresis (~30%). Large signal $\tan\delta$ were also calculated for the same ceramics. At 70 kV/cm, the large signal $\tan\delta$ were 20%

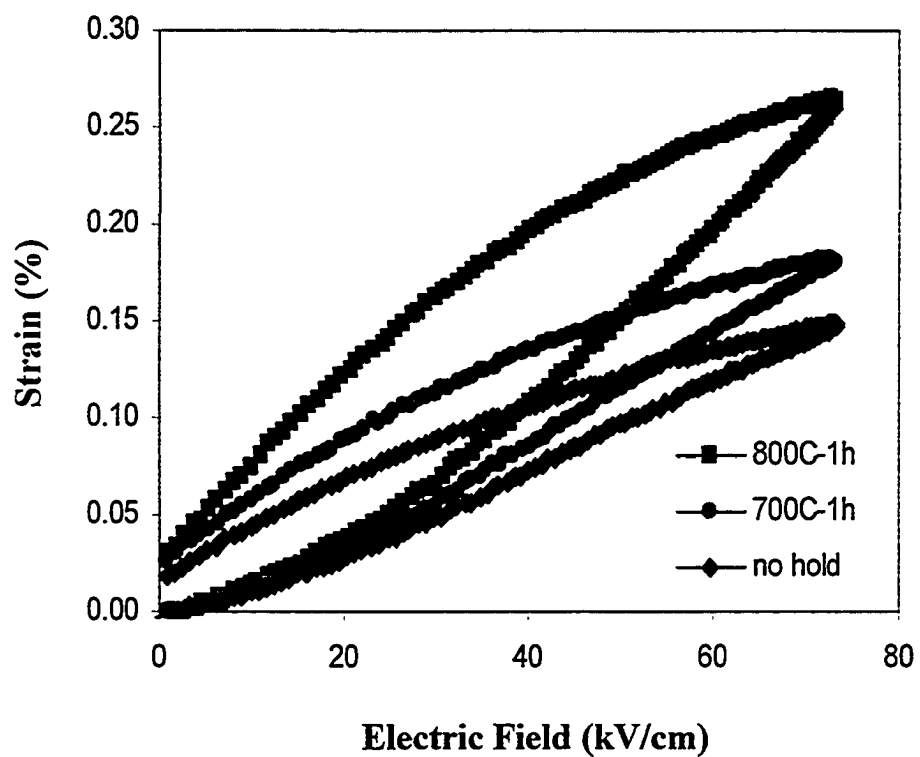


Figure 4.21. Unipolar strain curves of three of NBT-5.5 mo% BT ceramics at different pre-reaction conditions.

for untextured (no hold), 25% for 1 hour hold at 700°C and 34% for 1 hour hold at 800°C.

4.5 CONCLUSIONS

NBT-BT ceramics with 0 mol % to 6.5 mol % BT were textured using 5 vol% SrTiO₃ template particles. Texture fractions up to $f=94\%$ were obtained as measured by the Lotgering factor. There is a good correlation between texture fraction and the electrical and electromechanical properties. This relation is not linear. Enhancements in the properties were observed at high texture fractions ($f>70\%$).

$\langle 001 \rangle_{pc}$ oriented rhombohedral single crystals show high strain and piezoelectric coefficients. The same concept is also valid for $\langle 001 \rangle_{pc}$ oriented rhombohedral NBT-BT ceramics. Piezoelectric coefficients higher than randomly oriented ceramics but close to the single crystal values were obtained. The highest piezoelectric coefficient of 520 pC/N was measured for a textured sample with 5.5 mol% BT doping, on the rhombohedral side of the MPB. Considerable hysteresis in the strain response was observed. The piezoelectric coefficient from Berlincourt was $d_{33} \sim 200$ pC/N for the same sample.

Hysteresis reported as large signal $\tan\delta$ were larger than normalized hysteresis. The Large signal $\tan\delta$ better picks up the electric field contribution to domain movement.

4.6 REFERENCES

1. Y. M. Chiang, G. W. Farrey, A. N. Soukhojak, "Lead-Free High-Strain Single-Crystal Piezoelectrics in the Alkaline-Bismuth-Titanate Perovskite Family," *Applied Physics Letters*, **73**, 3683 (1998).
2. S. E. Park, and T. R. Shrout, "Ultrahigh Strain and Piezoelectric Behavior in Relaxor Based Ferroelectric Single Crystals," *J. Appl. Phys.*, **82** (4) 1804-1811 (1997).
3. T. Takenaka, and H. Nagata, "Present Status of Non-Lead Based Piezoelectric Ceramics," *Key Engineering Materials*, **157-158**, 57-64 (1999).
4. T. Takenaka, K. Maruyama, and K. Sakata, " $\text{Na}_{1/2}\text{Bi}_{1/2}\text{TiO}_3\text{-BaTiO}_3$ System for Lead-Free Piezoelectric Ceramics," *Jap. J. Appl. Phys.*, **30** [9b], 2236-9 (1991).
5. H. J. Bunge, "Grain Orientation and Texture," Ch. 41 in Industrial Applications of X-Ray Diffraction. Edited by F. H. Chung, and D. K. Smith. Marcel Decker Inc, New York, 2000.
6. H. Yilmaz, G. L. Messing, and S. Trolier-McKinstry, "(Reactive) Templated Grain Growth of Textured Sodium Bismuth Titanate ($\text{Na}_{1/2}\text{Bi}_{1/2}\text{TiO}_3\text{-BaTiO}_3$) Ceramics I," To be published.
7. S. B. Vakhrushev, B. G. Ivanitskii, B. E. Kvyatkovskii, and A. N. Maistrenko, "Neutron Scattering Studies of the Structure of Sodium Bismuth Titanate," *Sov. Phys. Solid State*, **25** [9] p 1504-6 (1983).
8. X. H. Du, U. Belegundu, and K. Uchino, "Crystal Orientation Dependence of Piezoelectric Properties in Lead Zirconate Titanate: Theoretical Expectations for Thin Films," *Jpn. J. Appl. Phys.*, **36** Part 1 No 9A 5580-5587 (1997).

9. H. C. Robinson, "Large Signal Dielectric Losses in Electrostrictive Materials," Proceedings of the 7th SPIE Symposium on Smart Materials and Structures, Newport Beach, CA, March 2000.
10. S. Li, W. Cao, and L. E. Cross, "The Extrinsic Nature of Nonlinear Behavior Observed in Lead Zirconate Titanate Ferroelectric Ceramics," J. Appl. Phys. **69** [10] pp. 7219-24 (1991).
11. Q. M. Zhang, H. Wang, N. Kim, and L. E. Cross, "Direct Evaluation of Domain-wall and Intrinsic Contributions to the Dielectric and Piezoelectric Response and Their Temperature Dependence on Lead Zirconate-Titanate Ceramics," Appl. Phys. **75** [1] pp. 454-59 (1994)
12. S. E. Park, Private communication.
13. A.N. Soukhovjak, H. Wang, G.W. Farrey, and Y.-M. Chiang, "Superlattice in Single Crystal Barium-Doped Sodium Bismuth Titanate," J. Phys. Chem. Solids, **61** [2] pp.301-304 (2000).
14. B. Jaffe, W. R. Cook, and H. Jaffe, Piezoelectric Ceramics, Academic Press, New York, 1971.
15. W. L. Warren, G. E. Pike, K. Vanheusden, D. Dimos, B. A. Tuttle, and J. Robertson, "Defect-Dipole Alignment and Tetragonal Strain in Ferroelectrics," J. Appl. Phys., **79** [12] pp. 9250-57 (1996).

Chapter 5

ELECTRON BACKSCATTER DIFFRACTION (EBSD) CHARACTERIZATION OF NBT-BT CERAMICS

5.1 INTRODUCTION

In 1928 Kikuchi observed electron diffraction through a thin mica crystal [1]. He described the occurrence of the lines which carry his name. Later, a similar diffraction pattern was also observed in the back reflection mode [2]. It was not until 1967 that the first pseudo Kikuchi lines were observed by SEM [3] (Scanning Electron Microscopy); these were later named a SACP (Selected Area Electron Channeling Pattern) [4]. Practically, the spatial resolution in SACP was 10 μm (3 μm theoretically), and was mainly controlled by the spherical aberration coefficient (C_s) of the objective lens of the microscope [5].

The first pattern indexing and orientation calculations using the technique known as EBSD (electron backscatter diffraction) were demonstrated by Venables and his coworkers at Sussex University [6-8]. EBSD is superior to SACP because of its high spatial resolution. Furthermore, because a wide angular range is recorded in the pattern, low symmetry crystals can be interpreted more easily [9]. Nowadays, all EBSD systems utilize live video imaging and computer assisted indexing.

5.2 ORIENTATION IMAGING MICROSCOPY

Orientation Imaging Microscopy (OIM) is used interchangeably with Electron BackScatter Diffraction (EBSD). In EBSD, a Kikuchi pattern is formed on a phosphorus screen and recorded via a CCD camera. The Kikuchi pattern is digitally analyzed to obtain the crystallographic orientation of each data point, Figure 5.1. EBSD is an attachment to a SEM. In SEM each electron beam spot on the sample surface leads to a Kikuchi pattern. Analysis of the Kikuchi patterns leads to quantitative texture characterization.

The OIM system used in this work consists of two parts: hardware and software, both of which are supplied from TexSEM Laboratories (Provo, Utah), Figure 5.2 [10]. The hardware is an attachment to the SEM (Model JSM, JEOL, Tokyo, Japan) that basically controls the scanning hardware and captures the image digitally from the phosphorus screen with a highly sensitivity CCD camera. The software analyzes the Kikuchi pattern in the digital image at every step, as the electron beam is scanned across the sample surface to obtain the orientation information from the spot where the beam is pointing. The components of the orientation imaging system are shown in Figure 5.2.

Image formation on the phosphorus screen is shown schematically in Figure 5.3 [10]. A flat specimen is tilted with respect to the incident e-beam at about 70° to enhance the contrast. A phosphorus screen on which the image is formed is located in the forward scattering geometry. The highly sensitive CCD camera, located behind the phosphorus screen, captures the image digitally for further processing with the hardware and software analysis.

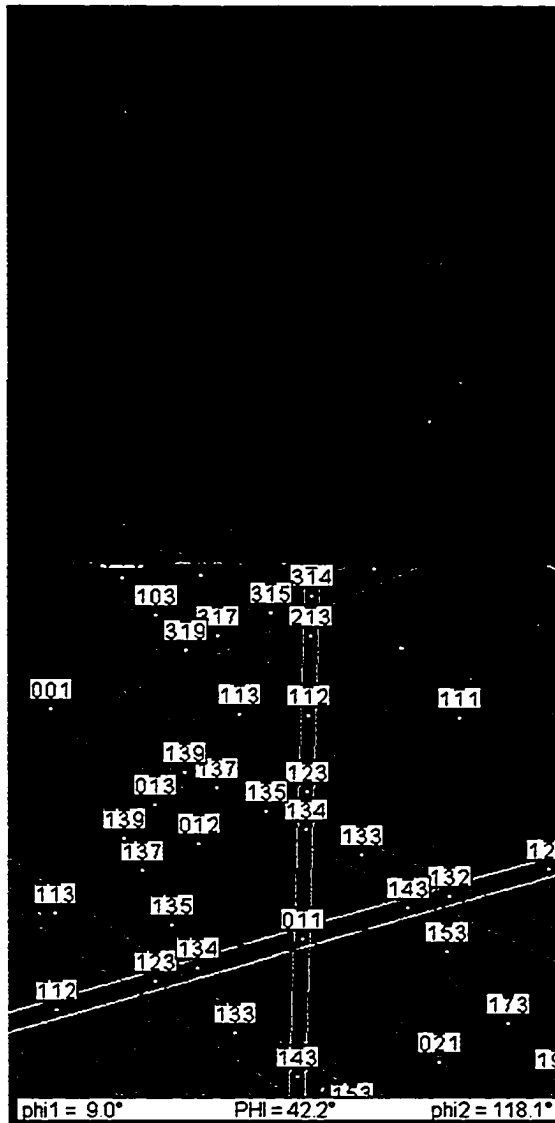
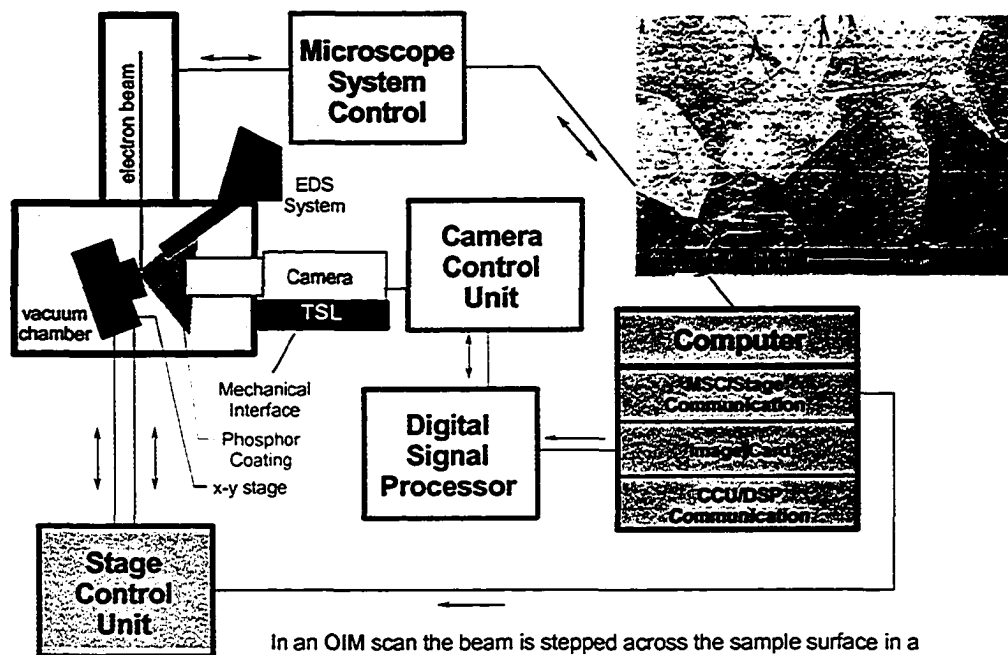


Figure 5.1. Kikuchi pattern of $\text{Na}_{1/2}\text{Bi}_{1/2}\text{TiO}_3$ -5.5 mol % BaTiO_3 grain captured by the CCD camera (Top). Indexed pattern (Bottom). (pc=pattern center)



In an OIM scan the beam is stepped across the sample surface in a regular grid. At each point the EBSP is captured and automatically indexed and the orientation and other information recorded (such as the pattern quality of the EBSP, an indexing reliability factor, the secondary detector intensity and EDS data.)

Figure 5.2. The components of the orientation imaging system; Electron Source (typically a SEM), Phosphor Screen, Mechanical Interface, Camera System, Lens/Fiber Optic Bundle, Digital Signal Processor, Computer/Video Card, Microscope System Control Electronics. Figure from [10].

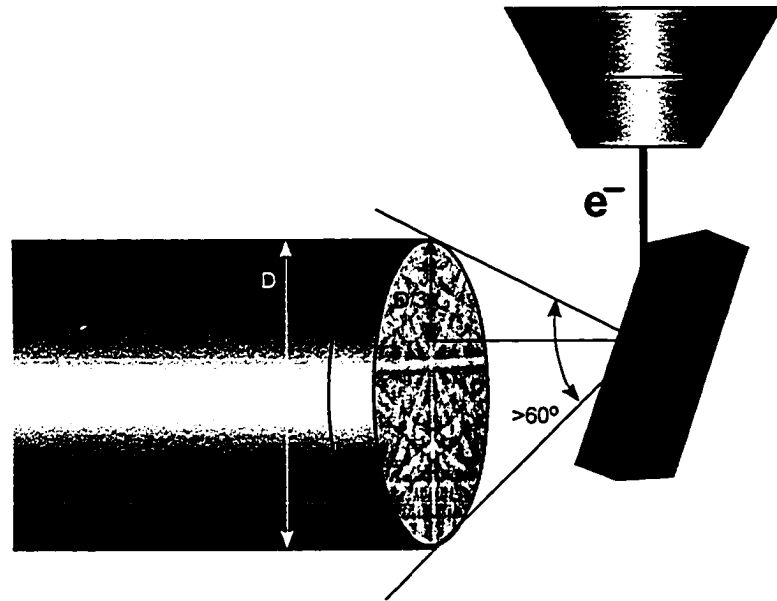


Figure 5.3. The position of the sample in the SEM chamber and image formation on the phosphorus screen. Figure from [10].

There are only linear features (lines) in the Kikuchi pattern, Figure 5.1. To identify a linear feature in the image, a Hough transformation [11] is used. Any linear feature will appear as a peak in Hough space. Taking three peaks at a time (three Kikuchi lines) in different combinations, the Kikuchi lines are indexed by looking at the angles between them. In a routine analysis, three images can be processed in a second, depending on the image quality and contrast. Therefore, a vast amount of data points can be analyzed and stored in a very short time. These stored data points are used to generate maps and pole figures [10].

The usefulness of OIM lies in the scale of the volume from which orientation information is obtained. Since the size of the e-beam is very small relative to the grain size, quantitative information is obtained about the orientation distribution of the grains in the sample. With this information, pole figures, inverse pole figures, rocking curves, grain size, and proof of (hetero)-epitaxy can be obtained.

If the tetragonal distortion or rhombohedral tilt is low (below the detection limit) then the indexing of the Kikuchi pattern has to be done using the high temperature cubic phase as the prototype. Therefore, the rhombohedral crystal structure is treated as cubic.

Texture in rolled metals is a very common phenomenon and has been studied for a long time for aluminum, iron, copper etc. [12-16]. OIM is an effective method for studying recrystallization in deformed metals [17-18]. The use of OIM in ceramics has become more popular recently. Duran et al. [19] employed OIM to characterize texture in strontium barium niobate tungsten bronze structures textured in the [001] direction. Khan et al. [20] studied the seeded growth of PMN-35% PT single crystals using OIM. The presence of crystal defects, like entrapped grains, voids, and second phases in the grown

single crystals was demonstrated. Ernst et al. [21] studied the presence of $\Sigma=3$ $\{111\}$ grain boundaries (twin boundaries) in polycrystalline perovskite ceramics like BaTiO_3 , SrTiO_3 , and PZT5A. From the orientation relations of the neighboring grains, significant preference for $\Sigma=3$ ($\{111\}$ twins) boundaries was reported. A twin boundary involves a BaO_3 $\{111\}$ plane as the common boundary plane and the nearby oxygen octahedra share faces instead of corners [22].

Sample preparation for OIM requires special care because the quality of the diffraction pattern is very sensitive to the surface quality and surface contamination [10]. Sample charging in OIM is a severe limitation for insulating samples. The electrons accumulate on the surface (surface charging) and destabilize the beam, leading to a distorted diffraction pattern [23]. The most commonly employed techniques to prevent charging are carbon coating the sample and use of a low vacuum environment in the specimen chamber [20, 23]. The diffracted electrons that form the image come from a depth of less than 20 nm. Therefore, any coating that is thick will severely degrade the signal quality [24]. Even with a very thin carbon coating the image is blurred, so the recommended coating thickness is <5 nm [10]. High atomic weight elements, like gold, are not recommended. In a low vacuum environment, positive ions generated in the chamber neutralize the surface charge [19].

5.3 EXPERIMENTAL PROCEDURE

Surface charging is a limitation in OIM. However, sometimes surface charging does not greatly affect the contrast in the Kikuchi pattern. In that case, it is not absolutely necessary to coat the sample for prevention of charging. In this work, the sample was attached to the sample holder with conducting tape. Areas close to the conducting tape were scanned to minimize artifacts due to surface charging. Scanning was conducted as quickly as possible so that the duration time of the e-beam on the same spot was minimized [10].

The samples were first embedded in an epoxy (Leco) for easy handling. Then, the surface was successively ground using 600, 800 (Leco), and 5000 (Buehler) grit papers. Fine polishing was done using diamond paste (Leco) with sizes of 6, 1, and 0.1 μm followed by 50 nm colloidal silica (pH=9), for about 20 minutes each. Then, the sample was sonicated in acetone to clean the surface.

To define the grain orientation, the reference coordinate axes used were labeled the “rolling direction [100]” (RD), “transverse direction [010]” (TD), and “normal direction [001]” (ND), the latter one is normal to the surface to be analyzed. These terms are adopted from the metallurgy community where texture is described in a rolled metal [21].

There are several parameters in the OIM software that need to be set before starting any analysis [10]. A grain boundary is defined when the angular deviation of successive points differs more than 3° . Raw data were filtered for questionable points that may occur at surface defects and grain boundaries. Special care was given not to alter the grain shape substantially. Crystal structure information (m3m) and lattice parameter (3.91

Å) were preset in order to index the Kikuchi patterns [10]. SrTiO₃ (3.9 Å) and Na_{1/2}Bi_{1/2}TiO₃ (3.89 Å) have similar lattice parameters.

5.4 RESULTS AND DISCUSSION

5.4.1 RANDOM CERAMICS

Figure 5.4 shows the OIM map of a randomly oriented Na_{1/2}Bi_{1/2}TiO₃-5.5 mol% BaTiO₃ ceramic. Any two points on the sample surface whose orientations differ by more than 3° are considered to belong to different grains. To construct this image, 17286 data points were used whose CI (Confidence Index), which is a quantification of the reliability of indexing, was 0.69 on the average. The CI can vary between 0 and 1. Any value greater than 0.2 is considered good [10]. The map can be thought of as equivalent to an SEM image of the sample with an average grain size of ~30 μm. Also, there are few special grain boundaries, like {111} twins, which will appear as straight lines [21]. Most of the grains were twin free which suggests that grain growth mechanism is not re-entrant edge grain growth mechanism but probably a normal grain growth mechanism.

For a randomly oriented ceramic, the distribution of orientations is equally probable in 3-D space. One way of searching for signs of crystallographic texture is to plot a pole figure (Figure 5.5) and/or inverse pole figure (Figure 5.6). If the density of poles is equally distributed, then the grains are randomly distributed. From the [001]_{pc} pole figure and inverse pole figure given Figures 5.5 and 5.6, respectively it is clear that the sample is randomly oriented.



Figure 5.4. OIM map of $\text{Na}_{1/2}\text{Bi}_{1/2}\text{TiO}_3\text{-BaTiO}_3$ random ceramics based on crystallographic orientation. Sintered at 1200°C for 12 hrs.

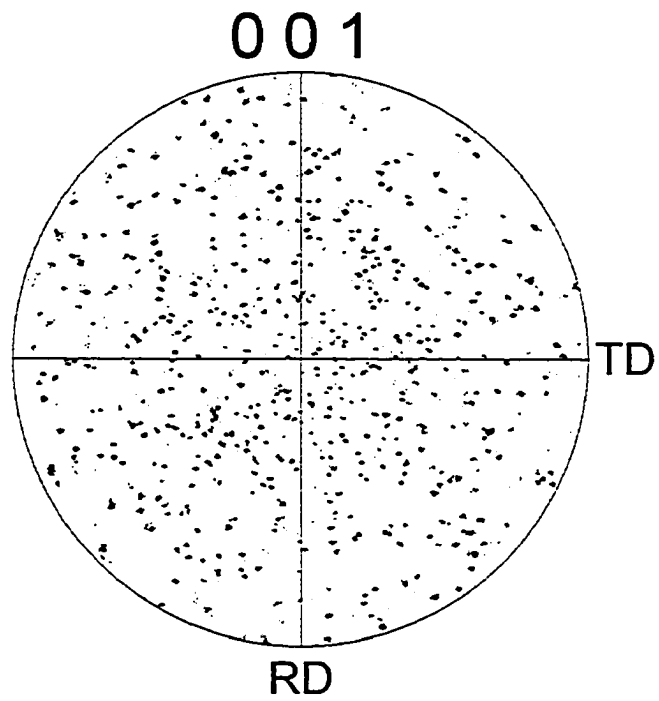


Figure 5.5. [001] pole figure of the $\text{Na}_{1/2}\text{Bi}_{1/2}\text{TiO}_3\text{-BaTiO}_3$ random ceramic.

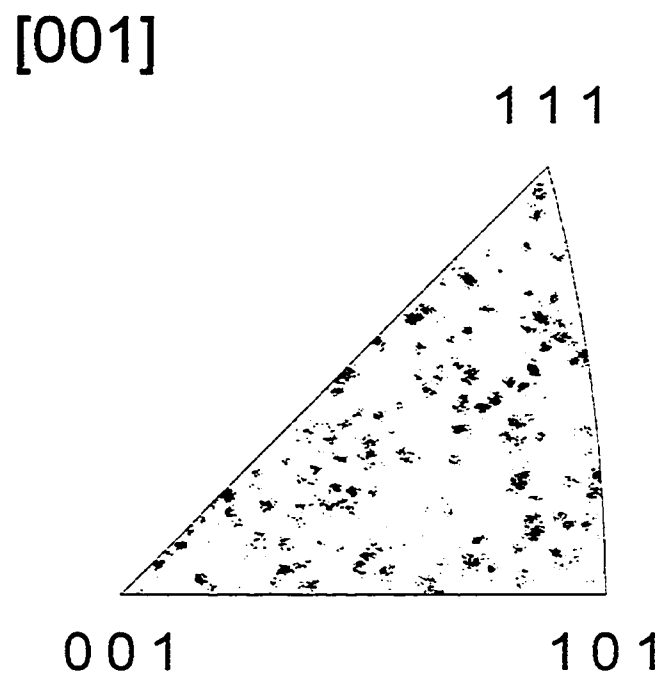


Figure 5.6. Inverse pole figure of $\text{Na}_{1/2}\text{Bi}_{1/2}\text{TiO}_3\text{-BaTiO}_3$ random ceramic.

5.4.2 TEXTURED CERAMICS

Figure 5.7 shows the SEM image of a textured $\text{Na}_{1/2}\text{Bi}_{1/2}\text{TiO}_3$ -5.5 mol% BaTiO_3 ceramic. The texture direction ($[001]_{\text{pc}}$) is shown in the figure. The large rectangular grains are the SrTiO_3 seeded $\text{Na}_{1/2}\text{Bi}_{1/2}\text{TiO}_3$ -5.5 mol% BaTiO_3 grains.

Figure 5.8 shows a color coded crystal orientation map of a $[001]_{\text{pc}}$ textured $\text{Na}_{1/2}\text{Bi}_{1/2}\text{TiO}_3$ -5.5 mol% BaTiO_3 ceramic. $[001]_{\text{pc}}$ oriented seeded grains, denoted in red, are dominant in the image. The other colors indicate orientations other than $[001]_{\text{pc}}$.

The phases in OIM are distinguished based on the crystal structure parameters, symmetry and lattice parameters. However, in some cases the differences in crystal structure can be below the detection limit of the equipment. Another way of differentiating phases is based on the chemistry. While analyzing the orientation of individual spots, an EDX detector analyses the chemistry of the very same spot and the information is saved with the orientation data. The crystal structure differences between SrTiO_3 template particles and $\text{Na}_{1/2}\text{Bi}_{1/2}\text{TiO}_3$ -5.5 mol% BaTiO_3 are below the detection limit of the equipment. The orientation analysis is done by assuming that the crystal structure is cubic and the material is homogeneous and single phase.

A qualitative way of distinguishing phases is the image quality (IQ) map. The quality of the diffraction pattern is material dependent because the atomic scattering factor is a function of atomic number [10]. Therefore, it is possible to construct a map that is based on image quality, to see the different phases in the image. It should be remembered that there are also other factors that affect the image quality of the diffraction pattern, like deviation from crystal ideality, and resolution of the electron beam.

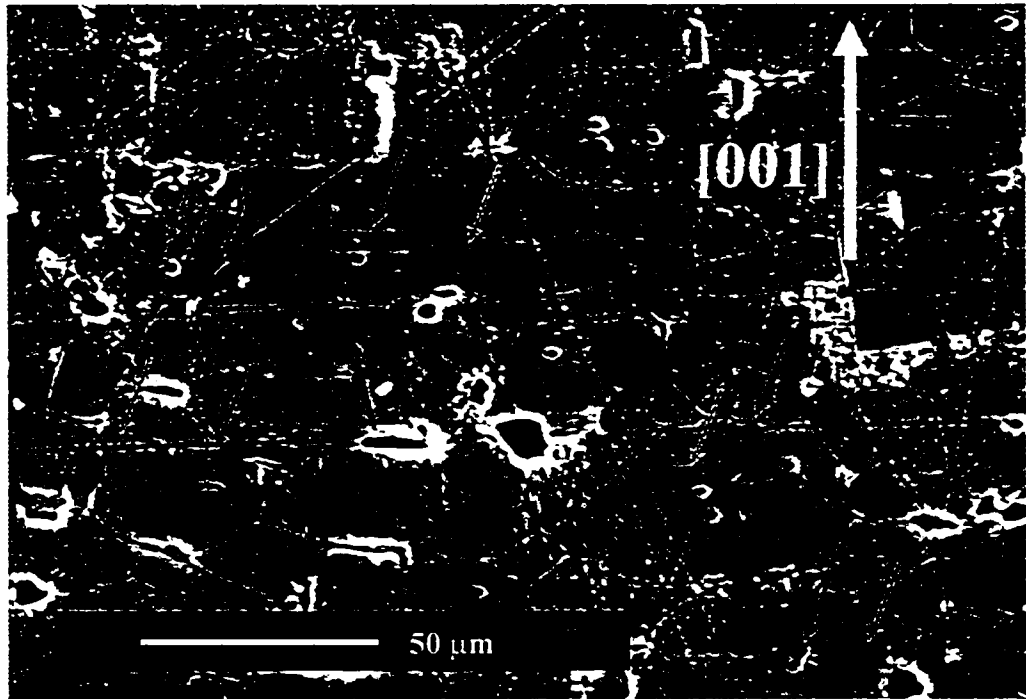


Figure 5.7. Edge view SEM image of textured $\text{Na}_{1/2}\text{Bi}_{1/2}\text{TiO}_3\text{-BaTiO}_3$. Rectangular grains are oriented in the [001] direction. Dark gray areas are SrTiO_3 template particles. Light gray areas are hetero-epitaxially grown $\text{Na}_{1/2}\text{Bi}_{1/2}\text{TiO}_3\text{-BaTiO}_3$ matrix phase. Those regions are marked by arrows.

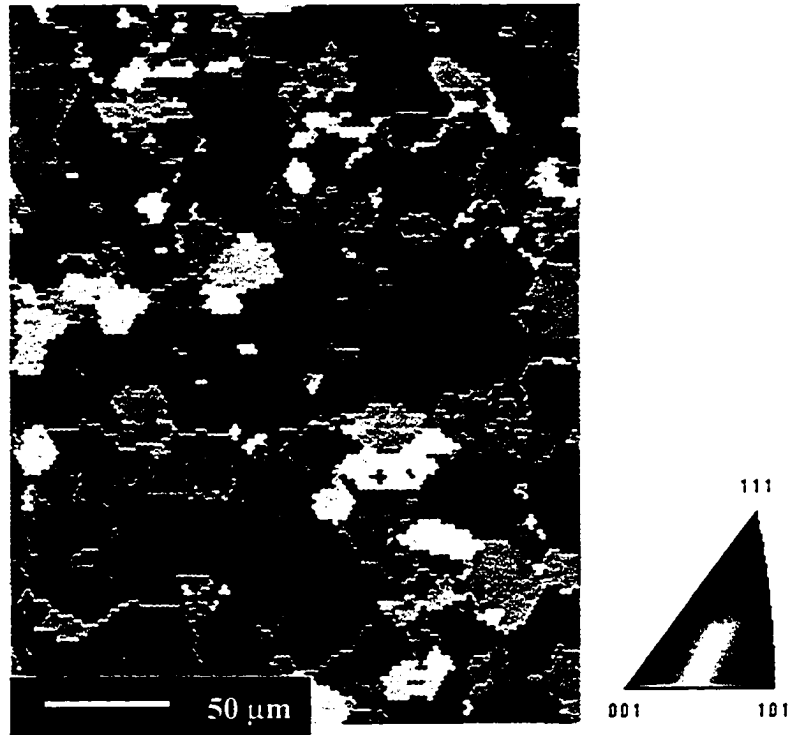


Figure 5.8. Color-coded crystal orientation map of textured $\text{Na}_{1/2}\text{Bi}_{1/2}\text{TiO}_3\text{-BaTiO}_3$.
Texture direction ($[001]$) is perpendicular to the plane.

Figure 5.9 shows the image quality map of a $[001]_{pc}$ textured $\text{Na}_{1/2}\text{Bi}_{1/2}\text{TiO}_3$ -5.5 mol% BaTiO_3 ceramic (textured using 5 vol% SrTiO_3 template particles) based on image quality of each data point. The texture direction is perpendicular to the plane. A schematic of one seeded grain is shown in Figure 5.10. A SrTiO_3 template grain is located at the center of each seeded grain. The $\text{Na}_{1/2}\text{Bi}_{1/2}\text{TiO}_3$ -5.5 mol% BaTiO_3 matrix phase is heteroepitaxially grown on the surface of the template particle resulting in large seeded grains. The seed and the grown material have the same orientation.

To further show the epitaxial growth of $\text{Na}_{1/2}\text{Bi}_{1/2}\text{TiO}_3$ -5.5 mol% BaTiO_3 on a SrTiO_3 template, a $[001]$ oriented SrTiO_3 single crystal was embedded in a $\text{Na}_{1/2}\text{Bi}_{1/2}\text{TiO}_3$ -5.5 mol% BaTiO_3 matrix powder and sintered in the same conditions. The image quality map was given in Figure 5.11. The white region on the left is the SrTiO_3 single crystal and the gray region on the right is the epitaxially grown matrix material. Randomly oriented grains are located at the lower section of the image. In Figure 5.12, a color coded orientation map of the same section is given. It should be noted that the SrTiO_3 template and epitaxially grown region were represented with the same color (light blue). The randomly oriented grains have various colors corresponding to different orientations. The misorientation in the epitaxially grown region is less than 5° .

Figure 5.13 shows the $[001]$, $[011]$, and $[111]$ pole figures of the same sample shown in Figures 5.8 and 5.9. Clustering of poles at the center of the $[001]$ pole figure (red color) confirms texture in that direction. Also, the clustering of points at a given radius from the center (red color), as is the case for $[011]$ and $[111]$ pole figures, confirms the presence of fiber texture. A similar sample characterized using x-ray rocking curve gave 80% texture with a FWHM of 8.5° .



Figure 5.9. Image quality map obtained using OIM shows the morphology of the grains. Light gray areas (marked by red arrows) at the center of large grains are the template particles.

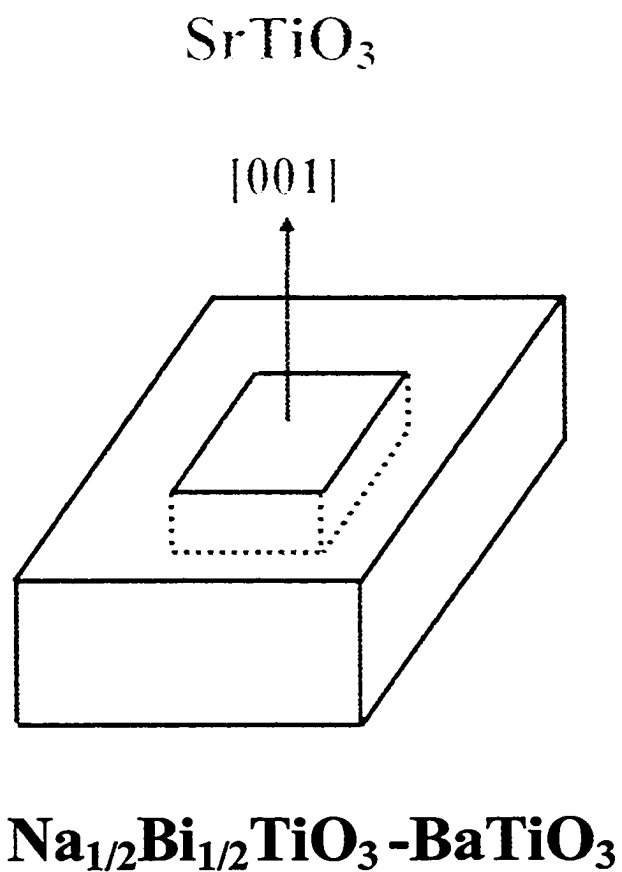


Figure 5.10. Schematic representing one SrTiO_3 templated $\text{Na}_{1/2}\text{Bi}_{1/2}\text{TiO}_3\text{-BaTiO}_3$ grain and its orientation in the SEM image.

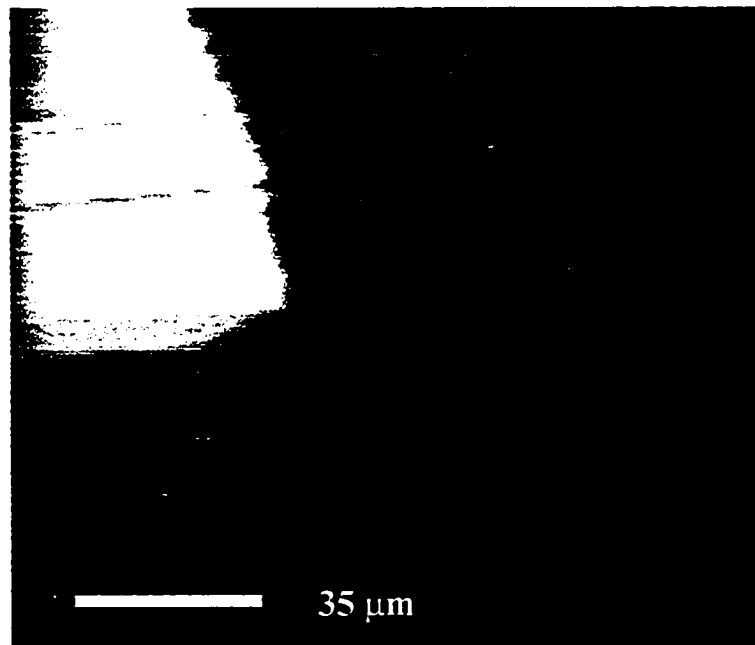


Figure 5.11. Image quality map of SrTiO₃ single crystal templated Na_{1/2}Bi_{1/2}TiO₃-5.5 mol % BaTiO₃ samples.

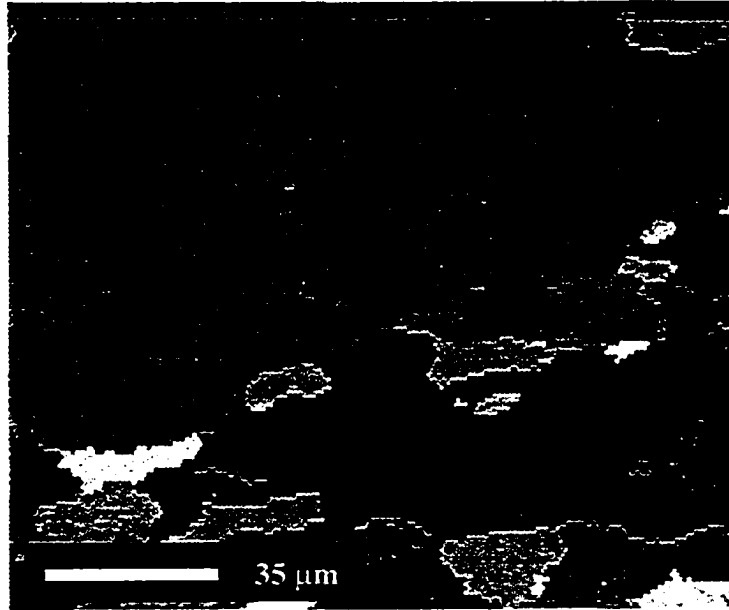


Figure 5.12. Color coded orientation map of SrTiO₃ single crystal templated Na_{1/2}Bi_{1/2}TiO₃-5.5 mol % BaTiO₃ samples.

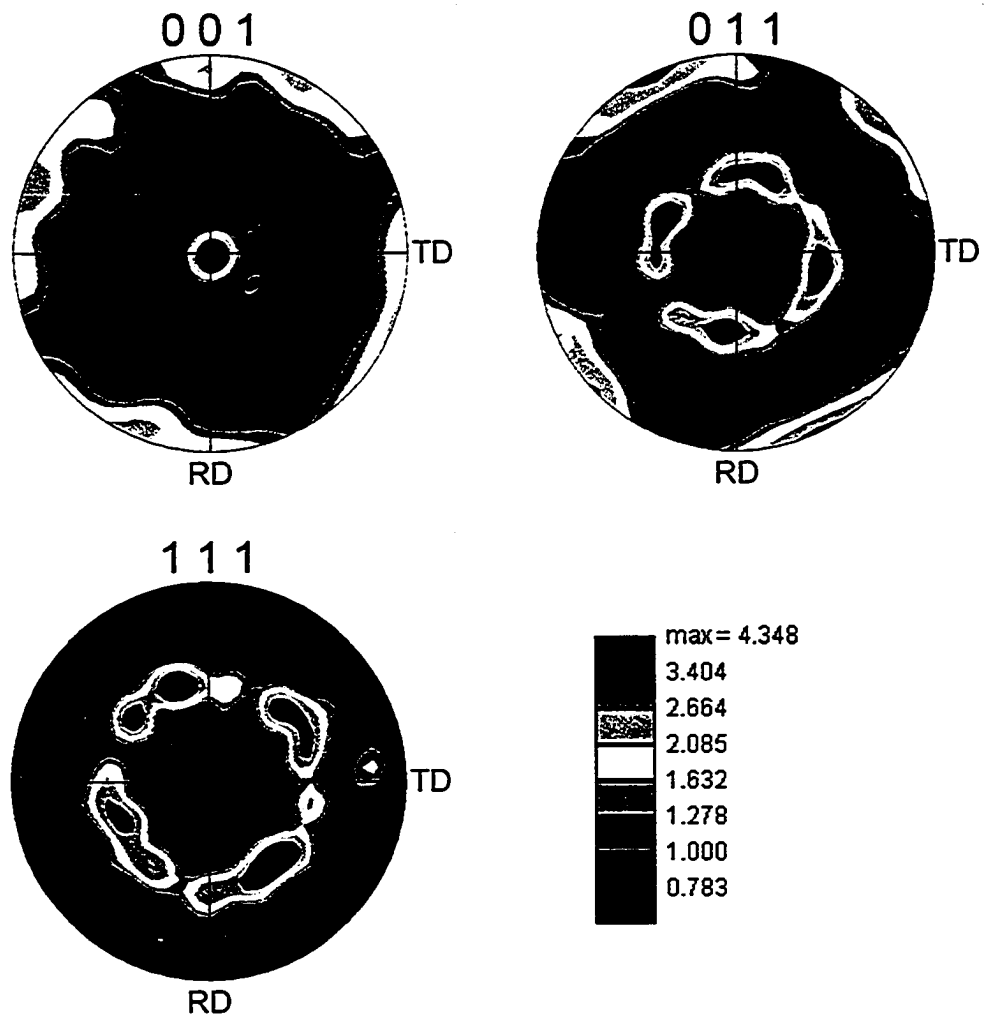


Figure 5.13. OIM derived $[001]$, $[011]$ and $[111]$ pole figures. The clustering of poles at the center of $[001]$ pole figure confirms texture in that direction.

Figure 5.14 shows the ODF (Orientation Distribution Function). The angles labeled as ϕ_1 , ϕ and ϕ_2 are Euler angles (Bunge). In the case of Bunge's form of the Euler angles this is a rotation (ϕ_1) about the z_s axis followed by a rotation (ϕ) about the x' axis followed by a third rotation (ϕ_2) about the z_s axis again, Figure 5.15. The angles ϕ_1 and ϕ_2 range from 0 to 2π and ϕ ranges from 0 to π . These limits form a bounded space referred to as Euler space. The orientations were plotted in constant sections through orientation space. However, the axisymmetric region of Euler Space is much smaller when crystal symmetry and sample symmetry are taken into account [10]. It should be noted that the ODF is different than the plot of orientations in Euler space. If the orientations overlap, which is common in texture, it is difficult to see the degree of orientation. The second problem is the orientation space is non-linear, therefore, clustering of points in orientation space may be misleading [10]. A quantitative way of overcoming this problem and describing the texture statistically is the use of the ODF. Therefore, the ODF is represented as a color intensity map. The regions of high intensity (near the red end of the color scale) are associated with clustering of points in the discrete plot shown in Figure 5.14 [10]. The ODF (also represented as $f(g)$) is calculated by fitting the distribution of the discrete orientation data. This gives the probability density function describing the probability of finding a grain with an orientation g within a given distance in orientation space (Δg) of a specified orientation g_0 in a polycrystal, or alternatively the volume fraction of material oriented within Δg of g_0 [10].

$$\frac{\Delta V(g_0 + \Delta g)}{V} = \int_{g \in (g_0 + \Delta g)} f(g) dg \quad \text{Eqn. 5.1}$$

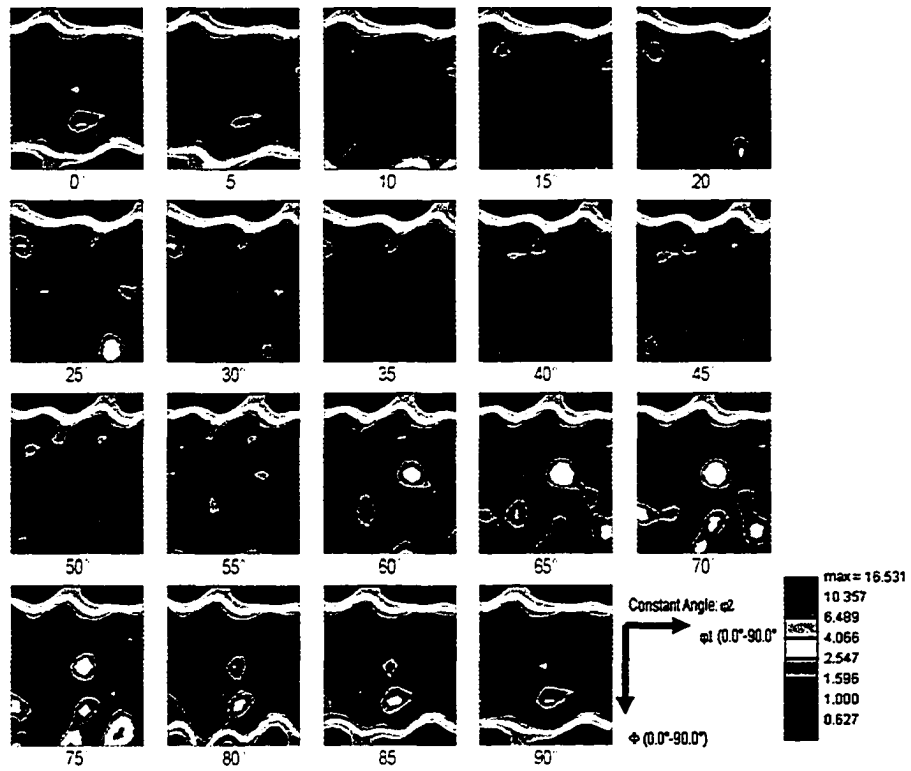


Figure 5.14. Orientation distribution function of textured $\text{Na}_{1/2}\text{Bi}_{1/2}\text{TiO}_3$ -5.5 mol % BaTiO_3 samples.

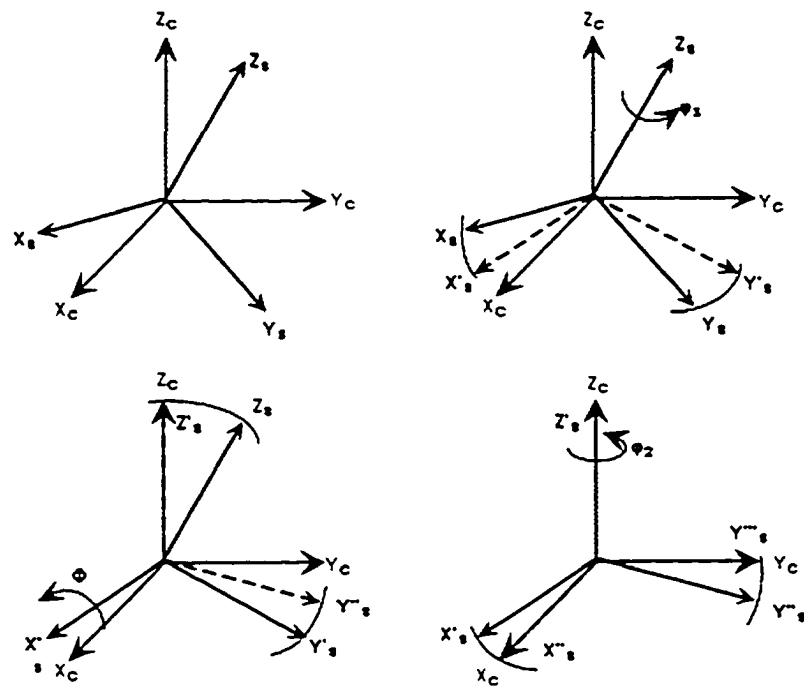


Figure 5.15. Schematic representation of Euler angles. From [10].

The expression for $f(g)$ must satisfy the following condition:

$$\int f(g)dg = 1 \quad \text{Eqn. 5.2}$$

It should be noted that one advantage of texture calculated by OIM data is that volume fractions of a given texture component can be determined quite accurately in a well defined manner compared to x-ray and neutron diffraction methods. For example, the volume fraction of material oriented within 15° of the orientation $(0^\circ, 0^\circ, 0^\circ)$ can be directly calculated by finding the number of orientation measurements in the OIM data set which satisfy this condition and dividing this number by the total number of measurements in the set. Data obtained from conventional x-ray or neutron diffraction pole figures cannot be directly interrogated. Pole figure methods require ODFs to be calculated from the pole figures and the volume fraction calculated from the ODFs by integration over an appropriate volume of the ODF and are thus dependent on the calculation method as well as the parameters used in the calculation [10].

In this study, texture was analyzed using x-ray diffraction and electron diffraction and the results were quantified using the Lotgering factor from the x-ray diffraction, and rocking curve were determined by both x-ray diffraction and electron diffraction for similar samples. The results are summarized in Table 5.1. The Lotgering factor is a semi-quantitative texture characterization method that does not give any information about orientation distribution. A texture fraction of $f=90\%$ was measured. The texture fraction for the same sample was $f=80\%$ with an orientation parameter of $r=0.20$ when measured using rocking curve. The texture fractions measured using rocking curve were relatively lower than the texture fractions obtained using Lotgering factor. The texture fraction

Table 5.1. Comparison of different texture quantification methods of textured $\text{Na}_{1/2}\text{Bi}_{1/2}\text{TiO}_3$ -5.5 mol % BaTiO_3 samples.

		X-ray	OIM
Lotgering Factor	Texture Fraction	90%	-
	Texture Fraction	80%	94%
Rocking Curve	FWHM	8.5°	9°
	Orientation Parameter	0.20	0.21

obtained from X-ray based rocking curve and electron diffraction based rocking curve 80% and 94%, respectively. A relatively close orientation parameter 0.20 and 0.21, and FWHM 8° and 9°, respectively were obtained for similar samples. Even though the correlation between orientation parameters from March-Dollase function were in good agreement, the relatively high texture fraction obtained from OIM might be related to the number of grains from which orientation information was collected. Considering the high reproducibility of texture in SrTiO₃ templated systems, the result is not surprising. The measured pole density data from OIM and March-Dollase function were shown in Figure 5.16.

5.5 CONCLUSIONS

Orientation imaging microscopy (OIM) was used to characterize the random and oriented grains in Na_{1/2}Bi_{1/2}TiO₃-BaTiO₃ ceramics. In characterization of the sample, a vast amount of microstructural (grain size and distribution, grain morphology) and orientation information (texture fraction, texture distribution, orientation across grain boundaries, pole figures, rocking curves) was obtained.

Random ceramics did not show the presence of many special boundaries like {111} twins. Probably the grain growth mechanism is normal grain growth. Large (~30 μm) grained microstructure were obtained. Pole figures confirmed the random distribution of the grain orientations.

In a textured ceramic, large seeded grains (up to 50 μm) dominated the microstructure, surrounded by small randomly oriented grains. The orientations of the seeded grains were the same as the SrTiO₃ template particles. The matrix Na_{1/2}Bi_{1/2}TiO₃-

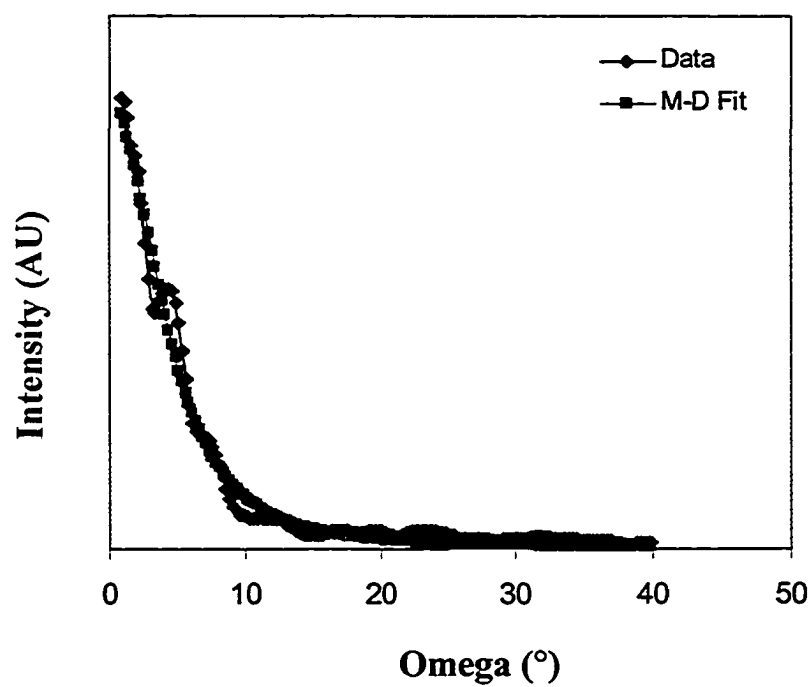


Figure 5.16. Measured pole density data from OIM and March-Dollase function for textured $\text{Na}_{1/2}\text{Bi}_{1/2}\text{TiO}_3$ -5.5 mol % BaTiO_3 samples.

BaTiO₃ phase nucleated and grew hetero-epitaxially on the template particles (it was not possible to distinguish the diffraction patterns of the SrTiO₃ template particles and Na_{1/2}Bi_{1/2}TiO₃-BaTiO₃ matrix phase surrounding it). Pole figures and rocking curves confirmed a narrow [001]_{pc} fiber texture distribution in the ceramics (FWHM=9°).

In this study x-ray-based and OIM-based texture characterization methods were used. Electron diffraction is a point sampling measurement technique, whereas x-ray diffraction is an area sampling technique. Therefore, x-ray diffraction is an average measurement technique. A complete texture description can be obtained using OIM. The calculated orientation distribution function is more reliable with OIM [25], which may become more critical in predicting the properties of the textured materials. It is also practical, because the sample needs to be characterized only one time to almost completely quantify the texture in the sample, including the microstructural features like grain size and morphological texture. Nevertheless, both texture characterization methods predicted similar FWHM, orientation parameter, and texture fractions.

5.6 REFERENCES

1. S. Kikuchi, "Diffraction of Cathode Rays by Mica," Jap. J. Phys., 5 pp.83-99 (1928).
2. M. N. Alam, M. Blackman, and D. W. Pashley, "High Angle Kikuchi Patterns," Proc. Royal Soc. London, A221 [1145] pp. 224-42 (1954).
3. D. G. Coates, "Kikuchi-like Reflection Patterns Observed in the Scanning Electron Microscope," Phil. Mag. 16 pp. 1179 (1967).
4. D. C. Joy, Electron Channeling Patterns in the SEM, in: Quantitative Scanning Electron Microscopy, Eds. D. Holt, M. D. Muir, P. R. Grant, I. M. Boswarva, Academic Press London, p. 31 (1974).
5. D. J. Dingley, The Development of Automated Diffraction in Scanning and Transmission Electron Microscopy, in Electron Backscatter Diffraction in Materials Science, Kluwer Academic/Plenum Publishers New York, NY, p. 1-18 (2000)
6. J. A Venables, and C. J. Harland, "Electron Backscatter Patterns – a New Crystallographic Technique for Use in the SEM," in Scanning Electron Microscopy: Systems and Applications, Institute of Physics, London and Bristol, p. 294 (1973).
7. J. A Venables, and C. J. Harland, "Electron Backscatter Patterns – a New Crystallographic Technique for Obtaining Crystallographic Information," in the Scanning Electron Microscope, Phil. Mag., 2 pp. 1193 (1973).
8. J. A Venables, A. Bin-Java, and C. J. Harland, Crystallographic Orientation Determination in the SEM Using Electron Backscattering Patterns and Channel

- Plates, in: *Developments in Electron Microscopy and Analysis*, Academic Press, London, p. 1014 (1973).
9. D. J. Dingley, "A Comparison of Diffraction Techniques for the SEM," *Scanning Electron Micro.*, 4 p. 273 (1981).
 10. S. Wright, and M. Nowell, *TSL Operators Training Manual*, October 23-25, 2001, Mahwah, NJ.
 11. J. Illingworth, and J. Kittler, "A Survey of the Hough Transform," *Computer Vision, Graphics and Image Processing*, 44 pp. 87-116. (1988).
 12. C. S. Barrett, and L. H. Levenson, "The Structure of Aluminum after Compression," *Tran. Am. Inst. Min. Eng.*, 137 pp. 112-127 (1940).
 13. C. S. Barrett, "The Structure of Iron after Compression," *Tran. Am. Inst. Min. Eng.*, 135 pp. 296-326 (1939)
 14. H. J. Bunge, *Texture Analysis in Materials Science*, Butterworths, London (1982).
 15. F. Haessner, J. Pospiech, and J. Sztwiertnia, "Spatial Arrangements of Orientations in Rolled Copper," *Mater. Sci. Eng.*, 57 [1] pp. 1-14 (1983).
 16. J. Hirsch, "Correlation of Deformation Texture and Microstructure," *Mater. Sci. Tech.*, 6 pp. 1048-57 (1990).
 17. F. J. Humphreys, "The Nucleation of Recrystallization at Second Phase Particles in Deformed Aluminum," *Acta Metal.*, 25 [11] pp.1323-44 (1977).
 18. M. T. Lyttle, and J. A. Wert, "Modeling of Continuous Recrystallization in Aluminum Alloys," *J. Mat. Sci.*, 29 [12] pp. 3342-50 (1994).

19. C. Duran, Fabrication and Electrical Properties of Textured $\text{Sr}_{0.53}\text{Ba}_{0.47}\text{Nb}_2\text{O}_6$ Ceramics Prepared by Templated Grain Growth. Ph.D. thesis, Penn State University (2001).
20. A. Khan, D. T. Carpenter, A. M. Scotch, and H. M. Chan, and M. P. Harmer, "Electron Backscatter Diffraction Analysis of $\text{Pb}(\text{Mg}_{1/3}\text{Nb}_{2/3})\text{O}_3$ -35mol% PbTiO_3 Single Crystals Grown by Seeded Polycrystal Conversion," *J. Mater. Res.*, **16** [3] pp. 694-700 (2001).
21. F. Ernst, M. L. Mulvihill, O. Kienzle, and M. Ruhle, "Preferred Grain Orientation Relationships in Sintered Perovskite Ceramics," *J. Am. Ceram. Soc.*, **84** [8] pp. 1885-90 (2001).
22. C.L. Jia, R. Rosenfeld, A. Thust, and K. Urban, "Atomic Structure of a $\Sigma=3$, {111} Twin-Boundary Junction in a BaTiO_3 Thin Film," *Philosophical Magazine Letters*, **79** [3] pp. 99-106 (1999).
23. R. A. Schwarzer "Preparation of High-Resistance or Sensitive Samples for Grain Orientation Measurement with Electron Microscopes," *Materials Science Forum*, **157-162** pp. 201-206 (1994).
24. D. J. Dingley, and V. Randle, "Microtexture Determination by Electron Backscatter Diffraction," *J. Mater. Sci.*, **27** [17] pp. 4545-66 (1992).
25. X. An, "A Comparison of Different Texture Analysis Techniques," *Proceedings of the Eleventh International Conference on Textures of Materials (ITOCOM-11)*, **1** pp. 53-62 (1996).

Chapter 6

**CALCULATION OF THE ELECTRICAL AND ELECTROMECHANICAL
PROPERTIES OF TEXTURED 3_m SYMMETRY (RHOMBOHEDRAL)
CERAMICS**

6.1 INTRODUCTION

Theoretical calculation of the macroscopic physical properties of polycrystalline materials from single crystal data is a very difficult task due to inherent complexity of the problem. Especially for polarized materials which exhibit piezoelectricity, the piezoelectric interactions between grains has to be taken into account to obtain more accurate property estimations [1]. One of the common approaches in doing the calculations is averaging any anisotropic physical property (polarization, dielectric, piezoelectric, etc.) over a representative space. This can be done by assuming a random grain (domain) orientation distribution for random ceramics. On the other hand, in order to calculate an average physical property for a textured ceramic, a function expressing the texture (orientation distribution) in the sample can be incorporated into the averaging equation prior to performing the calculations. The texture function can be measured by Lotgering factor, rocking curve, pole figure, orientation imaging microscopy etc.

The method of calculation in which grain interactions are taken into account is called Effective Medium Theory (EMT) [1]. In fact, EMT has been utilized in the calculation of the effective dielectric, piezoelectric, and elastic constants of polycrystalline ferroelectric materials especially with tetragonal (4_{mm}) symmetry [1].

However, most of the physical property calculations from single crystal data reported in the literature neglect grain-grain interactions [2].

Single crystals of rhombohedrally distorted perovskites exhibit high strains and, therefore, high piezoelectric constants along $[001]_{pc}$ due to the engineered domain state [3]. However, large and high quality single crystals are difficult to produce in large quantities. Therefore, there is interest in $[001]_{pc}$ textured rhombohedral ceramics. Well textured ceramics are expected to exhibit similar properties to single crystals, because the overall macroscopic property will be governed by the individual crystallites (grains, domains) whose orientations are distributed over space.

NBT-BT (BT<6.5 mol%) has rhombohedral symmetry therefore, it might be possible for this system to exhibit high strains in the $[001]_{pc}$. However, the complete polarization, dielectric, and piezoelectric tensors are not available for NBT-BT. Therefore, the properties of rhombohedral $PbZr_xTi_{1-x}O_3$ ferroelectric single domain-single crystals, whose properties (polarization, dielectric and piezoelectric) were computed using Landau-Ginsburg-Devonshire phenomenological theory, will be used in the calculations for random and textured cases [4]. The aim of this chapter is to estimate the macroscopic physical properties of random and textured ($[001]_{pc}$) rhombohedral perovskites by averaging single crystal data and to compare those values with the experimentally reported ones.

6.2 AVERAGING OF POLARIZATION

The polarization vector P_i' for a 3m symmetry ceramic is given by:

$$P_i' = \begin{bmatrix} 0 \\ 0 \\ P_3' \end{bmatrix} \quad \text{Eqn. 6.1}$$

where P_3' is $51 \mu\text{C}/\text{cm}^2$ for $\text{PbZr}_{0.52}\text{Ti}_{0.48}\text{O}_3$ on the rhombohedral side of the morphotropic phase boundary [4]. The symmetry does not allow a polarization component in the other principal axes directions [5]. The polarization direction is along $\langle 111 \rangle_{\text{pc}}$ in rhombohedral perovskites. To simplify the mathematics, instead of a rhombohedral lattice, a trigonal lattice was chosen in the calculations where the [111] direction in the rhombohedral lattice becomes the c-axis of the trigonal unit cell (Figure 6.1) [6]. An orthogonal coordinate system, x_1' , x_2' and x_3' , is defined so that x_1' ([100]) is equivalent to the a-axis and x_3' ([001]) is equivalent to the c-axis of the trigonal lattice. x_2' , which is the [010], is not in the same direction as the b-axis of the trigonal lattice. The polarization vector (P_i') given in Eqn. 6.1 is expressed in this orthogonal coordinate system whose axes are labeled as x_1' , x_2' and x_3' .

At this point, a new orthogonal coordinate system with principal axes labeled as x_1 , x_2 and x_3 (no prime) has to be defined. This new orthogonal coordinate system is defined so that the principal axes (x_1 , x_2 and x_3) are equivalent to the major pseudo-cubic axes of the cubic perovskite crystal structure (Figure 6.2) [7], that is x_1 is equivalent to [100], x_2 is equivalent to [010], and x_3 is equivalent to [001]. x_1' , x_2' and x_3' and x_1 , x_2 and x_3 are the principal axes in trigonal and cubic crystal lattices, respectively, as shown

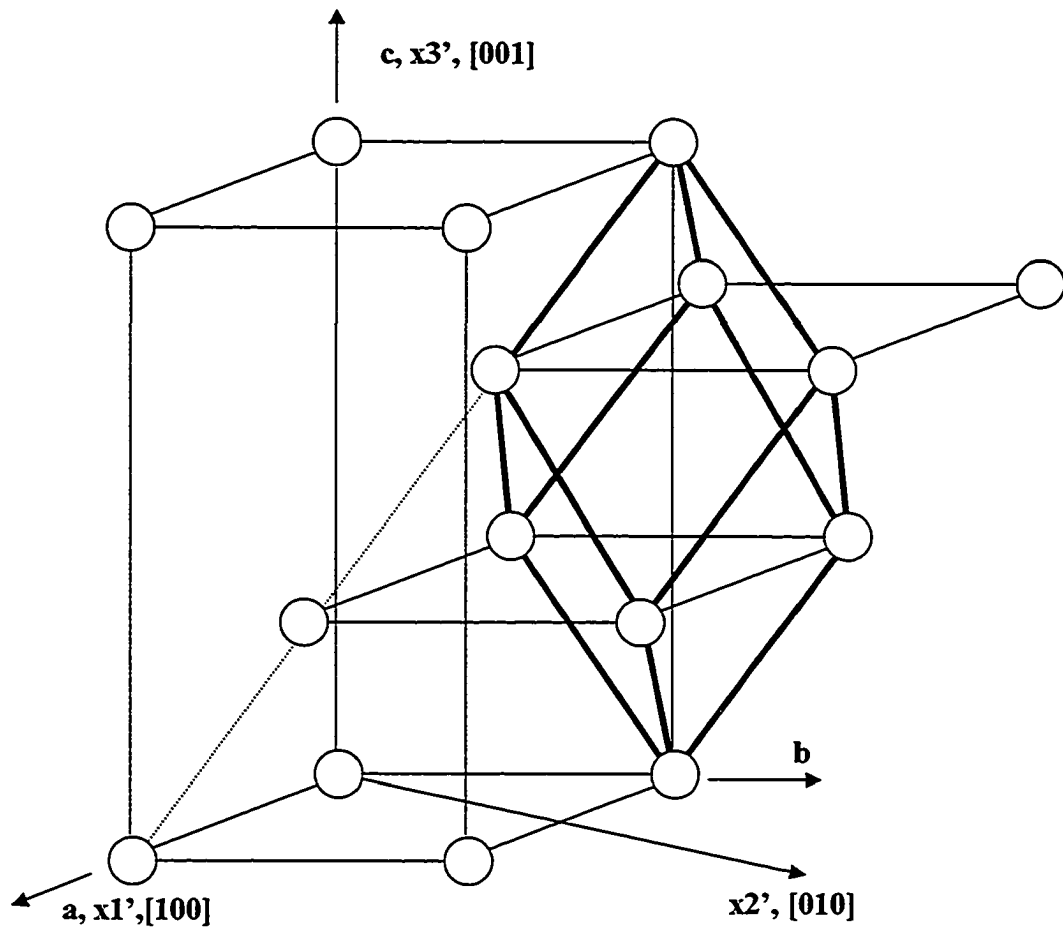


Figure 6.1. The relationship between the trigonal unit cell and the rhombohedral (pseudocubic) unit cell illustrated [6].

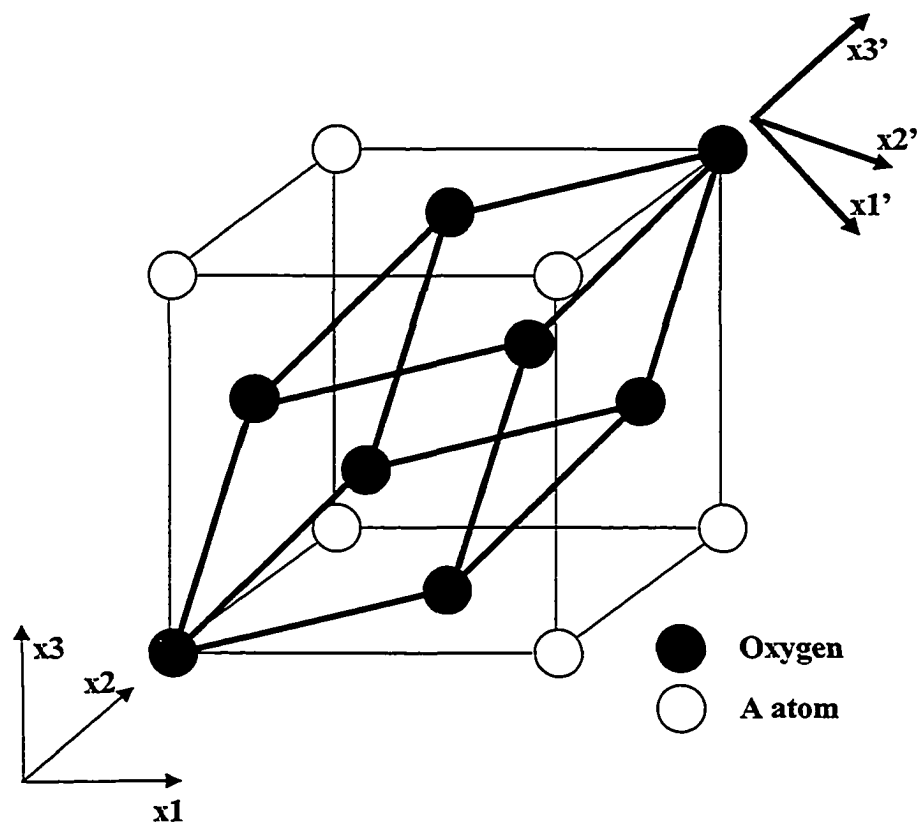


Figure 6.2. The relationship between the two coordinate systems in terms of the (pseudo) cubic unit cell.

in Figures 6.1 and 6.2. The need for the definition of two different coordinate systems is that any property of the crystal (polarization, dielectric and piezoelectric) has to be expressed in the new coordinate system (no prime) so that they are in the same coordinate system as the texture function. If the polarization vector, given in Eqn. 6.1, is expressed in this new orthogonal coordinate system, then the average value of polarization can be calculated by just measuring the angular deviation of the x_3 axis of the pseudo-cubic perovskite from sample normal (measurement direction).

The transformation of polarization vector from the old to new coordinate system is expressed as:

$$P_i = a_{ij}P'_j \quad \text{Eqn. 6.2}$$

where a_{ij} is the directional cosine matrix that relates the two coordinate systems mentioned above. In order to calculate the a_{ij} matrix, the equivalent directions of the x_1' , x_2' and x_3' axes has to be expressed in the new orthogonal coordinate system relative to the x_1 , x_2 and x_3 axes. The components of the directional cosines are given in Table 6.1, where α is the angle between the directions given in the second and third column. These directions are all expressed in the new coordinate system.

After the transformation the polarization vector will be:

$$P_i = \begin{bmatrix} P_1 \\ P_2 \\ P_3 \end{bmatrix} \quad \text{Eqn. 6.3}$$

where $P_1=P_2=P_3=P_3' \text{Cos}(54.7^\circ)$. The polarization is along $[111]_{pc}$ and the angle between any of the principal axes ($[100]_{pc}$, $[010]_{pc}$, $[001]_{pc}$) is 54.7° . The polarization in any direction denoted as $1'$ in Figure 6.3 can be calculated using Eqn. 6.4.

Table 6.1. Axes relations in the old and new coordinate system. All directions given in cubic axes.

	New axes	Equivalent old axes	Cos(α)
a_{11}	$[100]=x_1$	$[0-11]=x_1'$	0
a_{12}	$[100]=x_1$	$[2-1-1]=x_2'$	$2/\sqrt{6}$
a_{13}	$[100]=x_1$	$[111]=x_3'$	$1/\sqrt{3}$
a_{21}	$[010]=x_2$	$[0-11]=x_1'$	$-1/\sqrt{2}$
a_{22}	$[010]=x_2$	$[2-1-1]=x_2'$	$-1/\sqrt{6}$
a_{23}	$[010]=x_2$	$[111]=x_3'$	$1/\sqrt{3}$
a_{31}	$[001]=x_3$	$[0-11]=x_1'$	$1/\sqrt{2}$
a_{32}	$[001]=x_3$	$[2-1-1]=x_2'$	$1/\sqrt{6}$
a_{33}	$[001]=x_3$	$[111]=x_3'$	$1/\sqrt{3}$

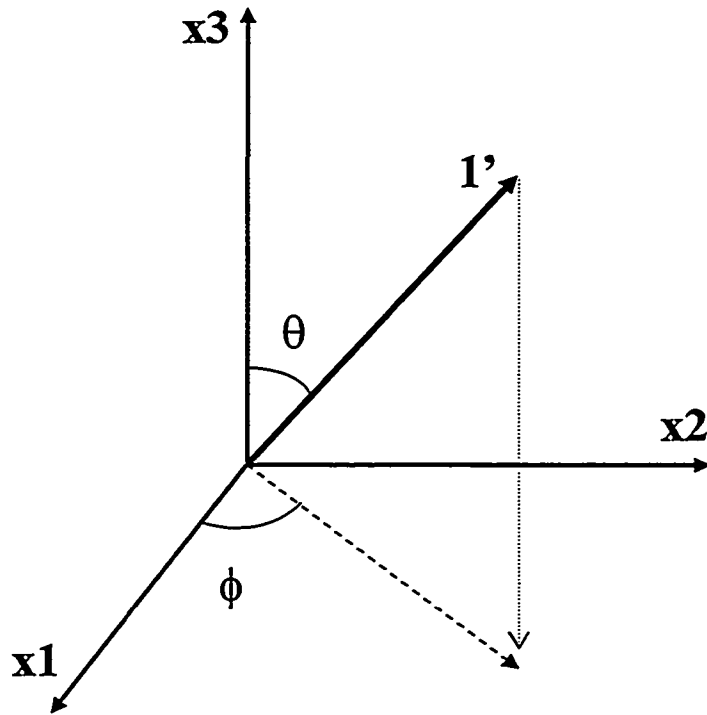


Figure 6.3. Definition of the angles to express directions in orthogonal coordinate system with axes labeled as x_1 , x_2 , and x_3 .

$$P_3(\theta, \phi) = P_3[\text{Sin}(\theta)\text{Cos}(\phi) + \text{Sin}(\theta)\text{Sin}(\phi) + \text{Cos}(\theta)] \quad \text{Eqn. 6.4}$$

where θ is the angle between the $1'$ direction and x_3 axes, whereas ϕ is the angle between the x_1 axis and the direction of the projection of the $1'$ onto the x_1 - x_2 plane, Figure 6.3.

There are 8 equivalent polarization directions ($\langle 111 \rangle_{pc}$) in a rhombohedrally distorted perovskite crystal [3]. If an electric field is applied along any of the $\langle 111 \rangle_{pc}$, then ideally all polarization will switch to that direction and the material will become a single domain. In Figure 6.4, the direction dependence of the net polarization is shown for the case of single domain rhombohedral single crystal, which is the plot of Eqn. 6.4 in the $0^\circ \leq \theta \leq 90^\circ$ and $0^\circ \leq \phi \leq 90^\circ$ angular ranges. At all other angles, the polarization will switch to another equivalent $\langle 111 \rangle_{pc}$ giving the same values of polarization.

Up to this point all the calculations were performed on single crystals. In order to calculate the polarization in a polycrystalline ceramic with $3m$ symmetry crystallites, the following assumptions have to be made: with the applications of the electric field (poling field) the polarization will switch to one of the 8 possible $\langle 111 \rangle_{pc}$ so that the one which makes the smallest angle with the electric field is going to be the favorable one. Then, each grain will be a single domain with the polarization direction closest to the poling field direction (the angle is labeled as θ). This is clearly an oversimplification as it ignores elastic incompatibilities, but it does allow calculation of all the properties. Under this assumption, all possible polarization directions will fall into a cone and the apex angle of the cone is set by the maximum angle ($2 \times \theta_{max}$) that the polarization direction will make with the poling field, which is $\theta_{max} = 54.7^\circ$ when $[001]_{pc}$ of the crystallite

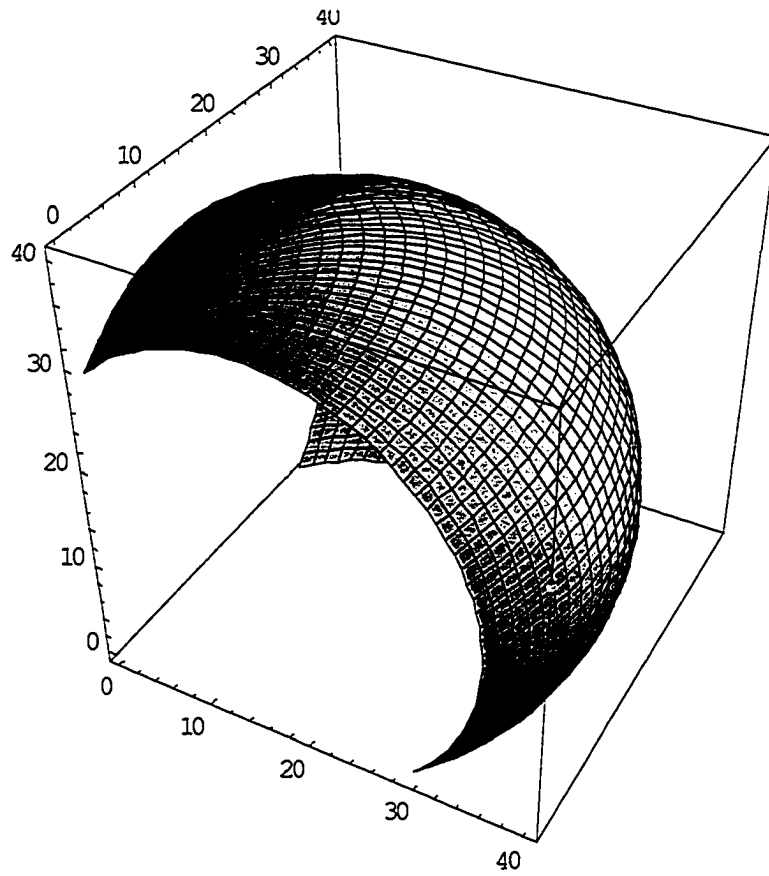


Figure 6.4. Directional dependence of polarization function (P_3) in spherical coordinate system.

(grain) is in the field direction. Any angle greater than 54.7° is not possible because another possible $\langle 111 \rangle_{pc}$ will be favored in order to reduce the angle between the field and P_3 . So, the angular range that θ can take ranges from 0° to 54.7° . The angular range for ϕ is 0° to 90° . Since the portion of angular space marked by the angles $0^\circ \leq \theta \leq 54.7^\circ$ and $0^\circ \leq \phi \leq 90^\circ$ encompasses the possible polarization direction distribution in a real sample, by averaging the orientation dependent polarization function (Eqn. 6.4) in that portion of the space for random and non-random situations, an average value for the polarization can be calculated for random and textured samples, respectively.

The polarization can be calculated by integrating over the orientation sphere allowing for the distribution of polar axes and averaging over all the crystallites (domains) [8]. The equation for the random ceramic case is given by [8]:

$$\langle P_3 \rangle_{\text{random}} = \frac{\int_{\theta=0^\circ}^{54.7^\circ} \int_{\phi=0^\circ}^{90^\circ} P_3(\theta, \phi) \sin\theta d\theta d\phi}{\int_{\theta=0^\circ}^{54.7^\circ} \int_{\phi=0^\circ}^{90^\circ} \sin\theta d\theta d\phi} \quad \text{Eqn. 6.5}$$

where $\langle P_3 \rangle_{\text{random}}$ stands for the average value of polarization for the random ceramic. If the calculation was performed using Eqn. 6.5 with $P_3 = 29 \mu\text{C}/\text{cm}^2$ (in the $[001]_{pc}$) for rhombohedral PZT [4] an average remanent polarization of $45 \mu\text{C}/\text{cm}^2$ was obtained for random ceramics. The calculated value of average polarization is 87 % of the single crystal polarization value in the $[111]_{pc}$ ($51 \mu\text{C}/\text{cm}^2$), which is consistent with the percentage reported in the literature [9]. The average value of remanent polarization of a polycrystal form this family is larger than the remanent polarization of the single crystal measured in the $[001]_{pc}$.

In order to calculate an average value of polarization for a textured ceramic, a texture function has to be incorporated into Eqn. 6.5. In this study, a March-Dollase [10] function is used.

$$F(f, r, \theta) = f \left(r^2 \cos^2 \theta + \frac{\sin^2 \theta}{r} \right)^{\frac{3}{2}} + (1-f) \quad \text{Eqn. 6.6}$$

where θ is the angle between the texture (orientation) axis and the scattering vector, r is the degree of orientation, and f is the volume fraction of oriented material. The r parameter characterizes the width of the texture (orientation) distribution. $r=1$ for a random sample and for a perfectly textured sample of tabular grains $r=0$. The equation for textured ceramic case is then given by

$$\langle P_3 \rangle_{\text{textured}} = \frac{\int_{\theta=0^\circ}^{54.7^\circ} \int_{\phi=0^\circ}^{90^\circ} P_3(\theta, \phi) F(f, r, \theta) \sin \theta d\theta d\phi}{\int_{\theta=0^\circ}^{54.7^\circ} \int_{\phi=0^\circ}^{90^\circ} F(f, r, \theta) \sin \theta d\theta d\phi} \quad \text{Eqn. 6.7}$$

where $\langle P_3 \rangle_{\text{textured}}$ stands for the average polarization for the textured ceramic. Before proceeding with the calculations, values for f and r in the March-Dollase function have to be assigned. Typical values of f and r for a reasonably well textured ceramic would be 0.8 (80%) and 0.2 respectively. The calculation performed using Eqn. 6.7 would yield an average polarization of $37 \mu\text{C}/\text{cm}^2$ for textured ceramic which is 72% of the single crystal polarization value in the $[111]_{\text{pc}}$.

A comparison of the average calculated polarization for random and textured ceramics reveals that $[001]_{\text{pc}}$ textured 3m symmetry ceramic has a lower polarization in the texture direction than a random ceramic, but is still bigger than single crystals

polarization measured in the same direction. This can be understood if the distribution of the polar $[111]_{pc}$ relative to the measurement direction is taken into account. In a $[001]_{pc}$ textured ceramic, the polar $[111]_{pc}$ is distributed mainly $\sim 54.7^\circ$ degrees away from the measurement direction. However, for a random ceramic, the distribution is even at all possible angles, therefore the polarization contribution from grains (domains) whose polar $[111]_{pc}$ axis is more closely parallel to the measurement direction is dominant. In Figure 6.5, the averaged remanent polarization in a rhombohedral PZT (52/48) as a function of texture fraction in March-Dollase [10] function is plotted, taking the r parameter as constant (0.2). This calculation gives the maximum available polarization.

6.3 AVERAGING OF DIELECTRIC CONSTANT

The dielectric constant tensor ϵ_{ij}' for a 3m symmetry ceramic is given by:

$$\epsilon_{ij}' = \begin{bmatrix} \epsilon_{11}' & 0 & 0 \\ 0 & \epsilon_{11}' & 0 \\ 0 & 0 & \epsilon_{33}' \end{bmatrix} \quad \text{Eqn. 6.8}$$

where ϵ_{11}' and ϵ_{33}' are 1233 and 475 for PZT (52/48), respectively [4]. The symmetry allows only three non-zero dielectric constants, two of which are independent [5]. The relationship between the cubic unit cell and the trigonal unit cell illustrated in Figures 6.1 and 6.2 is also used in the coordinate transformation of the dielectric tensor. If the dielectric tensor, given in Eqn. 6.8, is expressed in this new orthogonal coordinate system, then the average value of dielectric constant can be calculated by measuring the

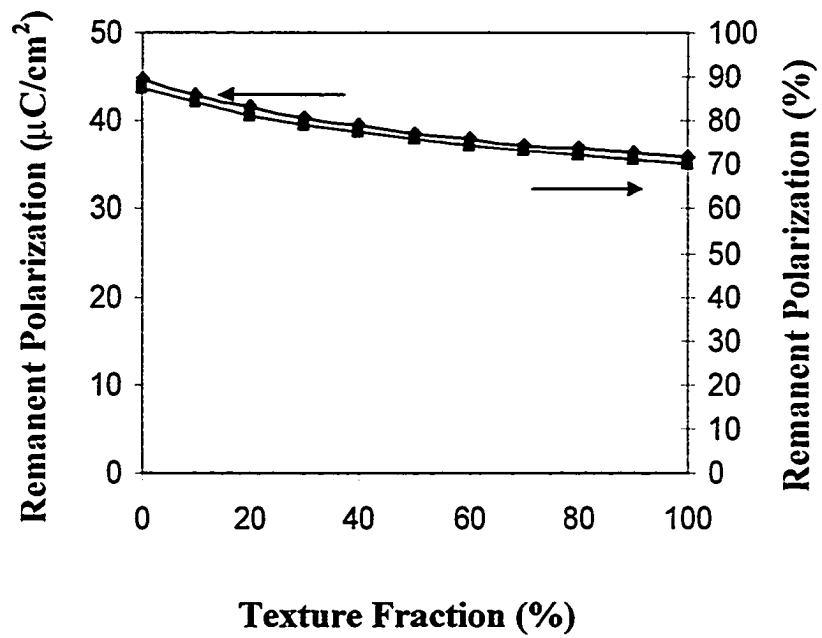


Figure 6.5. Calculated remanent polarization (also expressed in % of P_s) as a function of texture fraction in rhombohedral PZT (52/48).

angular deviation of the x_3 axis of the pseudo-cubic perovskite from the sample normal (measurement direction).

The dielectric tensor, ϵ_{ij} , in the new orthogonal coordinate system is calculated as:

$$\epsilon_{ij} = a_{ik} a_{jl} \epsilon_{kl} \quad \text{Eqn. 6.9}$$

where a_{ik} and a_{jl} are the directional cosines that relate the two coordinate systems mentioned above. The directional cosines matrix is given in Table 6.1.

After the transformation, the dielectric constant in any direction denoted as $1'$ can be expressed using Eqn. 6.10.

$$\epsilon_{33}(\theta, \phi) = \frac{1}{3} [2941 \cos^2(\theta) - 1516 \cos(\theta) \cos(\phi) \sin(\theta) + 2941 \cos^2(\phi) \sin^2(\theta) - 1516 \cos(\theta) \sin(\theta) \sin(\phi) - 1516 \cos(\phi) \sin^2(\theta) \sin(\phi) + 2941 \sin^2(\theta) \sin^2(\phi)] \quad \text{Eqn. 6.10}$$

where θ is the angle between the $1'$ direction and x_3 axes, whereas ϕ is the angle between x_1 axes and the direction of the projection of the $1'$ onto the x_1 - x_2 plane, Figure 6.3. Figure 6.6 is the plot of Eqn. 6.10. The maximum dielectric constant direction is the direction that is perpendicular to the polarization direction.

Up to this point all the calculations were performed on single crystals. In order to calculate the dielectric constant of a polycrystal ceramic with $3m$ symmetry the same assumptions about domain switching with the poling field mentioned in the previous section was made to set the angular boundaries for the averaging. So, the angular range that θ can take ranges from 0° to 54.7° . The angular range for ϕ is 0° to 90° . Since the portion of the angular space marked by the angles $0^\circ \leq \theta \leq 54.7^\circ$ and $0^\circ \leq \phi \leq 90^\circ$ is the only possible range of $[001]_{pc}$ direction distribution in a real sample, by averaging of

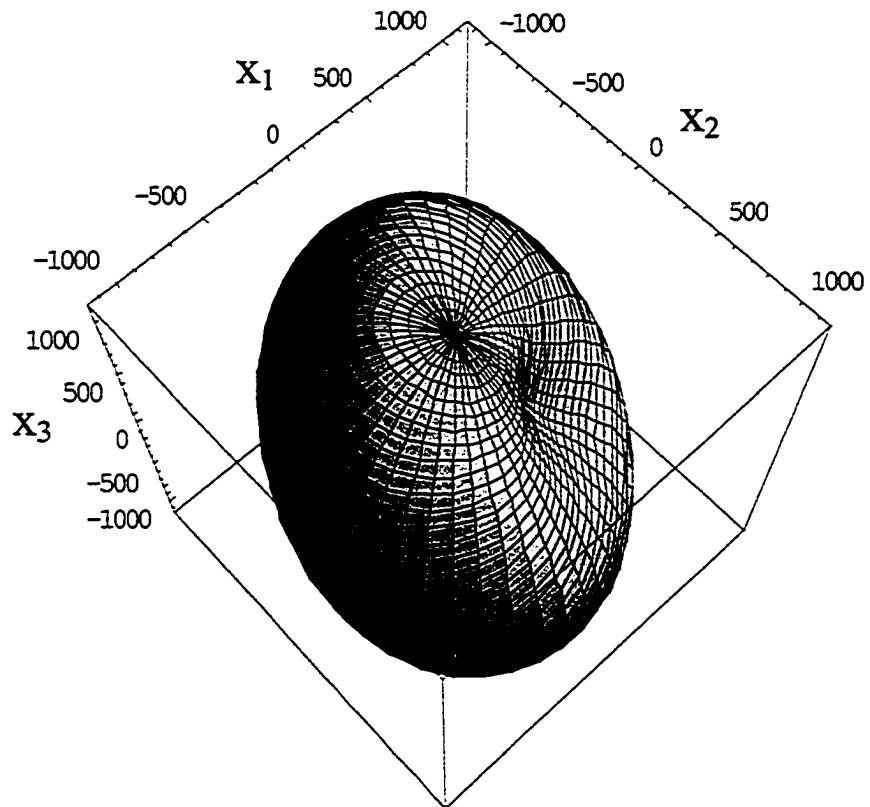


Figure 6.6. Directional dependence of dielectric function (ϵ_{33}) in spherical coordinate system.

orientation dependent dielectric function (Eqn. 6.10) in that portion of the space for random and non-random situation, an average value for the dielectric constant can be calculated for random and textured samples, respectively. This calculation does not account either for partial clamping of the dielectric constant or for domain wall contributions.

The dielectric constant can be calculated by integrating over the orientation sphere with allowance for the distribution of polar axes and averaging over all the crystallites (domains) [8]. The equation for the random ceramic is given by [8]:

$$\langle \epsilon_{33} \rangle_{\text{random}} = \frac{\int_{\theta=0^{\circ}}^{54.7^{\circ}} \int_{\phi=0^{\circ}}^{90^{\circ}} \epsilon_{33}(\theta, \phi) \sin\theta d\theta d\phi}{\int_{\theta=0^{\circ}}^{54.7^{\circ}} \int_{\phi=0^{\circ}}^{90^{\circ}} \sin\theta d\theta d\phi} \quad \text{Eqn. 6.11}$$

where $\langle \epsilon_{33} \rangle_{\text{random}}$ stands for the average value of dielectric constant for the random ceramic. If the calculation is performed using Eqn. 6.10, an average room temperature dielectric constant of 646 was obtained for random ceramics with 3m symmetry. The calculated average dielectric constant is 66% of the single crystal dielectric constant value in the $[001]_{\text{pc}}$. The average dielectric constant of a polycrystal is larger than the dielectric constant of the single crystal measured in the $[111]_{\text{pc}}$ (36%).

In order to calculate an average value of dielectric constant for textured ceramic a texture function has to be incorporated into Eqn. 6.11 as explained in the previous section, using the March-Dollase [10] function.

The equation for textured ceramic case is then given by:

$$\langle \epsilon_{33} \rangle_{\text{textured}} = \frac{\int_{\theta=0^{\circ}}^{54.7^{\circ}} \int_{\phi=0^{\circ}}^{90^{\circ}} \epsilon_{33}(\theta, \phi) F(f, r, \theta) \sin\theta d\theta d\phi}{\int_{\theta=0^{\circ}}^{54.7^{\circ}} \int_{\phi=0^{\circ}}^{90^{\circ}} F(f, r, \theta) \sin\theta d\theta d\phi} \quad \text{Eqn. 6.12}$$

where $\langle \epsilon_{33} \rangle_{\text{textured}}$ stands for an average value of dielectric constant for the textured ceramic. Before proceeding with the calculations, values for f and r in the March-Dollase function have to be assigned. Typical values of f and r for a reasonably well textured ceramic would be 0.8 (80%) and 0.2 respectively. The calculation performed using Eqn. 6.12 would yield an average dielectric constant of 829 for textured ceramic, which is 85% of the single crystal dielectric constant value in the $[001]_{\text{pc}}$. The average dielectric constant of a textured ceramic is larger than the dielectric constant of the single crystal measured in the $[111]_{\text{pc}}$ (75%).

A comparison of the average calculated dielectric constant for random and textured ceramics reveals that $[001]_{\text{pc}}$ textured 3m symmetry ceramic has a higher dielectric constant in the texture direction than a random ceramic, but is still lower than a single crystal dielectric constant measured in the same direction. This can be understood if the distribution of the polar $[111]_{\text{pc}}$ relative to the measurement direction is taken into account, keeping in mind that the maximum value of dielectric constant is perpendicular to the polarization direction. In a $[001]_{\text{pc}}$ textured ceramic, the polar $[111]_{\text{pc}}$ is distributed mainly about 54.7° degrees away from the measurement direction, however, for a random ceramic the distribution is even at all possible angles, therefore the contribution to the dielectric constant from grains (domains) whose polar $[111]_{\text{pc}}$ axis is pointing away (54.7°) from measurement direction is dominant as in the case of $[001]_{\text{pc}}$ textured

ceramics. In Figure 6.7, the averaged room temperature dielectric constant in a rhombohedral PZT (52/48) as a function of texture fraction in March-Dollase [10] function is plotted, taking the r parameter as constant (0.2).

6.4 AVERAGING OF PIEZOELECTRIC COEFFICIENT

The piezoelectric constant tensor d_{ij}' (two suffix notation) for a 3m symmetry ceramic is given by:

$$d_{ij}' = \begin{bmatrix} 0 & 0 & 0 & 0 & 1182 & -642 \\ -321 & 321 & 0 & 1182 & 0 & 0 \\ 7 & 7 & -3 & 0 & 0 & 0 \end{bmatrix} \text{ (pC/N)} \quad \text{Eqn. 6.13}$$

for a PZT (52/48) [4] ceramic expressed in the 3m coordinate system. The symmetry allows only eight non-zero piezoelectric coefficients, four of which are independent [5]. The relationship between the cubic unit cell and the trigonal unit cell illustrated in Figures 6.1 and 6.2 was used in the coordinate transformation of the piezoelectric constant tensor. If the piezoelectric constant tensor given in Eqn. 6.13 is expressed in this new cubic coordinate system, then the average value of piezoelectric constant can be calculated by just measuring the angular deviation of the x_3 axis of the pseudo-cubic perovskite from the sample normal (measurement direction).

The piezoelectric tensor, d_{ij} , in the new orthogonal coordinate system is calculated as:

$$d_{ij} = a_{il} d_{lm}' \alpha_{matrix} \quad \text{Eqn. 6.14}$$

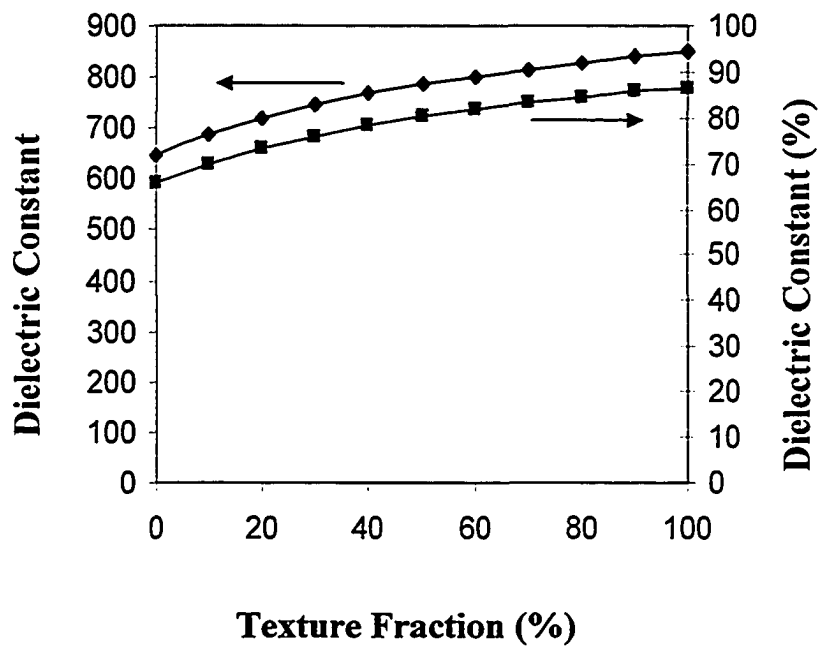


Figure 6.7. Calculated room temperature dielectric constant (also expressed in % of ϵ_{33}) as a function of texture fraction in rhombohedral PZT (52/48).

where a_{ij} are the directional cosines that relate the two coordinate systems mentioned above, whose components are given in Table 6.1. α_{matrix} is derived from the directional cosine matrix in order to transform a third rank tensor with two suffix notation [5].

After the transformation, the piezoelectric coefficient (d_{33} , two suffix notation, pC/N) in any direction denoted as $1'$ can be expressed using Eqn. 6.15.

$$\begin{aligned}
 d_{33}(\theta, \phi) = & 63\mathcal{C}\cos^3(\theta) - 264\cos^2(\theta)\cos(\phi)\sin(\theta) - 264\cos(\theta)\cos^2(\phi)\sin^2(\theta) \\
 & + 63\mathcal{C}\cos^3(\phi)\sin^3(\theta) - 264\cos^2(\theta)\sin(\theta)\cos(\phi) - 32\mathcal{C}\cos(\theta)\cos(\phi)\sin^2(\theta)\sin(\phi) \\
 & - 264\cos^2(\phi)\sin^3(\theta)\sin(\phi) - 264\cos(\theta)\sin^2(\theta)\sin^2(\phi) - 264\cos(\phi)\sin^3(\theta)\sin^2(\phi) \\
 & + 63\mathcal{S}\sin^3(\theta)\sin^3(\phi)
 \end{aligned}
 \tag{Eqn. 6.15}$$

where θ is the angle between the $1'$ direction and x_3 axis, whereas ϕ is the angle between the x_1 axis and the projection of $1'$ onto the x_1 - x_2 plane, Figure 6.3. Figure 6.8 is the plot of Eqn. 6.15.

Up to this point all the calculations were performed on single crystals. In order to calculate the piezoelectric coefficient of a polycrystal ceramic with 3m symmetry the same assumptions about domain switching with the poling field mentioned in the previous section were made to set the angular bounds for the averaging. So, the angular range that θ can take is from 0° to 54.7° . The angular range for ϕ is 0° to 90° . Since, the angular space bounded by the angles $0^\circ \leq \theta \leq 54.7^\circ$ and $0^\circ \leq \phi \leq 90^\circ$ covers the possible $[111]_{\text{pc}}$ direction distribution in a real sample, by averaging the orientation dependent piezoelectric function (Eqn. 6.15) in that portion of the space for random and non-random situation, an average value for the piezoelectric can be calculated for random and textured samples, respectively.

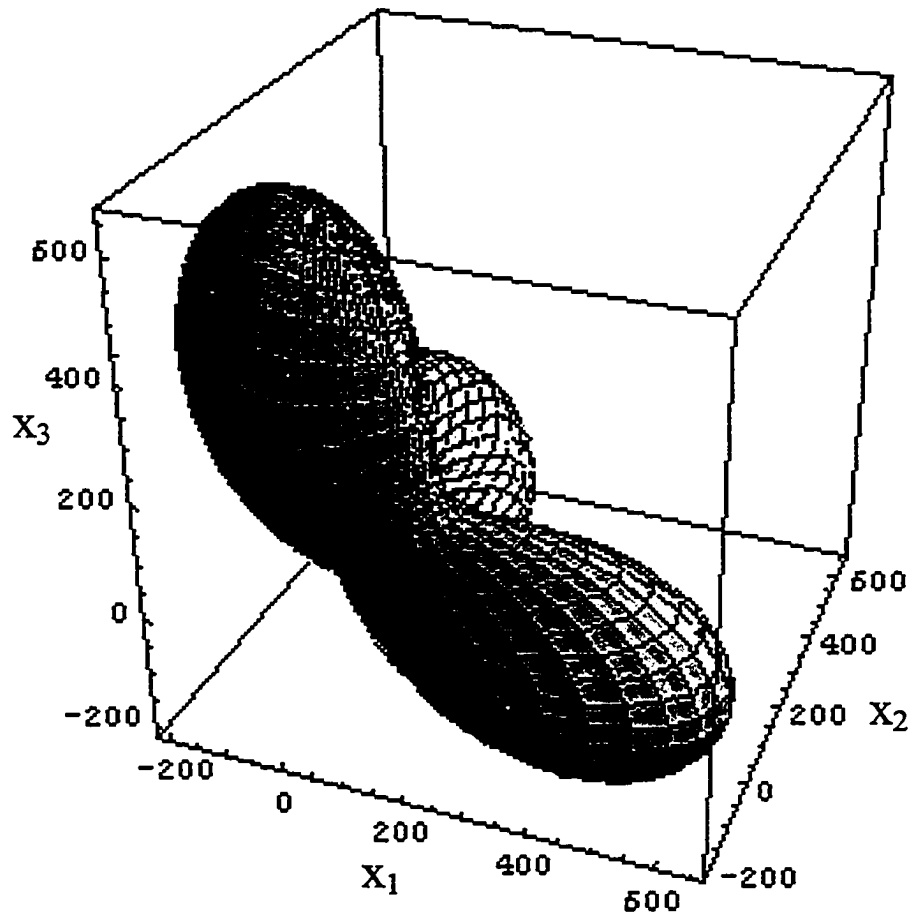


Figure 6.8. Directional dependence of piezoelectric coefficient function (d_{33}) in spherical coordinate system.

The piezoelectric constant can be calculated by integrating over the orientation sphere with allowance for the distribution of polar axes and averaging over all the crystallites (domains) [8]. The equation for random ceramic case is given by:

$$\langle d_{33} \rangle_{\text{random}} = \frac{\int_{\theta=0^{\circ}}^{54.7^{\circ}} \int_{\phi=0^{\circ}}^{90^{\circ}} d_{33}(\theta, \phi) \sin\theta d\theta d\phi}{\int_{\theta=0^{\circ}}^{54.7^{\circ}} \int_{\phi=0^{\circ}}^{90^{\circ}} \sin\theta d\theta d\phi} \quad \text{Eqn. 6.16}$$

where $\langle d_{33} \rangle_{\text{random}}$ stands for the average piezoelectric coefficient for a random ceramic. If the calculation is performed using Eqn. 6.16, a $\langle d_{33} \rangle_{\text{random}}$ of 228 pC/N was obtained for random ceramics with 3m symmetry. The calculated value of average piezoelectric constant is 36% of the single crystal piezoelectric coefficient value in the $[001]_{\text{pc}}$.

In order to calculate the average piezoelectric coefficient for a textured ceramic a texture function was incorporated into Eqn. 6.16 as explained in the previous section using the March-Dollase [10] function.

The equation for textured ceramic case is then given by:

$$\langle d_{33} \rangle_{\text{textured}} = \frac{\int_{\theta=0^{\circ}}^{54.7^{\circ}} \int_{\phi=0^{\circ}}^{90^{\circ}} d_{33}(\theta, \phi) F(f, r, \theta) \sin\theta d\theta d\phi}{\int_{\theta=0^{\circ}}^{54.7^{\circ}} \int_{\phi=0^{\circ}}^{90^{\circ}} F(f, r, \theta) \sin\theta d\theta d\phi} \quad \text{Eqn. 6.17}$$

where $\langle d_{33} \rangle_{\text{textured}}$ stands for the average piezoelectric coefficient for the textured ceramic. Again, the values for f and r in the March-Dollase function were assigned to 0.8 (80%) and 0.2 respectively. The calculation performed using Eqn. 6.17 would yield an average piezoelectric coefficient of 475 pC/N for a $[001]_{\text{pc}}$ textured ceramic which is 75% of the single crystal value in the $[001]_{\text{pc}}$.

A comparison of the average calculated piezoelectric coefficient for random and textured ceramics reveal that $[001]_{pc}$ textured PZT (52/48) ceramics have higher piezoelectric constant in the texture direction than a random ceramic but still lower than single crystals piezoelectric constants measured in the same direction. For a rhombohedral crystal, the maximum piezoelectric coefficient is in the $[001]_{pc}$ [3]. A ceramic textured in that direction would display high piezoelectric coefficients. For a random ceramic, the high piezoelectric coefficient in the $[001]_{pc}$ will average out due to the random distribution of that orientation. In Figure 6.9, the averaged piezoelectric coefficient (d_{33}) in a rhombohedral PZT (52/48) as a function of texture fraction in March-Dollase [10] function is plotted, taking the r parameter as constant (0.2).

6.5 CONCLUSIONS

The aim was to calculate the maximum values of polarization, dielectric constant and piezoelectric coefficient allowed by the symmetry of a rhombohedral ceramic for random and textured ceramics. In doing so, there were three major assumptions that were made:

- every grain is in a single domain state,
- the polarization direction is the closest possible direction to the electric field allowed by the symmetry,
- mechanical and electrical coupling between grains was ignored,

therefore, the calculated values are the maximum effective (average) properties that the material is expected to exhibit in the specified direction.

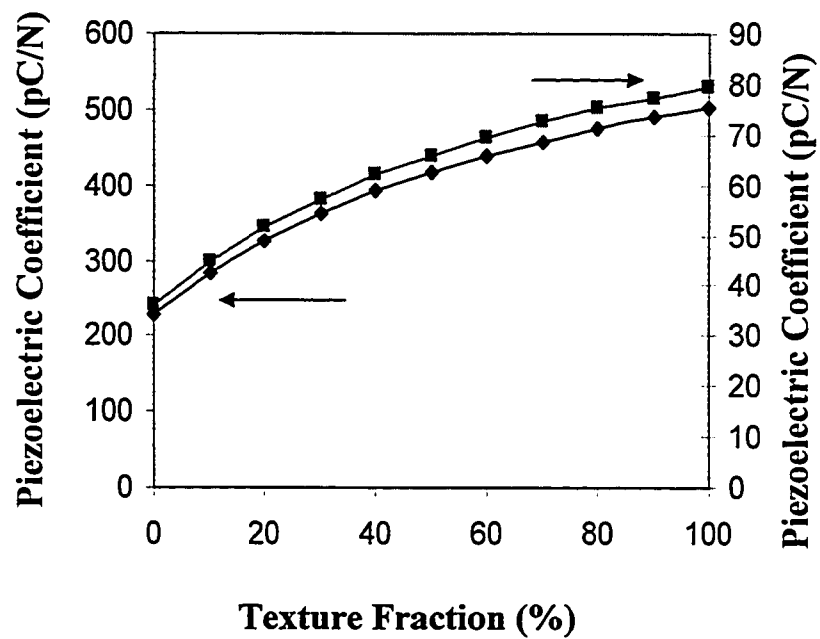


Figure 6.9. Calculated piezoelectric coefficient (d_{33}) (also expressed in %) as a function of texture fraction in rhombohedral PZT (52/48).

Trends in the net polarization, dielectric and piezoelectric coefficients were determined as a function of the degree of texture. Although the domain averaging used in the calculations ignores the grain interactions that lowers the overall macroscopic piezoelectric response, the predictions made are consistent with the experimental results obtained either on PMN-PT [11] or NBT-BT [Chapter 2] ceramics. It is possible to improve the properties of polycrystalline ceramic with crystallographic orientation control.

Comparing the predicted results for poled random ceramic, $[001]_{pc}$ oriented ceramic and $[001]_{pc}$ oriented perovskite single crystal with rhombohedral symmetry reveals that:

- The remanent polarization of a random ceramic is higher than a $[001]_{pc}$ oriented single crystal. The remanent polarization of the $[001]_{pc}$ oriented textured ceramic should be lower than a random ceramic but higher than a $[001]_{pc}$ oriented single crystal.
- The dielectric constant of a random ceramic is lower than that for a $[001]_{pc}$ oriented single crystal. The dielectric constant of the $[001]_{pc}$ oriented ceramic should be higher than a random ceramic but lower than a $[001]_{pc}$ oriented single crystal.
- The piezoelectric coefficient of the random ceramic is lower than a $[001]_{pc}$ oriented single crystal. The piezoelectric coefficient of the textured ceramic should be higher than a random ceramic but lower than a $[001]_{pc}$ oriented single crystal.

6.6 REFERENCES

1. N. A. Pertsev, A. G. Zembilgotov, and R. Waser, "Aggregate Linear Properties of Ferroelectric Ceramics and Polycrystalline Thin Films: Calculation by the Method of Effective Piezoelectric Medium," *J. Appl. Phys.*, **84** (3) pp. 1524-29 (1998).
2. C. W. Nan, D. R. Clarke, "Piezoelectric Moduli of Piezoelectric Ceramics," *J. Am. Ceram. Soc.*, **79** (10) pp. 2563 (1996).
3. S. E. Park, and T. R. Shrout, "Ultrahigh Strain and Piezoelectric Behavior in Relaxor Based Ferroelectric Single Crystals," *J. Appl. Phys.*, **82** (4) 1804-1811 (1997).
4. M. J. Haun, Thermodynamic Theory of the Lead Zirconate Titanate Solid Solution System, Ph.D. Thesis, The Pennsylvania State University, University Park, PA (1988).
5. J. F. Nye, Physical Properties of Crystals, Oxford University Press, London (1972).
6. W. B. Ott, Crystallography. Springer New York (1995).
7. C. Hammond, The Basics of Crystallography and Diffraction. International Union of Crystallography. Oxford Science Publications (1997).
8. M. G. Minchina, and V. P. Dudkevich, "Piezoelectric Properties of Oriented Z' Cuts of PZT-type Ferroelectric Ceramics," *Technical Physics*, **43** (7) pp. 814-17 (1998).
9. J. Erhart, M. Marvan, J. Fousek, "Role of the Soft Dielectric Energy in Poling Ceramics, Glass-like Systems and Domain Average Engineering," *Proceedings of*

the 2000 12th IEEE International Symposium on Applications of Ferroelectrics, 2 pp. 679-682, (2001).

10. W. A. Dollase, "Correction of Intensities for Preferred Orientation in Powder Diffractometry: Application of the March Model," *J. Appl. Crystallogr.*, **19** 267-272 (1986).
11. E. M. Sabolsky, Grain-Oriented $\text{Pb}(\text{Mg}_{1/3}\text{Nb}_{2/3})\text{O}_3$ - PbTiO_3 Ceramics Prepared by Templated Grain Growth, Ph.D. Thesis, The Pennsylvania State University, University Park, PA (2001).

Chapter 7

SUMMARY AND FUTURE WORK

7.1 SUMMARY

$(\text{Na}_{1/2}\text{Bi}_{1/2})_{0.945}\text{Ba}_{0.055}\text{TiO}_3$ ceramics were fiber textured in the $[001]_{\text{pc}}$ direction by using two kinds of template particles, i.e. SrTiO_3 and $\text{Bi}_4\text{Ti}_3\text{O}_{12}$ template particles. Growth of sodium bismuth titanate on the strontium titanate template surfaces was heteroepitaxial. A brick-wall microstructure resulted after sintering at 1200°C , with a SrTiO_3 template located at the core of each grain. 94% textured NBT-BT ceramics, measured by Lotgering factor, were obtained by using 5 vol% SrTiO_3 template particles. The FWHM of the texture distribution was $\sim 8^\circ$, measured by rocking curve and OIM. Reproducible results were easily obtained with SrTiO_3 templates using the TGG approach.

Textured $\text{Na}_{1/2}\text{Bi}_{1/2}\text{TiO}_3\text{-BaTiO}_3$ ceramics were fabricated by reactive templated grain growth using $\text{Bi}_4\text{Ti}_3\text{O}_{12}$ template particles. A texture fraction of 80% was obtained as measured by Lotgering factor. Pre-reaction at 700°C or 800°C before heating the sample to sintering temperature is very critical, because samples directly heated to the sintering temperature did not show any evidence of texturing.

$\langle 001 \rangle_{\text{pc}}$ oriented rhombohedral single crystals show high strain and piezoelectric coefficients [1]. The same concept is also valid for $\langle 001 \rangle_{\text{pc}}$ oriented rhombohedral $\text{Na}_{1/2}\text{Bi}_{1/2}\text{TiO}_3\text{-BaTiO}_3$ ceramics. Piezoelectric coefficients higher than randomly oriented ceramics but close to the single crystal values were obtained. The highest piezoelectric

coefficient of 520 pC/N was measured from the textured sample with 5.5 mol% BaTiO₃ doping, on the rhombohedral side of the MPB. The piezoelectric coefficient from Berlincourt was $d_{33} \sim 200$ pC/N. The properties of textured ceramics can be explained based on a combination of the presence of rhombohedral symmetry and considerable domain wall contributions to the properties in the samples. The d_{33} from Berlincourt measurement of random sample at MPB was 110 pC/N.

At low fields (@ 30 kV/cm) the measured d_{33} from unipolar strain curve was ~ 275 pC/N, however, the Berlincourt number was ~ 200 pC/N. At high fields (@ 70 kV/cm) the measured d_{33} from unipolar strain curve was ~ 520 pC/N. Thus, under unipolar drive, the d_{33} values exceed the low field numbers by $\sim 38\%$ and $\sim 160\%$, respectively. The field dependence of piezoelectric coefficient in unipolar strain curves suggests that there is substantial amount of contribution to d_{33} at high fields. This also draws into question whether the high field numbers reported for flux grown crystals are similarly inflated.

Grain orientation influences the materials properties mainly via crystal anisotropy. There is a very close correlation between texture fraction and electrical and electromechanical properties or any other properties. However, this relation is not linear. In this work, enhancements in the properties were not observed until a high texture fraction ($f > 70\%$), was obtained [2, 3].

The unipolar strain vs. electric field curves of textured Na_{1/2}Bi_{1/2}TiO₃ single crystals is hysteretic. The same behavior (with more hysteresis) is also seen in textured Na_{1/2}Bi_{1/2}TiO₃ ceramics. The reason for the appearance of hysteresis may lie in the phase transition sequence seen in Na_{1/2}Bi_{1/2}TiO₃ ceramics. The transition from cubic phase to

tetragonal phase at 520°C is ferroelastic [4, 5]. The ferroelastic domain state survives and influences the domain state in the succeeding phase transition at 230°C from tetragonal to rhombohedral phase. The electric field does not alter the ferroelastic domains, but a mechanical stress does. Therefore, it is highly probable that the poling of the ceramic in the rhombohedral phase only temporarily moves some of the ferroelectric domain boundary. If the field is removed ($E=0$ kV/cm), some of the initial domain structure may reappear again. So, every time a unipolar strain measurement is done, domain boundary movement leads to hysteresis in the curve. If this is the case, unless a mechanical stress is applied while cooling through the two transition temperatures to control the domain state it is hard to get an engineered domain state at room temperature. The source of hysteresis might be also the point defects, and/or field forced transition to tetragonal phase.

Using linear averaging methods, the macroscopic properties of randomly oriented and $[001]_{pc}$ textured perovskite ceramics were estimated from single crystal data. Since, the complete polarization, dielectric, and piezoelectric tensors are not available for the $Na_{1/2}Bi_{1/2}TiO_3$ - $BaTiO_3$ system, the properties of lead based rhombohedral ferroelectric single crystal-single domain PZT (52/48) (whose properties were computed using Landau-Ginsburg-Devonshire phenomenological theory,) were used in the calculations [6].

The variation in polarization, dielectric constant, and piezoelectric coefficient of $[001]_{pc}$ textured $Na_{1/2}Bi_{1/2}TiO_3$ - $BaTiO_3$ ceramics were consistent with the calculations based on the rhombohedral symmetry present in the crystallites (domains). Since $[001]_{pc}$ is not the polar direction in a rhombohedral crystal, a $[001]_{pc}$ textured ceramic should possess lower remanent polarization than a randomly oriented sample, but larger than a

[001]_{pc} cut single crystal. The room temperature dielectric constant increases with increasing texture fraction from 500 for randomly oriented ceramic to 650 for f=94% textured ceramics.

<001>_{pc} oriented rhombohedral single crystals show high strain and piezoelectric coefficients. The same concept is also valid for <001>_{pc} oriented rhombohedral Na_{1/2}Bi_{1/2}TiO₃-BaTiO₃ ceramics. A piezoelectric coefficients higher than randomly oriented ceramics but close to the single crystal values were obtained. The high value of d₃₃ is at least partly because textured samples were more hysteretic than single crystals as a result of the unstable domain state.

7.2 FUTURE WORK

The electromechanical properties of Na_{1/2}Bi_{1/2}TiO₃-BaTiO₃ ceramics were calculated from the slope of unipolar strain measurements. These measurements are high field measurements. The electromechanical properties need to be measured using resonance methods. This method utilizes low electric fields.

Texture in the ceramic can be well characterized using EBSD. Orientation Distribution Function (ODF) can be then calculated from EBSD data and can be used to correlate texture and properties [7]. Local arrangements of the grains can be better incorporated into the averaging equation, leading to better approximations of the macroscopic property.

In many textured ceramics, template particles are a different phase, but have similar crystal structure and lattice parameter of the matrix phase. Sometimes, template particles (seeds) do not react with the matrix material and maintain their single

crystallinity and phase, like $\text{Na}_{1/2}\text{Bi}_{1/2}\text{TiO}_3$ textured with SrTiO_3 templates. The properties of bulk materials are modified by the presence of template particles due to clamping, dilution and electric field in-homogeneity. The seed at the center of the templated grain do not show the same response to the electric field as the matrix material, usually hinders the strain in the matrix material leading to clamping effect. Furthermore, the dielectric constant of the seed and the matrix materials are different from each other. The electric field (E) across the sample will not be homogeneous across the sample. Further study needs to be done in this area. The system described above resembles a 0-3 composite. Such a system can be modeled using as 0-3 composite model where the template particles can be regarded as the discontinuous phase. The dielectric properties of the textured ceramics can be modeled using logarithmic mixing law.

Linear averaging of the single crystal properties to estimate the macroscopic physical properties of randomly oriented and textured ceramics results in overestimation [2]. Effective medium theory that has been adapted to piezoelectric ceramics to estimate the dielectric and piezoelectric properties gives more realistic numbers. However, effective medium theory has not been adapted to estimate the piezoelectric properties of textured ceramics with rhombohedral symmetry (3m) crystallites. In EMT, the response of a piezoelectric grain is modeled in a piezoelectric matrix. Since the piezoelectric response of the grain and the matrix is different, the assumed model represents the real situation more realistically.

It is clear from the review of the literature that the largest piezoelectric coefficients observed to date in $\text{Na}_{1/2}\text{Bi}_{1/2}\text{TiO}_3$ -based single crystals is coupled with substantial hysteresis. One possible cause for high hysteresis in the unipolar strain curve

is related to the high temperature ferroelastic phase transition. A compositional modification of the $\text{Na}_{1/2}\text{Bi}_{1/2}\text{TiO}_3$ ceramics might be required so that the high temperature ferroelastic phase transition might be avoided. Then, it might be possible to further decrease the hysteresis in $\text{Na}_{1/2}\text{Bi}_{1/2}\text{TiO}_3$ based ferroelectric ceramics.

The crystal structure refinement by Jones and Thomas [8] is still controversial. To correctly assign the crystal symmetry, a high quality $\text{Na}_{1/2}\text{Bi}_{1/2}\text{TiO}_3$ single crystal is required. The single crystals of $\text{Na}_{1/2}\text{Bi}_{1/2}\text{TiO}_3$ are usually grown by flux method in which it is difficult to control compositional inhomogeneity (variation). Because $\text{Na}_{1/2}\text{Bi}_{1/2}\text{TiO}_3$ melts incongruently at 1290°C [9]. However, it might be possible to grow single crystals of $\text{Na}_{1/2}\text{Bi}_{1/2}\text{TiO}_3$ by surface templated grain growth process which might allow better control over stoichiometry. In surface templated grain growth, the growth of single crystal is at relatively lower temperatures compared to flux methods, so the volatilization of the species, Na and Bi in this case, can be better controlled.

7.3 REFERENCES

1. S. E. Park, and T. R. Shrout, "Ultrahigh Strain and Piezoelectric Behavior in Relaxor Based Ferroelectric Single Crystals," *J. Appl. Phys.*, **82** (4) 1804-1811 (1997).
2. N. A. Pertzev, A. G. Zembilgotov, and R. Waser, "Aggregate Linear Properties of Ferroelectric Ceramics and Polycrystalline Thin Films: Calculation by the Method of Effective Piezoelectric Medium," *J. Appl. Phys.*, **84** [3] pp. 1524-29 (1998).
3. C. Duran, *Fabrication and Electrical Properties of Textured $Sr_{0.53}Ba_{0.47}Nb_2O_6$ Ceramics Prepared by Templated Grain Growth*. Ph.D. Thesis, Penn State University (2001).
4. K. Sakata, and Y. Masuda, "Ferroelectric and Antiferroelectric Properties of $(Na_{0.5}Bi_{0.5})TiO_3$ - $SrTiO_3$ Solid Solution Ceramics," *Ferroelectrics*, **7** pp. 347-51 (1974).
5. S. B. Vakhrushev, B. G. Ivanitskii, B. E. Kvyatkovskii, and A. N. Maistrenko, "Neutron Scattering Studies of the Structure of Sodium Bismuth Titanate", *Sov. Phys. Solid State*, **25** [9] p 1504-6 (1983).
6. M. J. Haun, *Thermodynamic Theory of the Lead Zirconate Titanate Solid Solution System*, Ph.D. Thesis, The Pennsylvania State University, University Park, PA (1988).
7. H. J. Bunge, "Grain Orientation and Texture"; Ch. 41 in Industrial Applications of X-Ray Diffraction. Edited by F. H. Chung, and D. K. Smith. Marcel Decker Inc, New York, 2000.

8. G. O. Jones and P. A. Thomas, "Investigation of the Structure and Phase Transitions in the Novel A-site Substituted Distorted Perovskite Compound $\text{Na}_{1/2}\text{Bi}_{1/2}\text{TiO}_3$," *Acta Crystallographica*, **B58** [2] pp. 168-178 (2002).
9. S. E. Park, S. J. Chung, I. T. Kim, and K. S. Hong, "Nonstoichiometry and Long-Range Cation Ordering in Crystals of $(\text{Na}_{1/2}\text{Bi}_{1/2})\text{TiO}_3$," *J. Am. Ceram. Soc.*, **77** [10] pp. 2641-47 (1994).

VITA

Huseyin YILMAZ

Huseyin Yilmaz was born January 07, 1970 in Kirsehir, Turkey. He obtained his B.Sc. in Metallurgical Engineering at the Middle East Technical University in 1994. After graduation, he joined the graduate program in Materials Science and Metallurgical Engineering at the Middle East Technical University in 1994, and obtained his M.Sc. in February 1997. Mr. Yilmaz received a Higher Educational Council Scholarship from Ministry of Education, and began his attendance in Materials Science and Engineering at the Pennsylvania State University in June 1997. He has since been working towards his Ph.D. He will be employed as an assistant professor at the Gebze Institute of Technology in Turkey.